FINITE ELEMENT METHOD BASED SIMULATIONS OF LOW FREQUENCY MAGNETIC FIELD IN SEAWATER

A THESIS
SUBMITTED TO THE DEPARTMENT OF ELECTRICAL AND
ELECTRONICS ENGINEERING
AND THE GRADUATE SCHOOL OF ENGINEERING AND SCIENCE
OF BILKENT UNIVERSITY
IN PARTIAL FULFILLMENT OF THE REQUIREMENTS
FOR THE DEGREE OF
MASTER OF SCIENCE

By
Fatih Emre Şimşek
August, 2013

I certify that I have read this thesis and that in my opinion it is fully adequate, in scope and in quality, as a thesis for the degree of Master of Science.

Prof. Dr. Yusuf Ziya İder (Advisor)

I certify that I have read this thesis and that in my opinion it is fully adequate, in scope and in quality, as a thesis for the degree of Master of Science.

Prof. Dr. Hayrettin Köymen

I certify that I have read this thesis and that in my opinion it is fully adequate, in scope and in quality, as a thesis for the degree of Master of Science.

Assist. Prof. Dr. Satılmış Topçu

Approved for the Graduate School of Engineering and Science:

Prof. Dr. Levent Onural
Director of the Graduate School

ABSTRACT

FINITE ELEMENT METHOD BASED SIMULATIONS OF LOW FREQUENCY MAGNETIC FIELD IN SEAWATER

Fatih Emre Şimşek
M.S in Electrical and Electronics Engineering
Supervisor: Prof. Dr. Yusuf Ziya İder
August, 2013

Propagation properties of the electromagnetic waves in seawater are different than in air (vacuum) due to electrical conductivity (σ) and high relative permittivity (ε_r) of the seawater. Numerically it is hard to solve the electromagnetic waves in seawater for the complex geometries. With the help of the advances in the Finite Element Method (FEM) tools as well as the personal computers, we have chance to analyze magnetic field of the complicated and complex geometries of physical systems in seawater. In this thesis; an air-cored multilayer transmitting coil is designed. Then the low frequency magnetic flux density of this coil in different studies in seawater in COMSOL Multiphysics is solved. In the first study; the magnetic flux density of the coil in air and in seawater for different frequencies on different observation points is solved. In the second study; the shielding effect of the material of the case of the coil as well as the thickness of the case is analyzed. Specific materials as well as thickness for the case are proposed. In the third study; the perturbation of the magnetic flux density of the coil due to a metal plate is analyzed. The material of the metal plate is taken iron and copper. Iron has high relative permeability (μ_r) and high electrical conductivity (σ). Copper has unity permeability (μ_0) and high electrical conductivity (σ). Effect of the high electrical conductivity on the perturbation of the magnetic flux density on the observation point is analyzed.

Effect of high relative permeability on the phase shift of the field on the observation point is observed. A detection region for the plate and coil geometries according to the attenuation of the secondary fields caused by the eddy currents on the metal plate is proposed. In the last study; perturbation of ambient Earth magnetic field due to a submarine is solved and how this perturbation can be imitated by an underwater system, which tows a DC current carrying wire is analyzed. These underwater systems are used to test detection performance of magnetic anomaly detector (MAD) equipped aircrafts.

Keywords: Finite Element Method, COMSOL Multiphysics, Air-cored multilayer coil, Metal detection in seawater, Magnetic anomaly detection.

ÖZET

DÜŞÜK FREKANSTA MANYETİK ALANIN DENİZ SUYUNDA SONLU ELEMANLAR YÖNTEMİNE DAYALI BENZETİMLERİ

Fatih Emre Şimşek
Elektrik ve Elektronik Mühendisliği, Yüksek Lisans
Tez Yöneticisi: Prof. Dr. Yusuf Ziya İder
Ağustos, 2013

Elektromanyetik dalgaların su içindeki yayılma özellikleri havadakinden (vakum) suyun elektrik iletkenliği (σ) ve yüksek bağıl yalıtkanlık sabiti (ε_r) yüzünden farklıdır. Karmaşık geometriler için elektromanyetik dalgaları deniz suyu içinde nümerik olarak çözmek zordur. Sonlu Elemanlar Yöntemi (SEY) araçlarındaki ve kişisel bilgiayarlardaki gelişmeler sayesinde deniz suyu içinde karmaşık fiziksel sistemleri analiz etme şansımız vardır. Tezde; hava çekirdekli çok katmanlı bir göndermeç sarımı tasarlanmıştır. Daha sonra bu sarımın manyetik akı yoğunluğu deniz suyunda farklı durumlarda COMSOL Çoklufizik'de incelenmiştir. İlk çalışmada; sarımın manyetik akı yoğunluğu havada ve suda farklı frekanslarda ve farklı gözlem noktalarında çözülmüştür. İkinci çalışmada; bobinin içinde bulunduğu gövdenin malzemesinin ve gövde kalınlığının ekranlama analizi yapılmıştır. Gövde için belirli malzeme ve kalınlık önerisinde bulunulmuştur. Üçüncü çalışmada; sarımın manyetik akı yoğunluğunun metal bir plaka yüzünden bozulmasının analizi yapılmıştır. Metal plakanın malzemesi demir ve bakır alınmıştır. Demir yüksek bir bağıl manyetik geçirgenlik (μ_r) ve elektriksel iletkenliğe (σ) sahip olup; bakır ise birim manyetik geçirgenlik (μ_0) ve yüksek elektriksel iletkenliğe (σ) sahiptir. Yüksek elektriksel iletkenliğin gözlem noktasındaki manyetik akı yoğunlunda yaptığı etki analiz edilmiştir. Yüksek bağıl manyetik geçirgenliğin gözlem noktasındaki manyetik alanın fazındaki kaymaya etkisi analiz edilmiştir. Plaka ve sarım geometleri için metal plaka üzerinde oluşan eddy akımlar tarafından yaratılmış ikincil alanların sönümlenmesine göre bir saptama bölgesi önerilmiştir. Son çalışmada ise; dünyanın manyetik alanının bir deniz altı tarafından bozulması çözülmüş ve bu bozulma nasıl DC akım taşıyan bir teli çeken sualtı sistemi tarafından taklit edilebilir analiz edilmiştir. Bu sualtı sistemleri manyetik anomali detektörü (MAD) ile donatılmış hava taşıtlarının saptama performanslarını test etmek için kullanılır.

Anahtar sözcükler: Sonlu Elemanlar Yöntemi, COMSOL Çoklufizik, Hava çekirdekli çok katmanlı bobin, suda metal saptaması, Manyetik anomali saptaması.

To My Family

Acknowledgements

I would like to express my gratitude to my supervisor Prof. Dr. Yusuf Ziya İder for his instructive comments, invaluable guidance and continuing support in the supervision of the thesis.

I would like to express my special thanks and gratitude to Prof. Dr. Hayrettin Köymen and Dr. Satılmış Topçu for showing keen interest to the subject matter and accepting to read and review the thesis.

My parents Cihan and Birgül Şimşek, and my brother Oğuz Şimşek deserve special mention for their support and encouragement. I also would like to thank my friends Taha Ufuk Taşcı, Ali Alp Akyol, Güneş Bayır, Durmuş Ali Taşdemir, Fatih Süleyman Hafalır, Necip Gürler and especially Merve Nur Çenesiz for their support and friendship.

Contents

List of Figures

List of Tables

Chapter 1

INTRODUCTION

Due to the recent developments in electronics as well as increase of the human activity on the sea, underwater systems have become popular. With the ease of new technological developments, many new applications have been designed; old fashioned methods have been re-evaluated. Underwater telemetry and control systems have been used for different applications. These applications are related to communication, monitoring of wildlife, sensing, navigation, control and monitoring of Autonomous Underwater Vehicles (AUV).

There are three different techniques that have been used in underwater environment. These techniques are based upon acoustic [1,2,3,4,5], optic [6,7,8,9] and electromagnetic [10,11,12] principles. As listed in [1], these techniques have advantages and disadvantages compared to each other. Acoustic based technology has these advantages; long range up to 20km, energy efficient, precision navigation, low size and cost; in the meantime acoustic based technology has these disadvantages; unable to transit water air boundary, poor in shallow water, adversely affected by water aeration, ambient noise and unpredictable propagation, latency, limited bandwidth detectable and impact on marine life [1,2,3,4,5]. Optical based technology has advantages which are ultra-high bandwidth and low cost; but also has disadvantages as well. These are susceptible to turbidity and particles, marine fouling on lens faces, needs tight alignment, very short range and difficult to cross water/air boundary [6,7,8,9]. Lastly; electromagnetic based technology has both advantages and disadvantages; signal passes through ice, water/air and water/seabed boundary, unaffected by water depth, unaffected by turbidity and bubbles, good non-line-of-sight performance, immune to acoustic noise, immune to marine fouling, up to 100 Mbps data rates, frequency agile capability, unaffected by multi-path, no known effects on marine animals are the advantages, being sensitive to electromagnetic interferences and limited range through water are the disadvantages [10,11,12].

Electromagnetic based technology has many applications that exploit the advantages of electromagnetic waves in seawater. The followings are some applications of the electromagnetic based technology: real-time control of Unmanned Underwater Vehicles (UUV) from shore, submarines and surface vessels, wireless through-hull transfer of power and data, high-speed transfer of data between UUVs and surface vessels, real-time transfer of sensor data from UUVs when submerged, communications between UUVs and subsea sensors, UUV distributed navigation systems for shallow harbors and ports, UUV docking systems, subsea navigation beacons; asset location, asset protection, subsea networks, data transmission from underwater sensors to surface or shore without surface repeaters, harvest data from submerged sensors via Unmanned Airborne Vehicles, communications; UUV to UUV, submarine to UUV, UUV to Unmanned Surface Vehicle, UUV to Unmanned Airborne Vehicles, diver communications (speech and texting), underwater navigation, underwater sensing [13].

1.1 Metal Detectors

One of the most popular applications of electromagnetic based technology is metal detectors in seawater [14,15,16,17,18]. One of the motivations of metal detectors is to search treasures located deep below the oceans. Ships have been transporting the riches of the world from port to port in their travels around the world. Some ships ran into dangerous situations and sink with valuable items under seawater during their journey. Trying to detect the location of such shipwrecks is interest of some adventurers. They try to find caches of gold, silver or anything else rumored to have been hidden somewhere in the shipwreck [15]. When searching such shipwrecks, boat towed metal detectors or magnetometers are used [16]. Metal detectors can be used to detect all types of metals for reasonable depth [17]. Magnetometers can be used to locate iron and steel at greater depth. If the adventurer can narrow the searching zone, a hand held metal detector can be used. Hand held metal detectors feature either Pulse or Broad Band Spectrum circuit to eliminate the effect of the minerals in the seawater [18]. One another motivation of the metal detectors is to detect underwater cables. Such cables are power and communication cables of submarines. These cables which are installed in shallow waters have been buried under the seabed. If these cables need to be repaired or relocated, they need to be detected and tracked via metal detectors [19].

Magnetic field strength is measured via various different technologies. Each technique has its own unique properties that make it more suitable for particular applications. Devices which measure low fields (< 1 mT) are called magnetometers and high fields (> 1 mT) are called gaussmeters [20]. Magnetometers are separated into vector component and scalar magnitude types. Vector component type magnetometers are search coil, fluxgate, SQUID (superconducting quantum interference device), magnetoresistive and fiber-optic. Scalar type magnetometers are proton precession and optically pumped. Sorts of gaussmeters are Hall Effect, magnetoresistive, magnetodiode and magnetotransistor [21].

Metal detectors can be sorted according to the technology they use or according to transmitting and receiving coil orientations. Each technology can have its transmitting and receiving coil orientations and each orientation can have its own technology [22,23]. Metal detectors use one of three technologies: very low frequency (VLF), pulse induction (PI) and beat-frequency oscillation (BFO).

1.1.1 Metal Detector Technologies

In very low frequency (VLF) technology there are two distinct coils. The outer coil loop is the transmitter coil. It is a coil of wire. Electricity is sent along this wire. The current moving through the transmitter coil creates an electromagnetic field. The polarity of the magnetic field is perpendicular to the coil of wire. As the current changes direction, the polarity of the magnetic field changes. If the coil of wire is parallel to the ground, the magnetic field is constantly pushing down into the ground and then pulling back out of it. As the magnetic field goes back and forth into the ground, it interacts with any conductive objects it encounters, causing them to generate weak magnetic fields of their own. The polarity of the object’s magnetic field is directly opposite the transmitter coil’s magnetic field. If the transmitter coil’s field is pulsing downward, the object’s field is pulsing upward. The inner coil loop is the receiver coil which is another coil of wire. It acts as an antenna to collect and amplify frequencies coming from the target objects in the ground. When the receiver coil passes over an object giving off a magnetic field, a small electric current goes through the coil. This current oscillates at the same frequency as the object’s magnetic field. The coil amplifies the signal and sends it to the control box of the metal detector [24,25].

PI systems may use a single coil. This coil can be both transmitter and receiver. The system also may have two or even three coils working together. This technology sends powerful, short bursts (pulses) of current through a coil of wire. Each pulse generates a brief magnetic field. When the pulse ends, the magnetic field reverses polarity and collapses very suddenly, causing a very sharp electrical spike. This spike lasts a few microseconds and results in another current to run through the coil. This current is named the reflected pulse and is extremely short, lasting only about 30 microseconds. Another pulse is then sent and the process repeats. In a PI metal detector, the magnetic fields from target objects add their “echo” to the reflected pulse, making it last a fraction longer than it would without them. A sampling circuit in the metal detector is set to monitor the length of the reflected pulse. By comparing it to the expected length, the circuit can determine if another magnetic field has caused the reflected pulse to take longer to decay. If the decay of the reflected pulse takes more than a few microseconds longer than normal, there is probably a metal object interfering with it [26,27].

In a beat-frequency oscillator (BFO) system there are two coils of wire. One large coil is in the search head and a small coil is located inside the control box. Each coil is connected to an oscillator that generates thousands of pulses of current per second. The frequency of these pulses is slightly offset between the two coils. When the pulses travel through each coil, the coil generates radio waves. A small receiver within the control box collects the radio waves and creates an audible series of tones (beats) based on the difference between the frequencies. If the coil in the search head passes over a metal object, the magnetic field caused by the current flowing through the coil creates a magnetic field around an object. The object’s magnetic field interferes with the frequency of the radio waves generated by the search-head coil. As the frequency deviates from the frequency of the coil in the control box, the audible beats change in duration and tone [22,28].

1.1.2 Coil Orientations of Metal Detectors

In the view of the orientation of the transmitting and receiving coil there are different types of coil configurations in the metal detectors. Each of them has its own advantages with respect to the techniques they are driven. The followings are some common configurations of the transmitting and receiving coils.

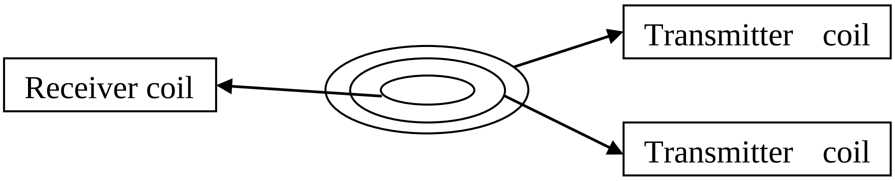

Figure 1.1: Coil configuration no. 1.

Coil configuration no. 1 is called the GEM-3 configuration. There are three concentric coils; two are transmitting and one is receiving (US Patent No. 5,557,206) in this configuration. Transmitter coil 1 is connected in an opposite polarity to a small inner transmitter coil which creates a magnetic cavity at the center where the receiver coil is placed. The two transmitting coils work together to cancel (or buck) the source field at the receiver coil. This source cancellation (or bucking) method provides a great increase in sensor dynamic range and gives a resolution of parts-per-million level [29].

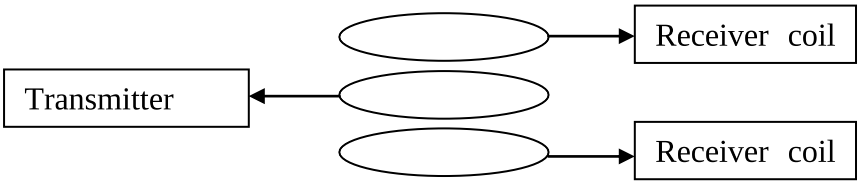

Figure 1.2: Coil configuration no. 2.

Coil configuration no. 2 is called GEM-5 configuration (US Patent No. 6,204,667). There are three concentric coils; one is transmitter at the center and two are receiver on either side of and at equal distance from the transmitter. The outputs from the two receiver coils are subtracted to cancel the primary signal from the transmitter, providing a dynamic range and resolution similar to the GEM-3 configuration [30].

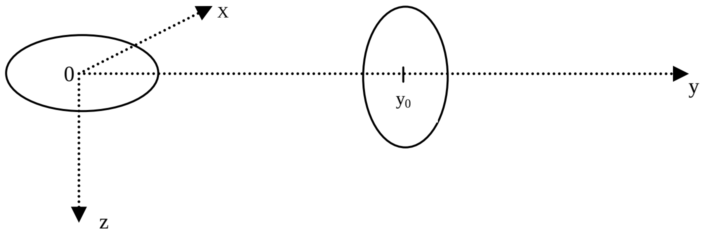

Figure 1.3: Coil configuration no. 3.

There are two coils in the coil configuration no 3. One is the transmitter coil at the origin (0, 0, 0). The other is the receiver coil perpendicular to the plane of the transmitter coil. The receiver coil is at the point (0, y_0, 0). Due to the reciprocity, transmitter and receiver coils can be interchangeable, that is transmitter coil can be receiver coil and receiver coil can be transmitter coil [19].

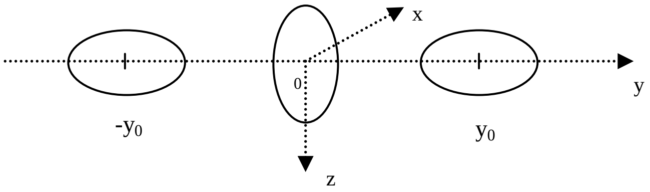

Figure 1.4: Coil configuration no. 4.

There are three coils in the configuration no. 4. One is the transmitter coil at the origin and other two receiver coils are symmetrically away from the transmitter coil. The plane of the transmitter coil is perpendicular to the receiving coils'. The advantage of this configuration compared to the configuration 3 is that the position of the detected material can be discriminated according to the detector carrying device [31].

1.2 Fluxgate Magnetometer

The fluxgate magnetometer is a magnetic field sensor for vector magnetic field. It can measure earth's field and resolve below one 10,000th of that. It has been used for navigation, compass work, metal detection and prospecting. It is easy to construct. There are two style of design of it: designed with rod cores and designed with ring cores. These cores are highly permeable cores which serve to concentrate the magnetic field to be measured. The core is magnetically saturated alternatively in opposing directions along any suitable axis, normally by means of an excitation coil driven by a sine or cosine signal. Prior to saturation the ambient field is guided through the core producing a high flux due to its high permeability. When the core saturates, the core permeability falls away to that of vacuum causing the flux to collapse. In the next half cycle of the excitation waveform the core recovers from saturation and the flux because of the ambient field is once again at a high level until the core saturates in the reverse direction; the cycle then repeats. Although the magnetisation reversals due to excitation, the flux from the ambient field operates in the same direction throughout. A sense coil placed around the core will collect these flux changes, the sign of the induced voltage indicating flux collapse or recovery [32].

1.3 DC Magnetic Anomaly Detector

Conventional detection of submarines has involved both acoustic and non-acoustic techniques. Acoustic technique is the utilization of active and passive hydrophones. These sound methods promise great range in the detection of the submarines, [33]. Alternative techniques to detect submarines by hydrophones were being studied in years 1917. One alternative was the use of magnetism. Magnetic anomaly detection (MAD) is a passive method used to detect visually obscured ferromagnetic objects by revealing the anomalies in the ambient Earth magnetic field, [34]. The U.S experimentally tried a ship towed magnetic detection device in 1918. This device had too limited a detection range and also suffered from the presence of the magnetic signature of the towing ship. With the outbreak of WW II, renewed interest occured in alternative detection systems for anti-submarine warfare. There was a pressing need to devise a means for them to be able to detect a submerged submarine for aircraft. One of the devices that received renewed attention was the use of magnetic anomaly detection. As early as 1941 magnetic detection devices (which measure changes in the Earth's magnetic field) were developed in both Britain and the U.S. The first use of these devices was in U.S K type blimps. This was followed by much wider installation of MAD devices in ASW patrol aircraft. Most ASW aircraft were equipped with MAD by 1943. Initially, the U.S. thought that MAD would be a primary means of detecting submerged submarines. In use MAD was found to be a system of limited usefulness. This was due to its very limited range and, its inability to distinguish between sources of magnetic variance. Frequently, wrecks or local magnetic disturbances were classified as submarines. This was particulary true earlier in the war before experience with the system had discovered its limitations. MAD in combination with sonobuoys proved more useful by late war. In combination, MAD let an aircraft to localize a contact made with sonobuoys and, the sonobuoys provided confirmation that the contact was, indeed, a submarine. In this combination MAD became the secondary system to the sonobuoy, the reverse of what was originally expected [35].

In order to test the detection performance of a magnetic anomaly detector equipped aircraft, a submerged submarine is needed and practicaly it is hard to have a submerged submarine any time it is necessary. Instead of having a submerged submarine, a submerged system can be used to test the detection of a magnetic anomaly detector equipped aircraft. In order to imitate the anomalies on the ambient Earth magnetic field caused by the submarine, the submersed system which tows DC current carrying wire can be utilized. Anomaly created by this system can be tried to be detected by MAD equipped aircrafts. Utilization of such systems cost less money and time than floating a submarine.

1.4 Scope of the Thesis

The Finite Element Method (FEM) has been developed and many commercial FEM tools has been started to be utilized. One of the FEM tools is COMSOL

Multiphysics software. This is a general purpose-software platform, based on advanced numerical methods, for modeling and simulating physics-based problems [36]. In the thesis, we make use of this software. Not only FEM tools have been developed but also physical memory and computation power of the personal computers have been increased. With the help of the advances in the FEM tools as well as the personal computers, we can analyze the complicated and complex geometries of physical systems. In the thesis; we solve the low frequency magnetic flux density of an air-cored multilayer coil in different cases in seawater. In the first study the magnetic flux density of the coil in air and in seawater for different frequencies on different observation points is solved. In the second study; the shielding effect of the material of the case of the coil as well as the thickness of the case is analyzed. Specific materials for the case as well as thickness for the case are proposed. In the third study; the perturbation of the magnetic flux density of the coil due to a metal plate which is firstly iron then copper are analyzed. Iron has high relative permeability (μ_r) and high electrical conductivity (σ). Copper has unity permeability (μ_0) and high electrical conductivity (σ). Effect of the high relative permeability and electrical conductivity on the perturbation of the magnetic flux density of the coil is observed. A detection region for the plate and coil geometries according to the strength of the perturbation of the magnetic field is proposed. In the last study; perturbation of ambient Earth magnetic field due to a submarine is solved and how this perturbation can be imitated by a current carrying wire system so as to test magnetic anomaly detector (MAD) equipped aircrafts is analyzed.

1.5 Outline of the Thesis

The outline of the thesis as follows. The second chapter discusses the theory and numerical methods for low frequency magnetic field in seawater. In the third chapter design of an air-cored multilayer coil is presented. Case studies of low frequency magnetic field of the air-cored multilayer coil in seawater are illustrated in the forth chapter. In addition, the perturbation of ambient Earth magnetic field due to a submarine and how this perturbation can be imitated by current carrying wire system is studied in the forth chapter. Finally, discussions and conclusions are in the fifth chapter.

Chapter 2

Theory and Numerical Methods for Low Frequency Magnetic Field in Seawater

2.1 Introduction

Electromagnetic properties of seawater and air as well as governing equations of propagation of electromagnetic waves in seawater are presented in this chapter. Propagation properties of the electromagnetic waves in seawater are different than in air (vacuum). The reason of this difference is that seawater has electrical conductivity (σ) and high relative permittivity (ε_r). Electrical conductivity of seawater varies from 1 to 8 (S/m). If the salinity of the sea is low the conductivity is close to 1and if it is high, the conductivity is close to 8.

2.1 Formulation

In order to understand the behavior of the electromagnetic waves in seawater, the governing equations must be known. Maxwell's equations predict the propagation of electromagnetic (EM) waves travelling in seawater. To derive the partial differential equation (PDE) system to be solved in the *Magnetic Fields* interface under the branch of *AC/DC* for the physics section of the model in the COMSOL Multiphysics, we start with Ampere's law:

$$\nabla \times H = J + \frac{\partial D}{\partial t} = \sigma E + \sigma v \times B + J_e + \frac{\partial D}{\partial t}. \tag{2.1}$$

Now assume time-harmonic fields and use the definitions of the potentials:

$$B = \nabla \times A, \tag{2.2}$$

$$E = -\nabla V - \frac{\partial A}{\partial t}, \tag{2.3}$$

Constitutive relationships between electrical and magnetic fields are the followings:

$$B = \mu_r \mu_0 H, \tag{2.4}$$

$$D = \varepsilon_r \varepsilon_0 E, \tag{2.5}$$

where μ_0, ε_0 are the permittivity and permeability of vacuum, with numerical values:

$$\mu_0 = 4\pi \times 10^{-7} \text{ (henry/m)}, \tag{2.6}$$

$$\varepsilon_0 = 8.854 \times 10^{-12} \text{ (farad/m)}. \tag{2.7}$$

In frequency domain, Ampere's law and electrical field are the followings:

$$\nabla \times H = \sigma E + J_e + j\omega D, \tag{2.8}$$

$$E = -j\omega A. \tag{2.9}$$

Electric displacement field (D) can be re-written according to the equations (2.5) and (2.9) as following:

$$D = -j\omega \varepsilon_r \varepsilon_0 A. \tag{2.10}$$

Magnetic field strength (H) can be re-written according to the equation (2.4) as the following:

$$H = \mu_r^{-1} \mu_0^{-1} B. \tag{2.11}$$

Finally, when we put the equations (2.10) and (2.11) into the equation (2.8) and re-arrange it, we find the PDA solved in COMSOL Multiphysics:

$$\left(\mathrm{j}\omega\sigma-\omega^{2}\varepsilon_{\mathrm{o}}\varepsilon_{\mathrm{r}}\right)\mathrm{A}+\nabla\times\left(\mu_{\mathrm{o}}{}^{-1}\mu_{\mathrm{r}}{}^{-1}B\right)=\mathrm{J}_{e}. \tag{2.12}$$

A linearly polarized plane EM wave propagating in the z direction can be described in terms of the electric field strength E_x and magnetic field strength H_y with [37],

$$E_{X}=E_{0}\exp(j\omega t-\gamma z), \tag{2.13}$$

$$\mathrm{H}_{y}=\mathrm{H}_{0}\exp(j\omega t-\gamma z). \tag{2.14}$$

The propagation constant (γ) can be written in terms of permittivity (ε), permeability (μ), and electrical conductivity (σ) by

$$\gamma=\mathrm{j}\omega\sqrt{\varepsilon\mu-j\frac{\sigma\mu}{\omega}}=\alpha+j\beta, \tag{2.15}$$

where α is the attenuation factor, β is the phase factor, and $\omega=2\pi f$ is the angular frequency. For a fixed frequency and conductivity, absorption coefficient and wavelength in seawater can be written as the followings:

$$\alpha=17.3\times10^{-3}(\sigma\mathrm{f})^{1/2}\ (\mathrm{dB/m}), \tag{2.16}$$

$$\lambda=3.16\times10^{3}/\ (\sigma\mathrm{f})^{1/2}\ (\mathrm{m}). \tag{2.17}$$

When α and λ are multiplied, how much electromagnetic energy in one wavelength to be absorbed is found:

$$\alpha \, \lambda \; = \; 54.6 (\mathrm{dB}) \tag{2.18}$$

The attenuation of 54.6 dB in one wavelength is a high value. This absorption prevents the magnetic waves to penetrate long distances in seawater.

The speed of the electromagnetic wave in seawater is dependent upon the frequency and electrical conductivity:

$$\mathrm{c} \; = \; 3.12 \text{ x } 10^{3} \left(\mathrm{f} \, / \, \sigma \right)^{1/2} (\mathrm{m/s}). \tag{2.19}$$

For example, the speed of the electromagnetic wave is $50 \mathrm{x} 10^{3}$ m/s and the wavelength is 50m if the frequency is 1 kHz and the conductance of the seawater is 4 (S/m). The speed of the electromagnetic wave in air is $3 \mathrm{x} 10^{8}$ m/s and the wavelength is $300 \mathrm{x} 10^{3}$ m if the frequency is 1 kHz. The following table summarizes this example.

Medium	**Air (vacuum)**	**Seawater**
Speed of electromagnetic wave (c) (m/s)	$3 \mathrm{x} 10^{8}$	$50 \mathrm{x} 10^{3}$
Wavelength (λ) (m)	$300 \mathrm{x} 10^{3}$	50
Conductivity (σ) (S/m)	0	4
Permeability (μ) ($\mathrm{H.m}^{-1}$)	1	1
Permittivity (ε_{r}) (F/m)	1	80

Table 2.1: Electromagnetic properties of air and seawater for the frequency 1 kHz.

Chapter 3

DESIGN OF AN AIR-CORED MULTILAYER COIL

In this chapter; we design an air-cored multilayer coil in order to solve the magnetic field of it in different case studies in seawater. We need the an air-cored solenoid coil which is able to be steered with plausible current and power. Since power consumption is an important criterion for an underwater system. We steer the coil with 1 Ampere current through the studies. In order to be able to steer the coil with 1 Ampere current, the coil has to have plausible impedance value at low frequencies. We need to calculate the inductance of the coil so as to calculate the impedance of it. The geometry and dimensions of an air-cored multilayer coil is illustrated on the Figure 3.1.

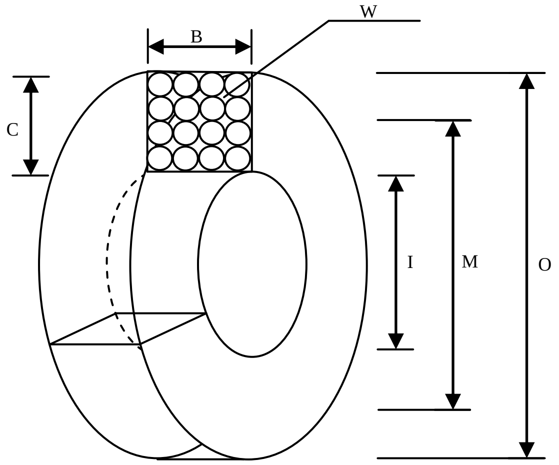

Figure 3.1: Geometry of an air- cored multilayer coil.

We designate the coil with the dimensions on Table 3.1. We calculate the inductance of an air-cored multilayer coil via Wheeler's formula, [38].

Dimensions	**Value (mm)**
C (radial thickness)	125 mm
B(width or length)	100
W (diameter of the copper wire)	To be determined
I (inner diameter)	250
M (mean diameter)	375
O (outer diameter)	500

Table 3.1: Dimensions of the coil.

According to Wheeler's formula, the design starts with the determination of the inductance of the coil. Then the number of the windings is calculated and the American Wire Gauge (AWG) number of the copper wire is decided. DC resistance (R) of the wire is calculated either. P is linear packing density (the wire diameter divided with the centre-to-centre wire spacing). P is taken as 0.8. We decide 50 milliHenry for the inductance value of the coil. The necessary design values are calculated by using the following equations:

$$L = \frac{7.87 \times N^2 \times M^2}{3 \times M + 9 \times B + 10 \times C} \tag{3.1}$$

$$N \times \left(\frac{W}{P} \right)^2 = B \times C \tag{3.2}$$

$$R = \frac{N \times M}{14250 \times W^2} \tag{3.3}$$

When we solve the equation (3.1) for N, we have 384 numbers of windings. When we solve the equation (3.2) with this N for W, we have 4.56mm diameter of the wire. We choose AWG 5 wire whose diameter is 4.621mm which is close to the calculated one. We re-calculate C (radial thickness) with this new W via the equation (3.2). We re-calculate the inductance of the coil with this new C (radial thickness), and M (mean diameter) and we find 50.034 millihenry which is closely 50 millihenry. We calculate the DC resistance (R) of the copper wire via the equation (3.3) and find 0.47Ω. Then, we calculate the impedance of the coil at 600 Hz as $Z = w \times L = 2 \times \pi \times f \times L = 2 \times \pi \times 600 \times 0.05 = 188\Omega$. The power required to drive the coil is $P = V \times I = I^2 \times R = 1^2 \times 188 = 188W$. This power consumption is plausible for an underwater system. In the thesis we make use of this coil through the simulations.

Dimensions	**Value (mm)**
C (radial thickness)	128
B (width or length)	100
W (diameter of the copper wire, AWG5)	4.621
I (inner diameter)	250
M (mean diameter)	378
O (outer diameter)	506

Table 3.2: New dimensions of the coil.

N (number of winding)	384 turns
L (inductance)	50 mH
Z (impedance @ 600Hz)	188 Ω
R (DC resistance)	0.47Ω

Table 3.3: Number of winding and impedance values of the coil.

Chapter 4

CASE STUDIES

In this chapter, detailed analyses of magnetic field of the air cored multilayer coil using 2D axial symmetric and 3D simulation of FEM models developed in COMSOL Multiphysics are presented. In addition, analyses of perturbation of ambient Earth magnetic field due to a submarine as well as analysis of magnetic field of DC current carrying wire are presented. In each section these models are described with respect to all aspects of FEM: geometry, physics, boundary condition and mesh. The computer used for the FEM simulations needs to be powerful in terms of central processing unit (CPU) and needs to have big random access memory (RAM) to be able generate finer meshes and solve larger matrices. The properties of the computer we used is illustrated on the Table 4.1.

Manufacturer:	Hewlett-Packard Company
Model:	HP Z800 Workstation
Processor:	Intel(R) Xeon(R) CPU X5675
	@3.07GHZ 3.06GHZ (2 processors)
Installed memory (RAM):	64GB
System type:	64-bit Operating System

Table 4.1: Properties of the computer used for the simulations.

4.1 Magnetic Field of a Coil

In this section, low frequency magnetic field of the air-cored multilayer coil in seawater and in air for three different frequencies of 500Hz, 1 kHz and 10 kHz are studied in COMSOL Multiphysics. We observe the variations of the magnetic flux density of the coil with respect to the three different frequencies and seawater. The applied current to the coil is 1 Ampere. We take a cylinder as a solution domain as illustrated on the Figure 4.1. The diameter and the height of the cylinder is 50m. We put the coil in the solution domain as seen on the Figure 4.1 to have 2D axial symmetry. The coil is z-directed and at the origin of the cylinder. The symmetry provides the problem to be solved with less physical memory and processing power of the personal computer. This is an advantage over 3D asymmetric geometries. In the model we put the coil into a case (cylinder). This cylinder has 30cm radius and 15cm height and inside of it is air. The case has no thickness. The coil, case and the medium can be seen in 2D axial symmetry on the Figure 4.2.

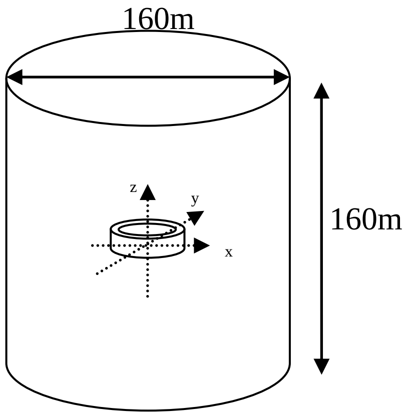

Figure 4.1: The coil in the solution medium.

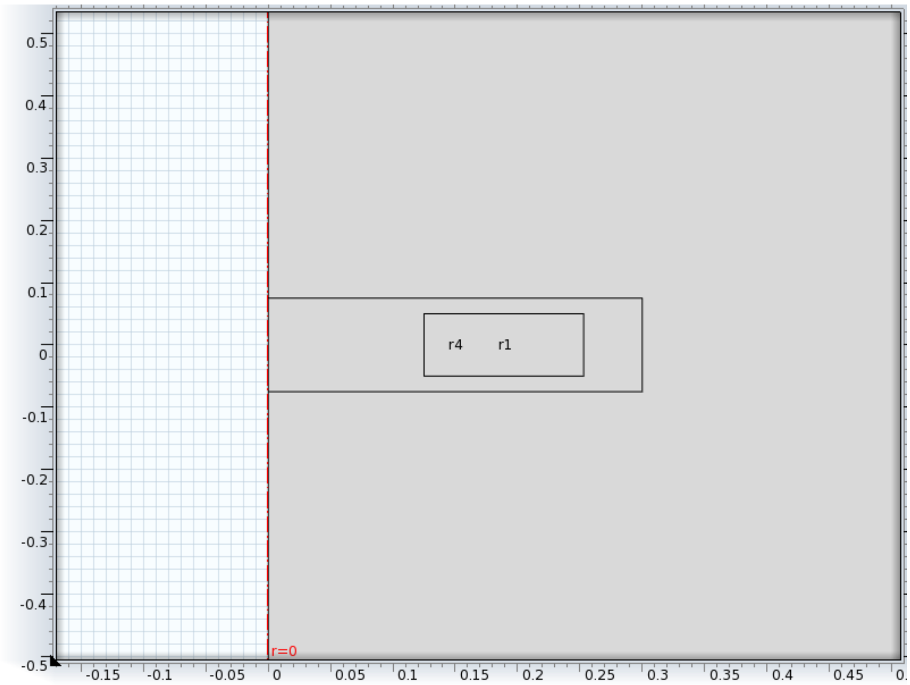

Figure 4.2: Coil, case and the solution domain in 2D view.

After modeling the geometry of the coil, *Magnetic Fields* interface is added under the *AC/DC* branch for the physics selection of the model. This interface solves the equation (2.12).

After adding physics for the model, we assign boundary conditions to the coil, case and outer boundary of the solution domain enclosing the coil geometry. Ampere's Law is assigned to the coil and the case. In this condition, μ_r is taken 1; σ is taken zero and ε_r is taken 1 since these domains are air. For the solution domain enclosing the coil geometry we assign Ampere's Law, too. If the solution medium is air, μ_r is taken 1; σ is taken zero and ε_r is taken 1. If the solution medium is seawater, μ_r is taken 1, σ is taken 4 (S/m) and ε_r is taken 80. Boundary condition assigned to the edges of the solution medium is magnetic insulation. The equation solved on this boundary is $n \times A = 0$. We set the tangential component of vector magnetic potential of these boundaries to zero. In order to excite the coil, external current density is assigned to the coil domain. The coil is excited in phi direction with respect to 2D axial symmetry.

After adding physics and boundary condition, we generate a mesh for the model in order to discretize the complex geometry of the coil into triangular elements. In order to get accurate results, in any wave problems, it is vital that wavelength must be taken into account while generating meshes. According to [39], maximum element size of the mesh elements must be at least one fifth of the wavelength at the operating frequency. The meshing of coil, case and the medium is on the Figure 4.3.

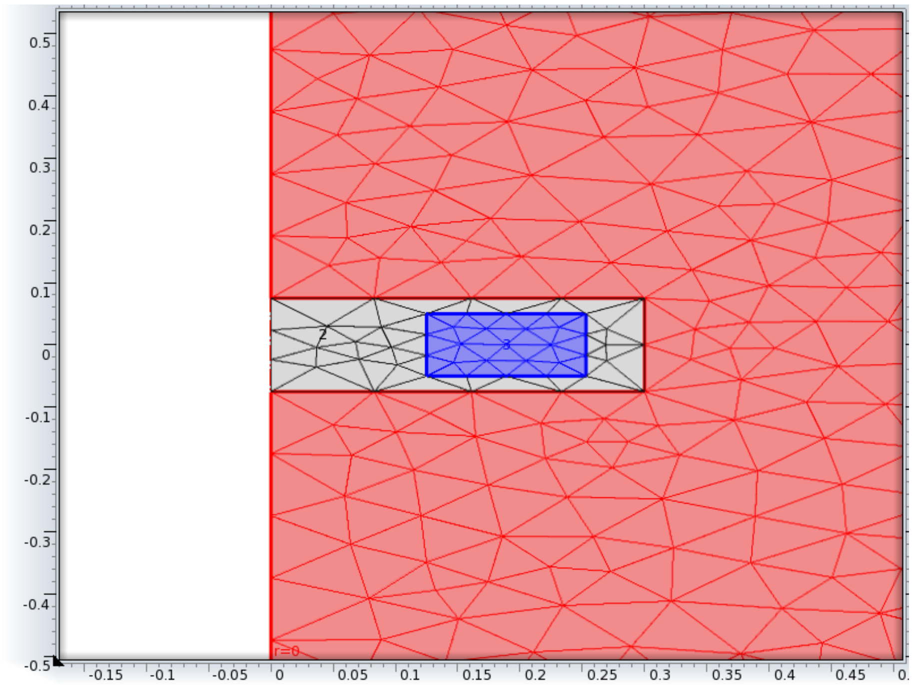

Figure 4.3: Generated mesh of the coil, case and the medium.

As the last step, we add frequency domain as study step and solver sequence for the model so as to compute the solution.

We start post-processing of the magnetic flux density of the coil. Firstly we observe the magnetic flux density of the coil on an arch. As can be seen on the Figure 4.4, the observation arch is 1 meter away from the center of the coil from 0^0 to 90^0. The following plots show the change of the magnetic flux density norm of the coil on the arc when the frequencies are 500 Hz, 1 kHz, 10 kHz and the medium is air and seawater.

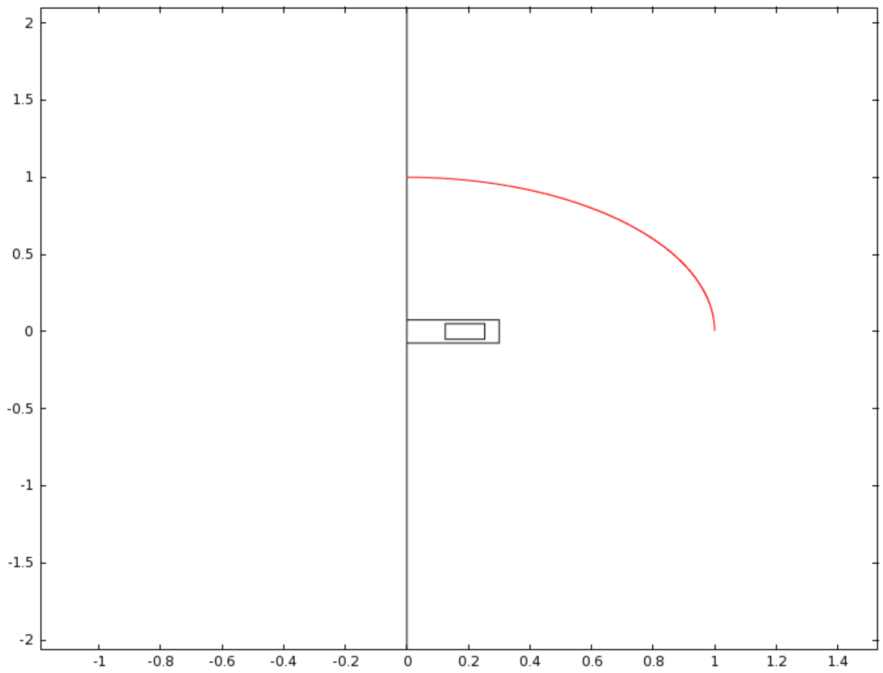

Figure 4.4: Observation arch: one meter from the center of the coil from 0^0 to 90^0.

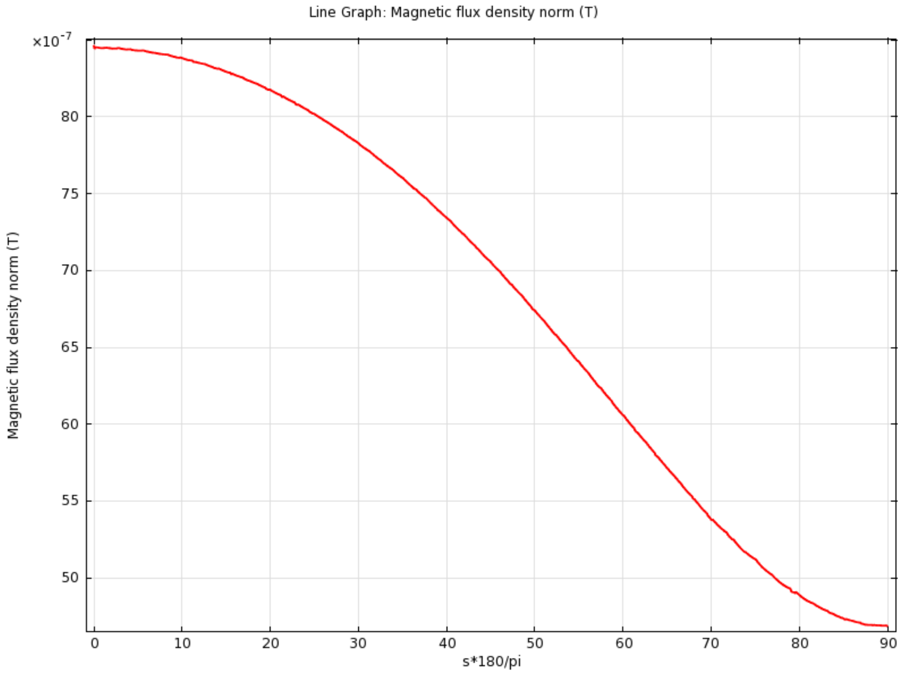

Figure 4.5: All three frequencies on the same plot (in air).

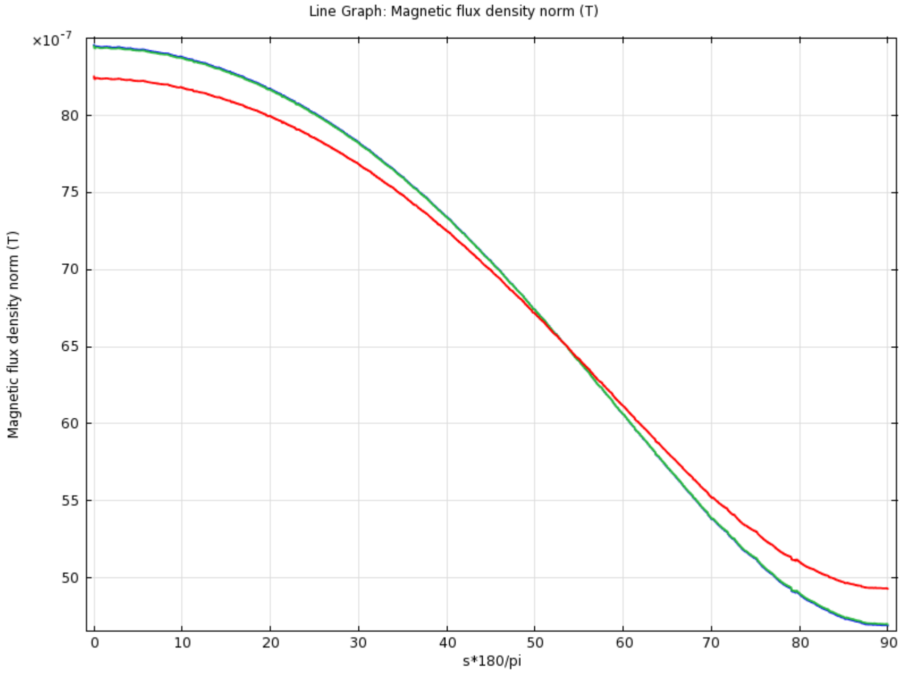

Figure 4.6: All three frequencies on the same plot (in seawater).

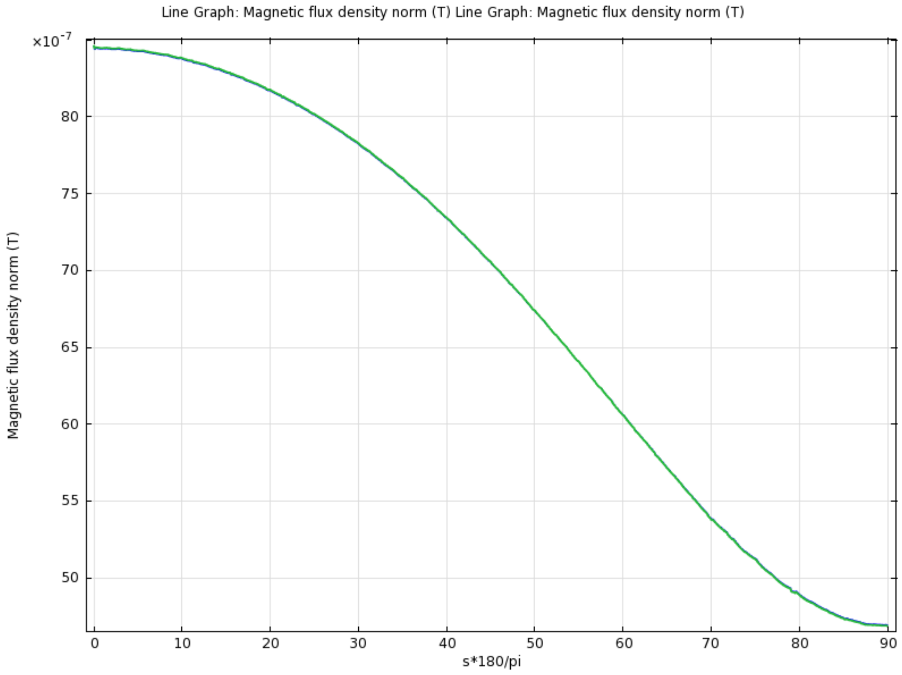

Figure 4.7: Frequency 500 Hz in air and seawater.

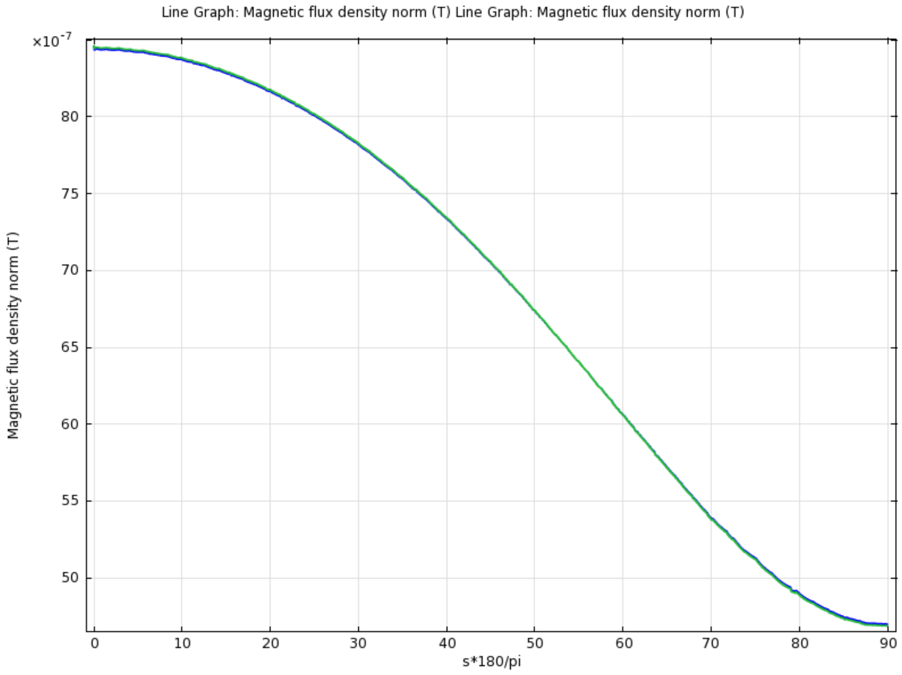

Figure 4.8: Frequency 1 kHz in air and seawater.

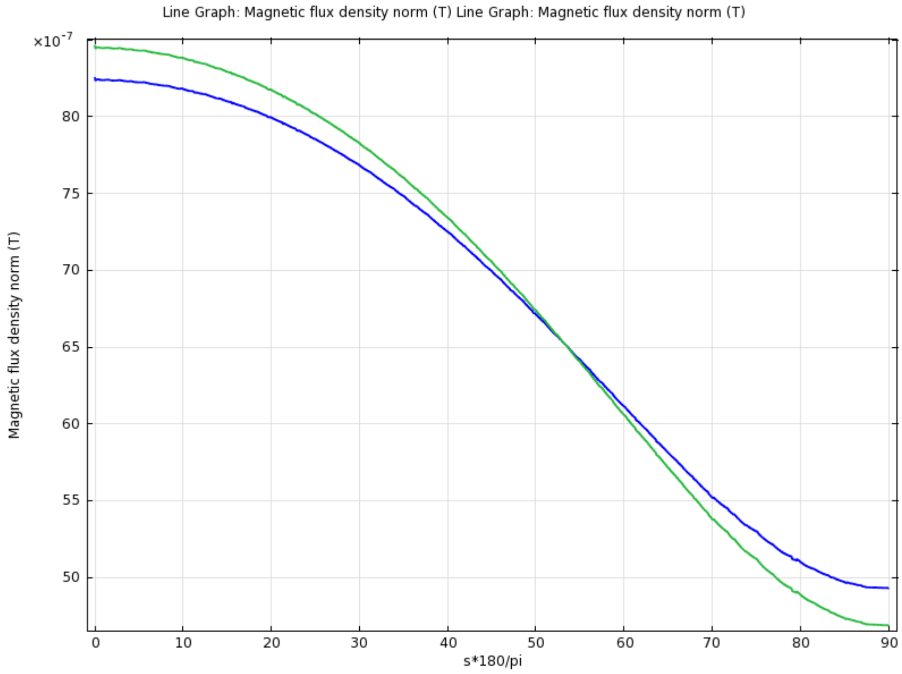

Figure 4.9: Frequency 10 kHz in air (green) and seawater (blue).

Comparisons of the magnetic flux density of the coil for three frequencies in air and in seawater are illustrated on the preceding plots. We observe on the plots that the magnetic flux density norm is maximum at 0^0 (r =0, z= 1) and minimum at 90^0 (r =1, z= 0) in one meter distance. Magnetic flux density norm at 0^0 (r =0, z= 1) is almost two fold of magnetic flux density norm at 90^0 (r =1, z= 0). As seen on the Figure 4.5, in air for three frequency (500 Hz, 1 kHz and 10 kHz) curves coincide, on the other hand as seen on the Figure 4.6, in seawater 500 Hz and 1 kHz are close to each other and 10 kHz differs from them. Blue curve is 500Hz, the frequency of green curve is 1 kHz and the frequency of red curve is 10 kHz. As the frequency increases, ratio of the magnetic flux density at 0^0 to 90^0 decreases. As seen on the Figure 4.7 and Figure 4.8, in air and seawater for 500 Hz and 1 kHz respectively, magnetic flux densities of the coil on the arc coincide. As illustrated on the Figure 4.9, in air and seawater magnetic flux density of the coil differ from each other.

Secondly; we observe the magnetic flux density of the coil on an observation line which is from the center of the coil to 80m at 0^0 (r=0, z=0 to r=0, z=80m). This observation line is illustrated on the Figure 4.10. Wavelength (λ) of electromagnetic wave in seawater is 70m when the frequency is 500 Hz, 50m when the frequency is 1 kHz and 16m when the frequency is 10 kHz. In the following plots, we observe the attenuation of magnetic flux density of the coil in air and seawater for each frequency.

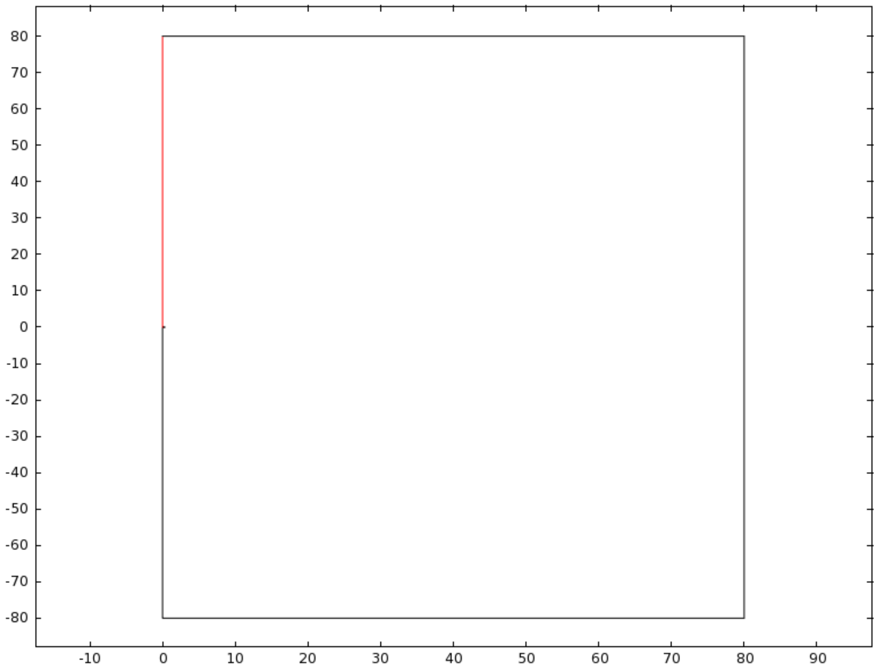

Figure 4.10: Observation line: Red line from the origin of the coil to 80m @ 0^0 (r=0, z=0 to r=0, z=80m).

When we plot the magnetic flux density of the coil through this observation line for three frequencies (500 Hz, 1 kHz and 10 kHz) in air and seawater, we see that all of the plots coincide; it is not possible to discriminate them from each other. This plot is illustrated on the Figure 4.11. In order to be able to discriminate the plots, we plot them for three different frequencies and two mediums in the following figures.

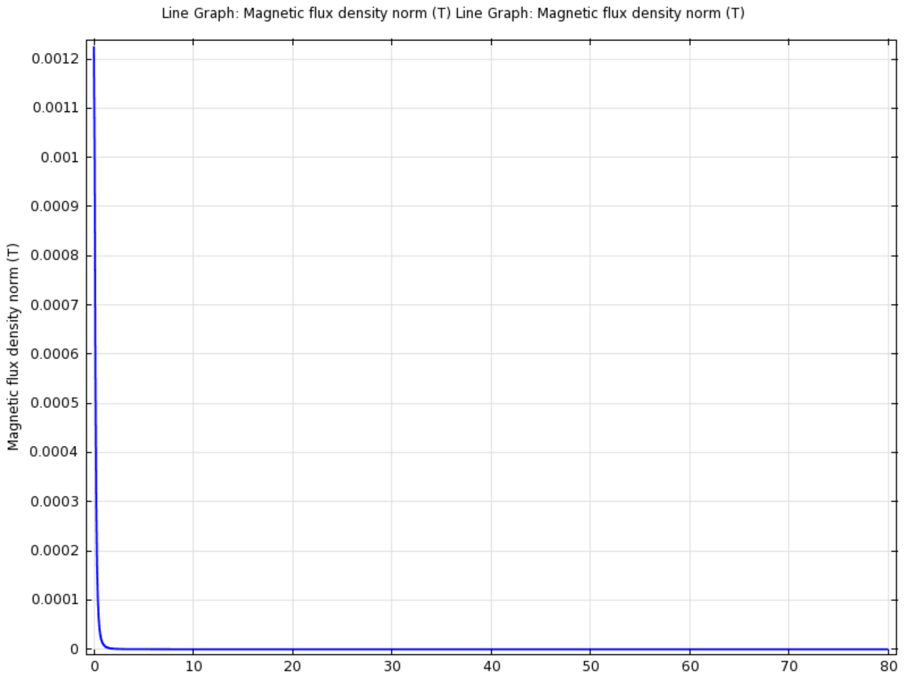

Figure 4.11: All three frequencies (500 Hz, 1 kHz and 10 kHz) in air and seawater.

When the frequency is 500 Hz, wavelength (λ) of electromagnetic wave in seawater is 70m. Comparison of the magnetic flux density of the coil in air and seawater through the line (r=0, z=[69:71]) is illustrated on the Figure 4.12. Magnetic flux density in seawater is 5.0639×10^{-13} (T) and in air is 1.1729×10^{-11} (T) at the point (r=0, z=70m). In one wavelength, the magnetic flux density of the coil attenuates 62.8dB in seawater with respect to in air.

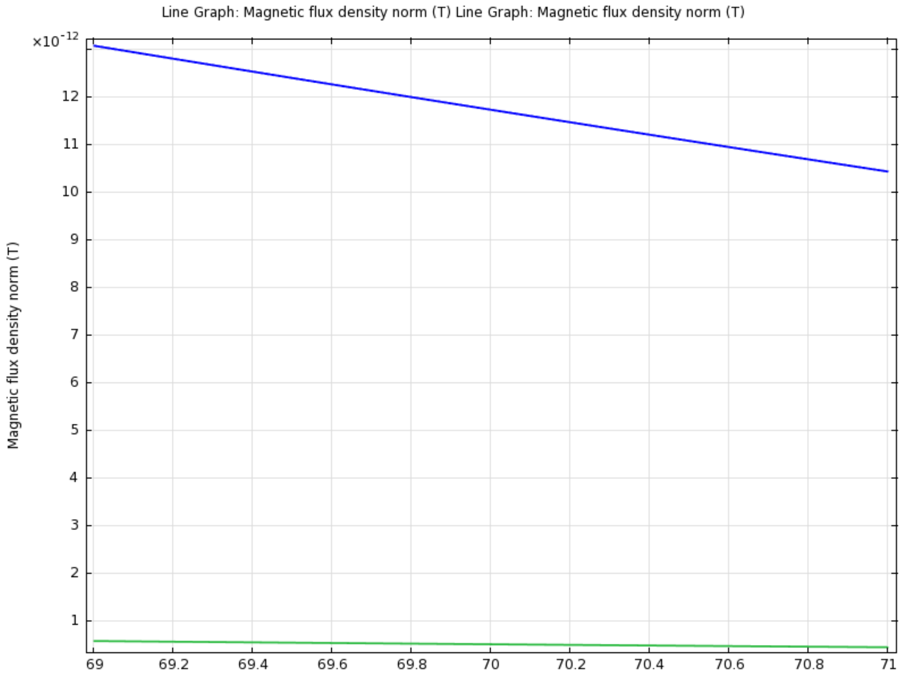

Figure 4.12: Frequency 500 Hz in air (blue) and seawater (green).

When the frequency is 1 kHz, wavelength (λ) of electromagnetic wave in seawater is 50m. Comparison of the magnetic flux density of the coil in air and seawater through the line (r=0, z=[49:51]) is illustrated on the Figure 4.13. Magnetic flux density in seawater is 1.2856×10^{-12} (T) and in air is 5.8812×10^{-11} (T) at the point (r=0, z=50m). In one wavelength, the magnetic flux density of the coil attenuates 76.4dB in seawater with respect to in air.

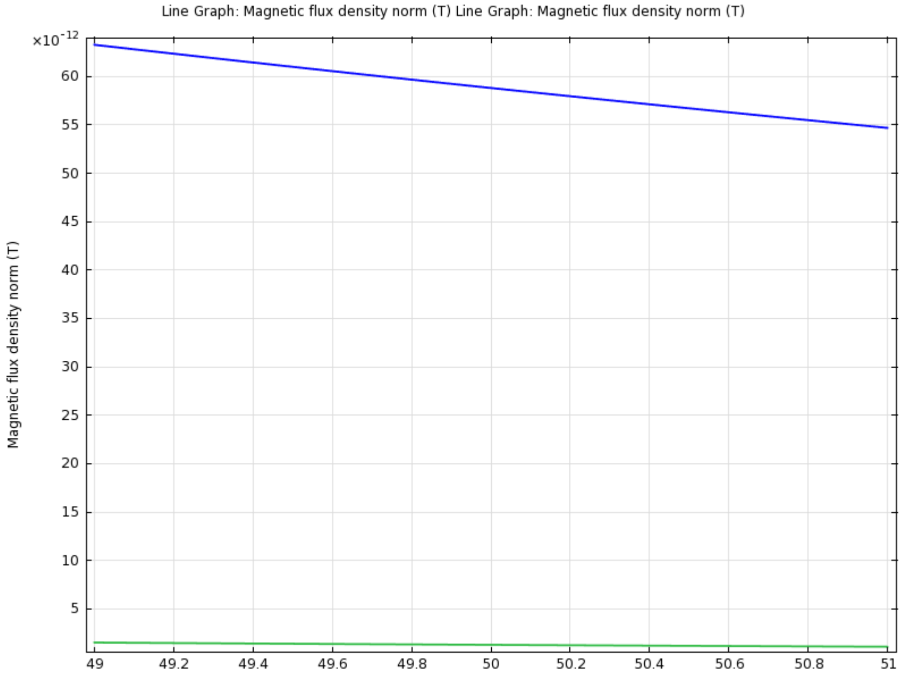

Figure 4.13: Frequency 1 kHz in air (blue) and seawater (green).

When the frequency is 10 kHz, wavelength (λ) of electromagnetic wave in seawater is 16m. Comparison of the magnetic flux density of the coil in air and seawater through the line (r=0, z=[15:17]) is illustrated on the Figure 4.14. Magnetic flux density in seawater is 3.6698×10^{-11} (T) and in air is 2.1699×10^{-9} (T) at the point (r=0, z=16m). In one wavelength, the magnetic flux density of the coil attenuates 81.5dB in seawater with respect to in air.

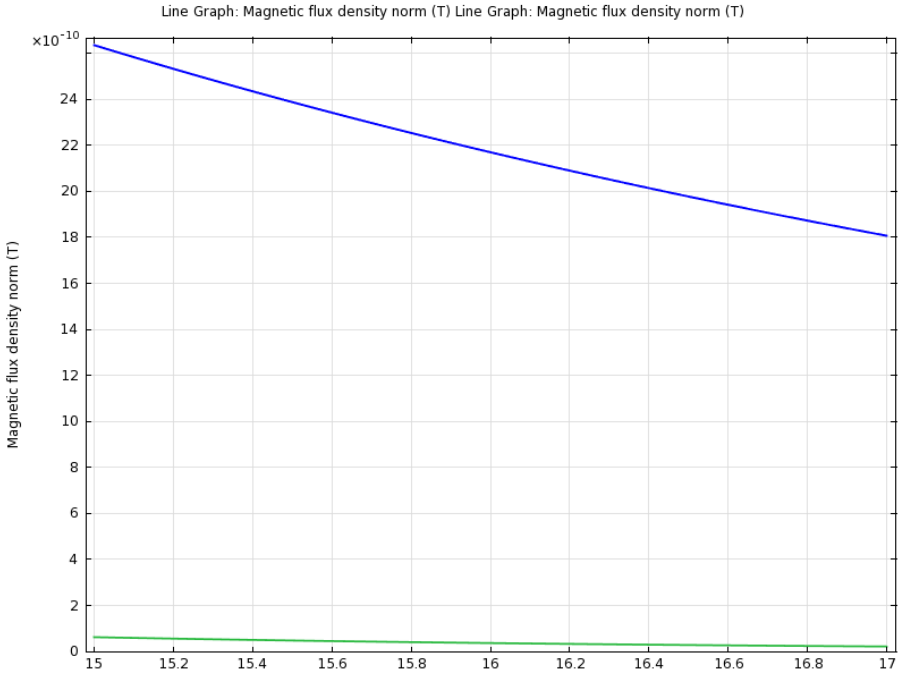

Figure 4.14: Frequency 10 kHz in air (blue) and seawater (green).

4.2 Magnetic Field of a Shielded Coil

Detectors, sensors and electronic circuitries of underwater systems are isolated from seawater via water proof cases due to the fact that submerging the system into seawater without isolating it from seawater damages the components of the electronic systems. There are different decision criterions in the selection of the material of the case of the underwater systems. The material of case has to be water proof, hard, durable and rustproof. Selection of the material of the case is also a vital decision step when the concerns of electromagnetic interference are taken into account. The material of the case can affect the magnetic field of the coil according to its electrical properties. Due to the electrical properties of the case that are electrical conductivity (σ) and relative permeability (μ_r), the strength of the magnetic field can be attenuated. The attenuation of the magnetic field of the coil is not only due to the permeability of the material of the case but also eddy currents that are created on the surface of case. This effect is called the shielding effect of the case on the magnetic field strength of the coil. In this section, the effect of the electrical conductivity of the material of the case and different thicknesses of the case on the magnetic flux density of the coil is studied. We disregard permeability of the material of the case and other electromagnetic interference sources. The studied materials are copper (Cu), aluminum (Al), stainless steel and carbon mixed composite. These materials have relative permeability (μ_r) 1 and relative permittivity (ε_r) 1 but they have different electrical conductivity values.

We begin the analysis with the designation of the geometry of the models in COMSOL Multiphysics. We take a solution domain as a cylinder whose height is 50m, radius is 25m. We take the case whose inner length is 50cm and inner radius is 25.5cm. We take a gap distance of 2mm between the outer radius of the coil and the inner radius of the case. Two dimensional axial symmetric views of the case, coil and the solution medium are on the Figure 4.15.

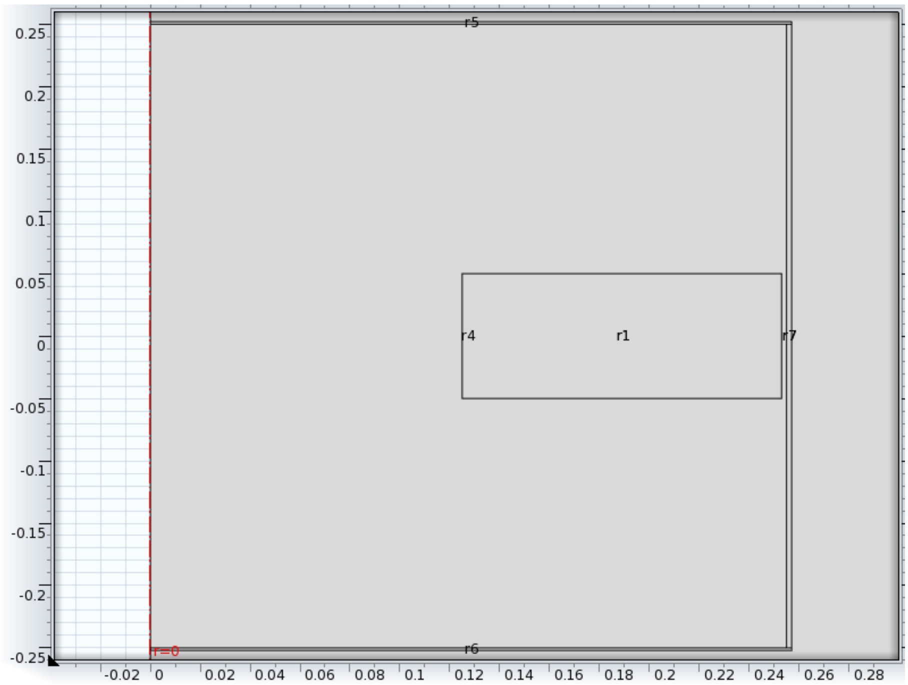

Figure 4.15: Coil, case and the solution medium.

After modeling the geometry of the coil and the case, *Magnetic Fields* interface is added under the *AC/DC* branch for the physics selection of the model. The equation solved in this interface is the equation (2.12).

After adding physics for the model, we have to assign boundary conditions to the coil, the case and the solution domain enclosing the coil and the case geometries. For the solution domain enclosing the coil and the case geometries we assign Ampere's Law. The solution medium is seawater, μ_r is taken 1, σ is taken 4 (S/m) and ε_r is taken 80 in this domain. The coil domain and inner of the case domain are taken air, μ_r is taken 1, σ is taken zero and ε_r is taken 1 in these domains. Thickness domain of the case is the interested material. We assign Ampere's Law in this domain too. In this domain, μ_r is taken 1, and ε_r is taken 1. Electrical conductance (σ) varies according to the material chosen. Boundary condition of the edges of the solution medium is magnetic insulation. The equation solved on these edges is $n \times A = 0$. We set the tangential component of vector magnetic potential of these boundaries to zero. In order to excite the coil, external current density is assigned to the coil domain. The coil is excited in phi direction with respect to 2D axial symmetry.

After adding physics and boundary condition, we generate a mesh for the model in order to discretize the complex geometry of the coil into triangular elements.

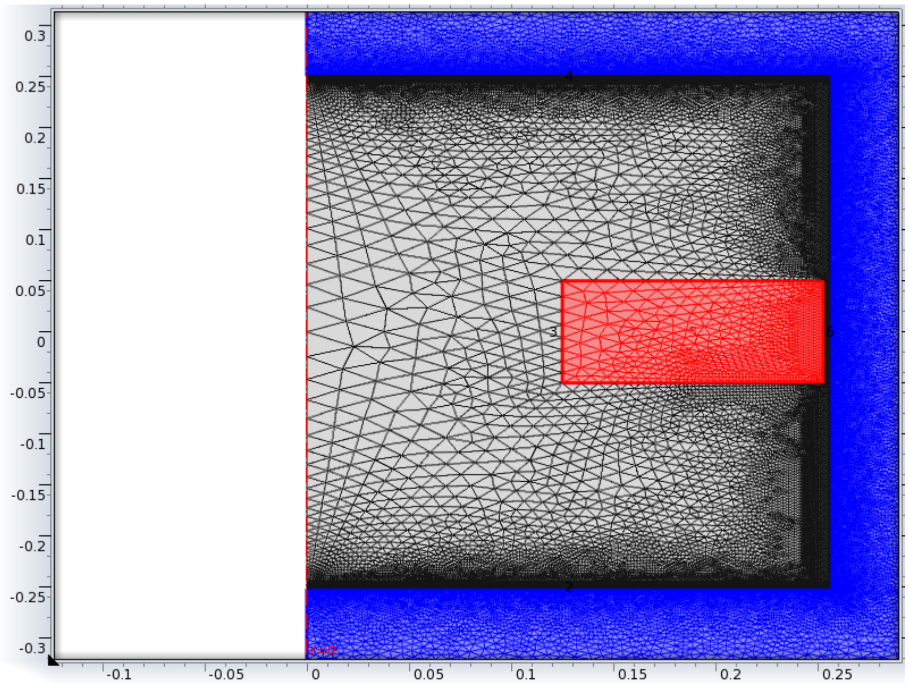

Figure 4.16: Generated mesh of the coil, case and the solution medium.

As the last step, we add frequency domain as study step and solver sequence for the model so as to compute the solution.

We study the shielding effect of thicknesses for 2mm and 1mm of the case for three frequencies of 500Hz, 1 kHz and 10 kHz. Observation points of shielding effect are on the Figure 4.17. Firstly, we observe the effect of the 2mm thickness of the case for different materials, different electrical conductance values and frequencies on the magnetic flux density norm at two points: (r=0, z=1) and (r=1, z=0). Secondly, we observe the magnetic flux density of the coil for 1mm thickness of the case.

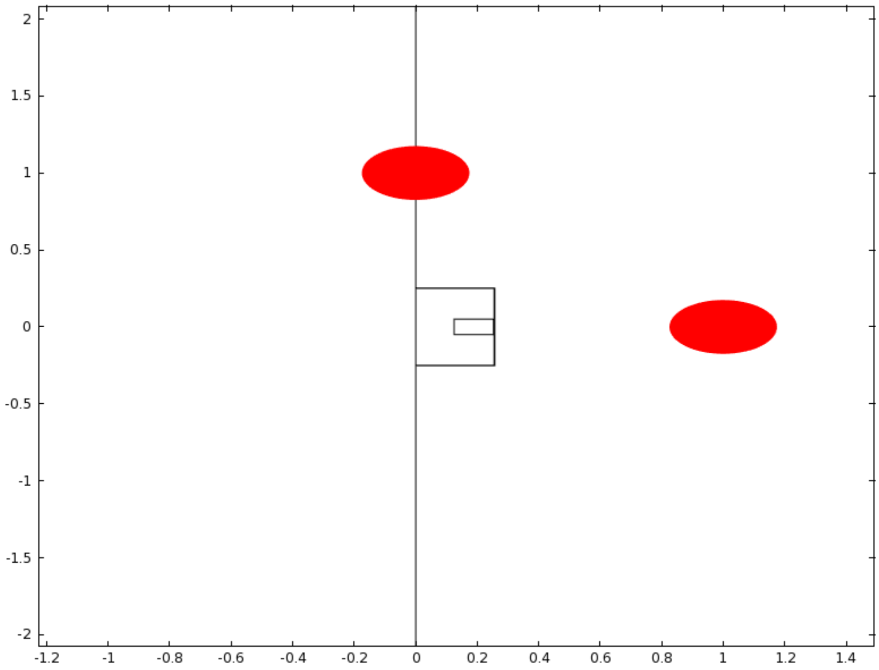

Figure 4.17: Observations points (r=0, z=1 and r=1, z=0).

Case material	**Conductivity(S/m) @ 20^{0}C**	**Frequency (Hz)**	**Magnetic Flux Density norm (T)**	
			r=0, z=1m	**r=1m, z=0**
Copper(Cu)	5.96 x 10^7	500	1.3699e-7	1.0351e-7
		1000	6.7401e-8	5.1074e-8
		10000	4.5253e-9	3.6928e-9
Aluminum(Al)	3.50 x 10^7	500	2.3432e-7	1.768e-7
		1000	1.163e-7	8.8082e-8
		10000	7.2914e-9	5.9265e-9
Stainless Steel	1.45 x 10^6	500	5.3457e-6	3.1649e-6
		1000	2.9805e-6	1.9503e-6
		10000	2.7577e-7	2.2317e-7
Carbon (perpendicular to base plane)	2 to 3x 10^5	500	8.4687e-6	4.7129e-6
		1000	7.9626e-6	4.4718e-6
		10000	1.6638e-6	1.2611e-6
Carbon (parallel to base plane)	3.3x 10^2	500	8.6554e-6	4.8054e-6
		1000	8.649e-6	4.8125e-6
		10000	8.4446e-6	5.05e-6

Table 4.2: Magnetic Flux Density norm of the coil for 2mm thickness for different materials.

Conductivity(S/m)	**Frequency (Hz)**	**Magnetic Flux Density norm (T)**	
		r=0, z=1m	**r=1m, z=0**
0.01	500	8.6554e-6	4.8054e-6
	1000	8.649e-6	4.8125e-6
	10000	8.4449e-6	5.0502e-6
0.1	500	8.6554e-6	4.8054e-6
	1000	8.649e-6	4.8125e-6
	10000	8.4449e-6	5.0502e-6
1	500	8.6554e-6	4.8054e-6
	1000	8.649e-6	4.8125e-6
	10000	8.4449e-6	5.0502e-6
10	500	8.6554e-6	4.8054e-6
	1000	8.649e-6	4.8125e-6
	10000	8.4448e-6	5.0502e-6
1e2	500	8.6554e-6	4.8054e-6
	1000	8.649e-6	4.8125e-6
	10000	8.4448e-6	5.0501e-6
1e3	500	8.6554e-6	4.8054e-6
	1000	8.649e-6	4.8125e-6
	10000	8.4433e-6	5.0493e-6
1e4	500	8.6551e-6	4.8053e-6
	1000	8.6477e-6	4.8119e-6
	10000	8.3244e-6	4.9853e-6
1e5	500	8.6247e-6	4.7903e-6
	1000	8.5282e-6	4.7525e-6
	10000	4.1056e-6	2.7165e-6
5e5	500	7.9686e-6	4.4652e-6
	1000	6.5538e-6	3.773e-6
	10000	8.1019e-7	6.4479e-7
1e6	500	6.5582e-6	3.7673e-6
	1000	4.1944e-6	2.5897e-6
	10000	4.0108e-7	3.2365e-7
2e6	500	4.1966e-6	2.5854e-6
	1000	2.1473e-6	1.4779e-6
	10000	1.9945e-7	1.6164e-7
3.5e6	500	2.4668e-6	1.6604e-6
	1000	1.1967e-6	8.7419e-7
	10000	1.133e-7	9.1938e-8
5e6	500	1.7007e-6	1.2025e-6
	1000	8.297e-7	6.1685e-7
	10000	7.8715e-8	6.3905e-8
8e6	500	1.0433e-6	7.6666e-7
	1000	5.1516e-7	3.8711e-7
	10000	4.8156e-8	3.911e-8
1e7	500	8.3024e-7	6.1596e-7
	1000	4.1132e-7	3.099e-7
	10000	3.7798e-8	3.0702e-8
1.5e7	500	5.5026e-7	4.1221e-7
	1000	2.7344e-7	2.0661e-7
	10000	2.367e-8	1.923e-8
2e7	500	4.1162e-7	3.0947e-7
	1000	2.0468e-7	1.5483e-7

	10000	1.6399e-8	1.3324e-8
3e7	500	2.7365e-7	2.0633e-7
	1000	1.3596e-7	1.0295e-7
	10000	9.1676e-9	7.4497e-9
5e7	500	1.6359e-7	1.2356e-7
	1000	8.0814e-8	6.1229e-8
	10000	4.8622e-9	3.9607e-9
1e8	500	8.088e-8	6.1149e-8
	1000	3.8811e-8	2.9419e-8
	10000	4.6366e-9	3.7941e-9

Table 4.3: Magnetic Flux Density norm of the coil for 2mm thickness for different conductivities of the material of the case.

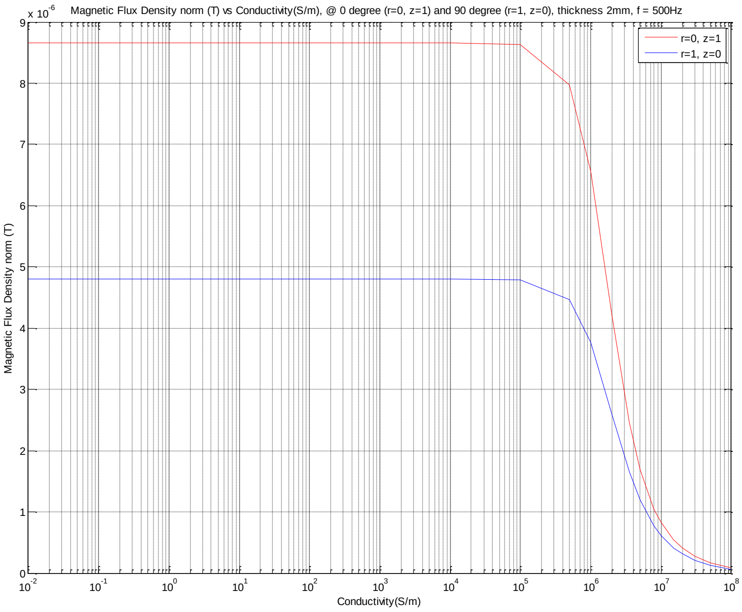

Figure 4.18: Magnetic Flux Density norm (T) vs Conductivity(S/m), f = 500Hz.

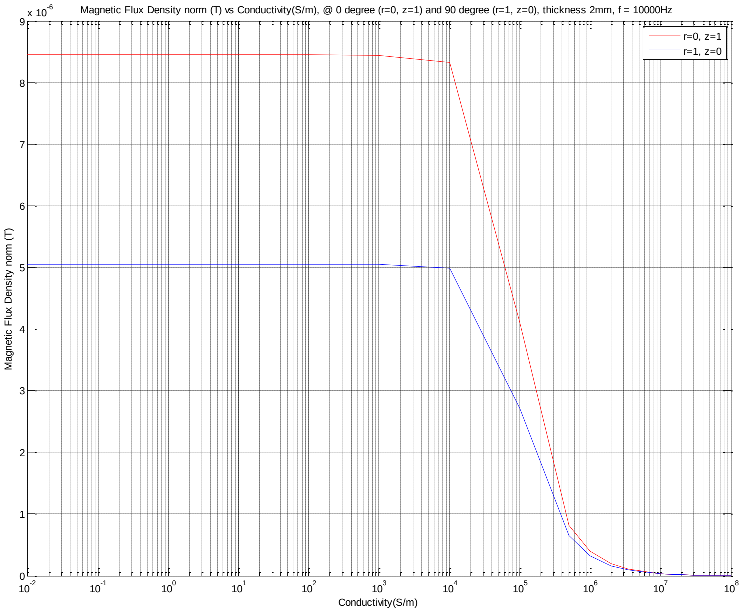

Figure 4.19 : Magnetic Flux Density norm (T) vs Conductivity(S/m), f = 10000Hz.

Secondly, we repeat the calculations for 1mm thickness of the case.

Case material	**Conductivity(S/m) @ 20^{0}C**	**Frequency (Hz)**	**Magnetic Flux Density norm (T)**	
			r=0, z=1m	**r=1m, z=0**
Copper(Cu)	5.96 x 10^7	500	2.7633e-7	2.0751e-7
		1000	1.3768e-7	1.0383e-7
		10000	1.1955e-8	9.6731e-9
Aluminum (Al)	3.50 x 10^7	500	4.7204e-7	3.5299e-7
		1000	2.3493e-7	1.7692e-7
		10000	2.1909e-8	1.7725e-8
Stainless Steel	1.45 x 10^6	500	7.3653e-6	4.1575e-6
		1000	5.3462e-6	3.1647e-6
		10000	5.564e-7	4.4532e-7
Carbon (perpendicular to base plane)	2 to 3x 10^5	500	8.6117e-6	4.7734e-6
		1000	8.4663e-6	4.7116e-6
		10000	3.3707e-6	2.2997e-6
Carbon (parallel to base plane)	3.3x 10^2	500	8.6594e-6	4.797e-6
		1000	8.653e-6	4.8041e-6
		10000	8.4488e-6	5.0417e-6

Table 4.4: Magnetic Flux Density norm for 1mm thickness for different materials.

Conductivity(S/m)	**Frequency (Hz)**	**Magnetic Flux Density norm (T)**	
		r=0, z=1m	**r=1m, z=0**
0.01	500	8.6594e-6	4.797e-6
	1000	8.653e-6	4.8041e-6
	10000	8.4488e-6	5.0418e-6
0.1	500	8.6594e-6	4.797e-6
	1000	8.653e-6	4.8041e-6
	10000	8.4488e-6	5.0418e-6
1	500	8.6594e-6	4.797e-6
	1000	8.653e-6	4.8041e-6
	10000	8.4488e-6	5.0418e-6
10	500	8.6594e-6	4.797e-6
	1000	8.653e-6	4.8041e-6
	10000	8.4488e-6	5.0418e-6
1e2	500	8.6594e-6	4.797e-6
	1000	8.653e-6	4.8041e-6
	10000	8.4488e-6	5.0418e-6
1e3	500	8.6594e-6	4.797e-6
	1000	8.653e-6	4.8041e-6
	10000	8.4484e-6	5.0415e-6
1e4	500	8.6593e-6	4.797e-6
	1000	8.6527e-6	4.8039e-6
	10000	8.4175e-6	5.0248e-6
1e5	500	8.6517e-6	4.7932e-6
	1000	8.6223e-6	4.7889e-6
	10000	6.405e-6	3.95e-6
5e5	500	8.4727e-6	4.7047e-6
	1000	7.9667e-6	4.4641e-6
	10000	1.6664e-6	1.2588e-6
1e6	500	7.9727e-6	4.4575e-6
	1000	6.5578e-6	3.7667e-6
	10000	8.1181e-7	6.4367e-7
2e6	500	6.5622e-6	3.7609e-6
	1000	4.1979e-6	2.5852e-6
	10000	4.0207e-7	3.2319e-7
3.5e6	500	4.6763e-6	2.8225e-6
	1000	2.4687e-6	1.6601e-6
	10000	2.2895e-7	1.8472e-7
5e6	500	3.4433e-6	2.1888e-6
	1000	1.7025e-6	1.2022e-6
	10000	1.6001e-7	1.2925e-7
8e6	500	2.1512e-6	1.4727e-6
	1000	1.0446e-6	7.6636e-7
	10000	9.9781e-8	8.0663e-8
1e7	500	1.7034e-6	1.2003e-6
	1000	8.3136e-7	6.1573e-7
	10000	7.9703e-8	6.4447e-8
1.5e7	500	1.1171e-6	8.1485e-7
	1000	5.5109e-7	4.1209e-7
	10000	5.2889e-8	4.2777e-8
2e7	500	8.319e-7	6.1483e-7
	1000	4.1232e-7	3.0943e-7

	10000	3.9423e-8	3.189e-8
3e7	500	5.5148e-7	4.1151e-7
	1000	2.7426e-7	2.064e-7
	10000	2.5839e-8	2.0904e-8
5e7	500	3.2966e-7	2.4731e-7
	1000	1.6423e-7	1.238e-7
	10000	1.4719e-8	1.1909e-8
1e8	500	1.6436e-7	1.2364e-7
	1000	8.1828e-8	6.1742e-8
	10000	6.0143e-9	4.8667e-9

Table 4.5: Magnetic Flux Density norm of the coil for 1mm thickness for different conductivities of the material of the case.

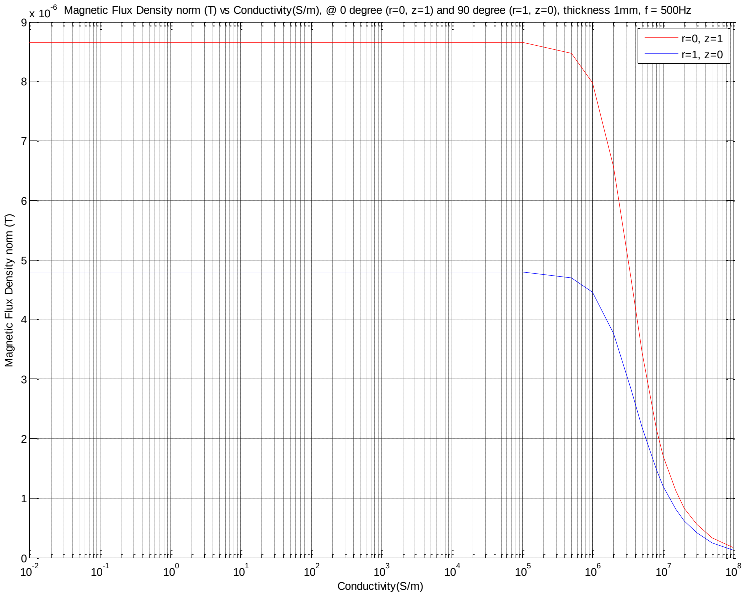

Figure 4.20: Magnetic Flux Density Norm (T) vs Conductivity(S/m), f = 500Hz.

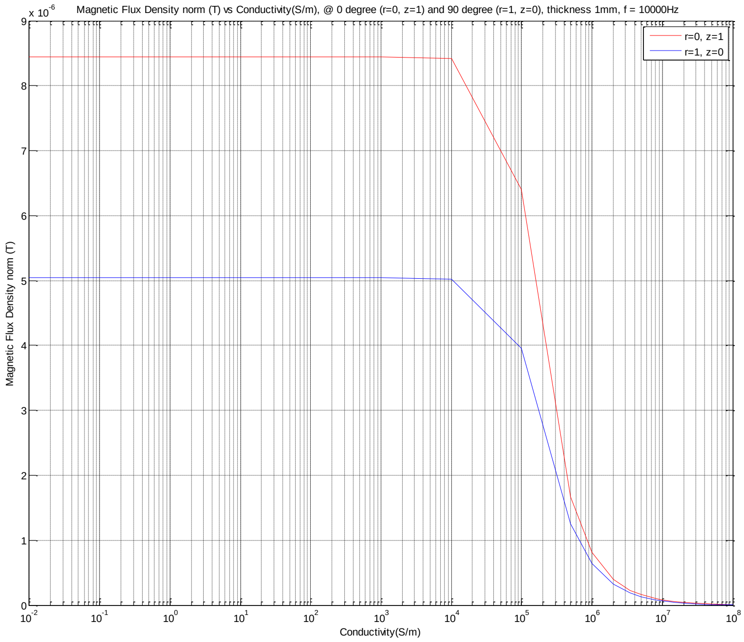

Figure 4.21: Magnetic Flux Density Norm (T) vs Conductivity(S/m), f = 10000Hz.

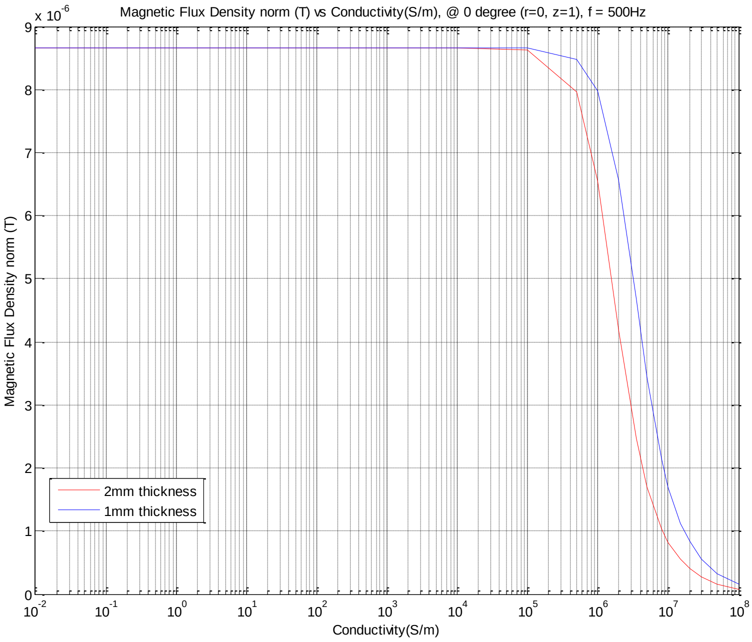

Figure 4.22: Effect of thickness @ 0^0 (r=0, z=1).

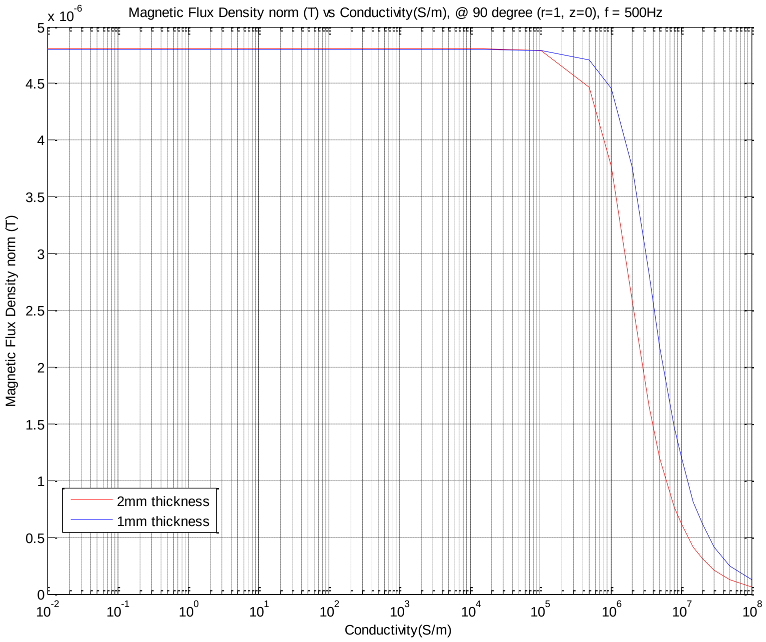

Figure 4.23: Effect of thickness @ 90^0 (r=1, z=0).

We observe the effect of the electrical conductivity of the material of the case and the effect of the thickness of the case on the magnetic flux density norm of the coil on the two observation points for two frequencies on the preceding figures. We observe on the Figure 4.18 to the Figure 4.23 that as the conductivity of the material of the case increases, magnetic flux density norm of the coil is unaffected until a certain value of the electrical conductivity in any two frequencies. After a certain electrical conductivity value, shielding effect of the case starts and the field attenuates rapidly. This critical value depends upon the thickness of the case and the frequency. As can be observed on the Figure 4.18, magnetic flux density norm of the coil decreases drastically after the conductivity exceeds 10^6 (S/m) when the frequency is 500Hz and the thickness of the case is 2mm. On the other hand, as it is illustrated on the Figure 4.19 drastic attenuation of the magnetic flux density norm starts when the conductivity of the material of the coil exceeds 10^4 (S/m) if the frequency is 10kHz. It can be concluded that as the frequency increases, attenuation starts for lower conductivity values of the material of the case. Final observation is that as can be seen on the Figure 4.22 and Figure 4.23 as the thickness of the case increases, shielding effect of the case increases, magnetic flux density norm of the coil decreases. To sum up, in order to avoid shielding effect of the material of the case, thin and low electric conducting material must be chosen. GRP and CRP have conductivity below 10^6 (S/m) and they would be good choice for the body of an underwater system. If the body would be metal, stainless steel whose conductivity is 1.45 x 10^6 (S/m) would have been an ideal case.

4.3 Perturbation of the Magnetic Field Due to a Metal Plate

In this section; we present the perturbation of the magnetic field of the coil due to a metal plate in seawater in COMSOL Multiphysics. We study how to detect the metal plate by measuring perturbation it creates on the magnetic flux density of the transmitting coil. The metal plate is the target. We study the metal plate in two cases: the material of the plate is iron and copper. We use the coil which is presented in chapter 3 as the transmitting coil in the model. The current applied to the coil is 1 Ampere 600Hz signal. Instead of using a receiving coil in the model, we solve x, y and z components of the magnetic flux density of the coil on an observation point. We investigate if the perturbations of the magnetic flux density of the coil on the observation point are able to be measured via a fluxgate magnetometer. We try to determine what kind of detection; in phase or quadrature, can be done for different metals.

We take a solution medium. The solution medium is illustrated on the Figure 4.24. This is an x-directed cylinder whose radius is 100m and height is 200m. Then, we take a target plate whose dimensions are 4cm thickness, 6m width and 12m length (0.04m x 6m x 12m).

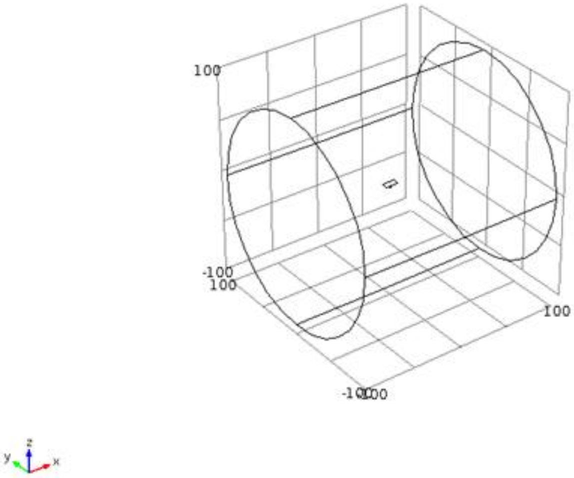

Figure 4.24: Solution medium.

We put the center of the plate on the domain to the point (x=0, y=0, z=3.52m). The plate is put parallel to x-y plane. The distance between the bottom surface of the plate and the origin is 3.5m. The coil is at the origin (0, 0, 0). The plate and the coil are illustrated on the Figure 4.25.

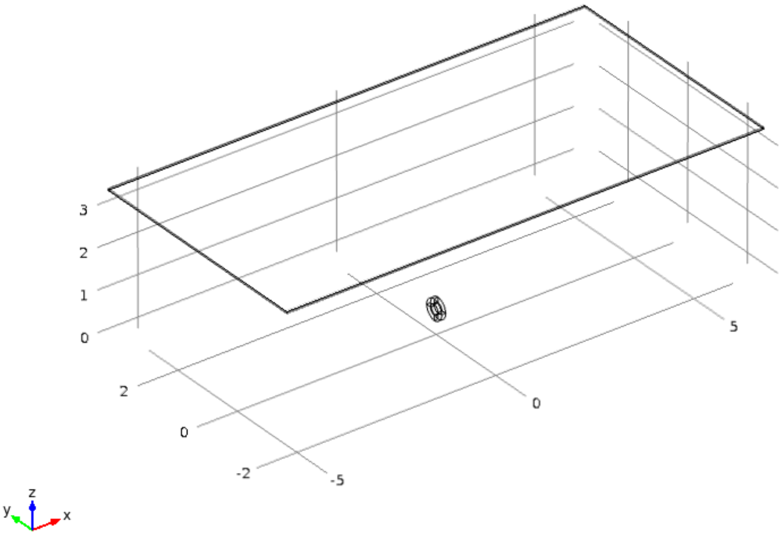

Figure 4.25: Coil and the metal plate.

After modeling the geometry of the coil, plate and solution domain, *Magnetic Fields* interface is added under the *AC/DC* branch for the physics section of the model in COMSOL Multiphysics. The equation solved in this interface is the equation (2.12).

After adding physics for the model, we have to assign boundary conditions to the coil, plate and outer boundary of the solution domain enclosing the coil and plate geometries. For the coil and the solution domain enclosing the coil we assign Ampere's Law. The solution medium is seawater, where relative permeability (μ_r) is 1, electrical conductivity (σ) is 4 (S/m) and relative permittivity (ε_r) is 80. The coil domain is air, where relative permeability (μ_r) is 1, electrical conductivity (σ) is 0.001 (zero is not allowed by COMSOL Multiphysics) and relative permittivity (ε_r) is 1. In order to validate the accuracies of the solutions we assign electrical properties of seawater (relative permeability (μ_r) 1, electrical conductivity (σ) 4 (S/m) and relative permittivity

(ε_r) 80) to the plate. Firstly we solve the magnetic flux density of the coil as if everywhere, except coil, is seawater. Boundary condition of the surfaces of the solution medium is magnetic insulation. The equation solved on these surfaces is $n \times A = 0$. We set the tangential component of vector magnetic potential of these boundaries to zero. In order to excite the coil, external current density is assigned to the coil domain.

After adding physics and boundary conditions, we generate a mesh for the model in order to discretize the geometry of the coil, plate and the solution medium into triangular and tetrahedral elements. From Figure 4.26 to Figure 4.28 illustrate the generated meshes for the coil, plate and the solution domain.

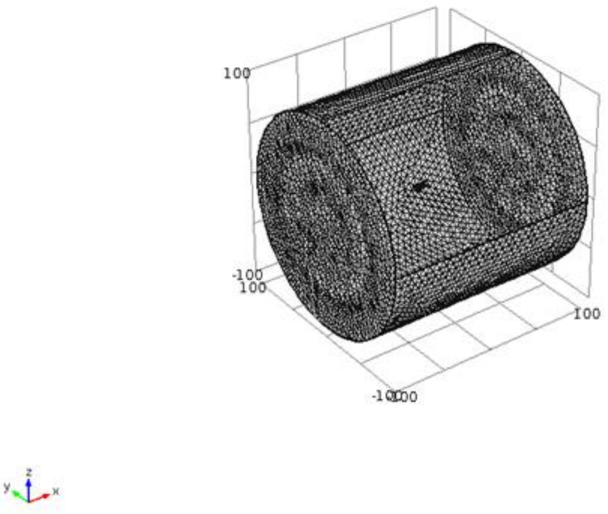

Figure 4.26: Generated mesh of the plate coil and the solution medium.

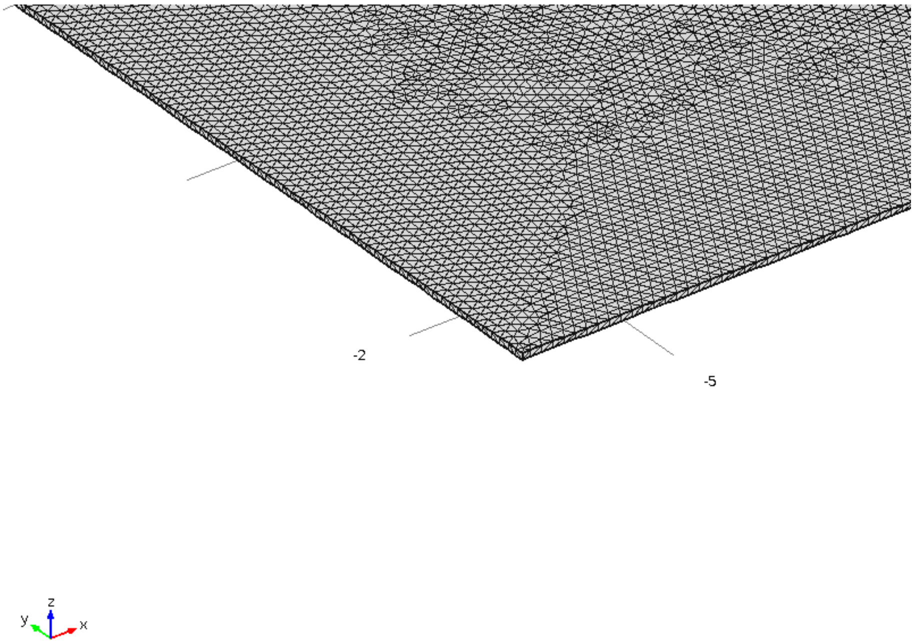

Figure 4.27: Generated mesh of the plate.

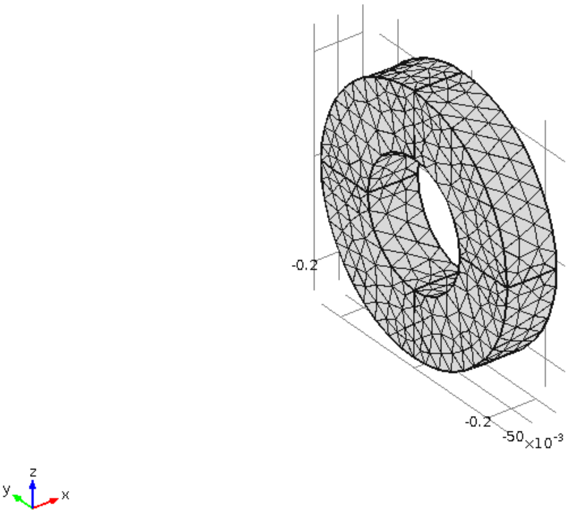

Figure 4.28: Generated mesh of the coil.

We take an observation point with respect to the coil. The observation point is 5m away from the center of the coil in positive x direction. This point is illustrated on the Figure 4.29.

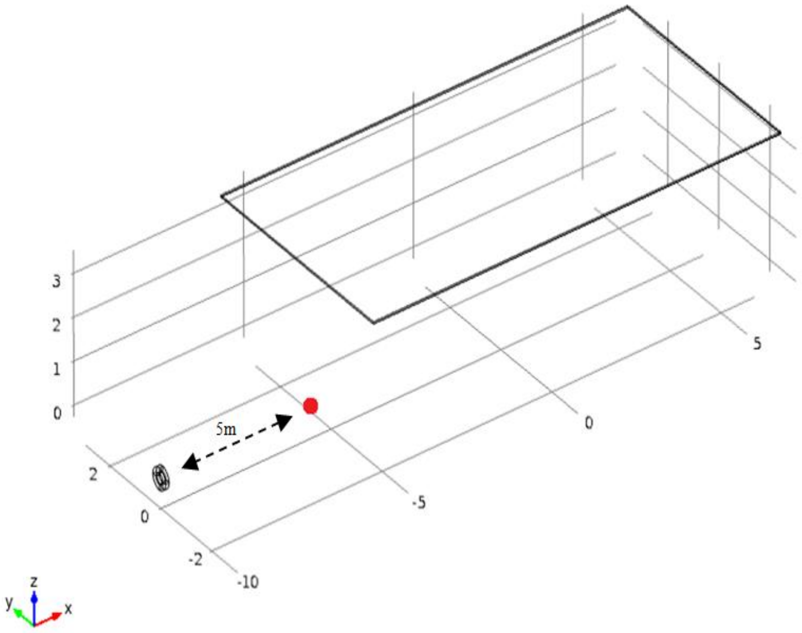

Figure 4.29: Plate, coil and observation point.

As the last step, we add frequency domain as study step and solver sequence for the model so as to compute the solution.

We observe the magnetic flux density of the coil through a 10cm observation line which is centered at the observation point (x=5m, y=0, z=0). When this observation line is x-directed (x=[4.95:5.05], y=0, z=0), y-directed (x=0, y=[-0.05:0.05], z=0) and z-directed (x=0, y=0, z=[-0.05:0.05]), we plot x, y and z components of the magnetic flux density of the coil through this line. We see that the curve of x component of the field is same when the line is y and z-directed. The slope of the y component of the field through y-directed line equals to the slope of the z component of the field through z-directed line. We repeat these calculations by changing the positions of the coil and the observation point in the solution domain and have the same magnetic flux density curves on the mentioned observation lines. These observations let us validate that the coil is excited in true directions and solutions are not affected by the position of the coil and the observation point as well as mesh of the plate. The solution medium is big enough.

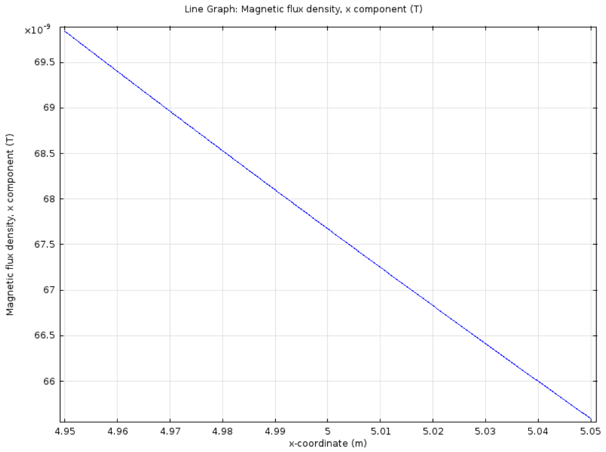

Figure 4.30: X component on the observation line (x=[4.95:5.05],y=0,z=0).

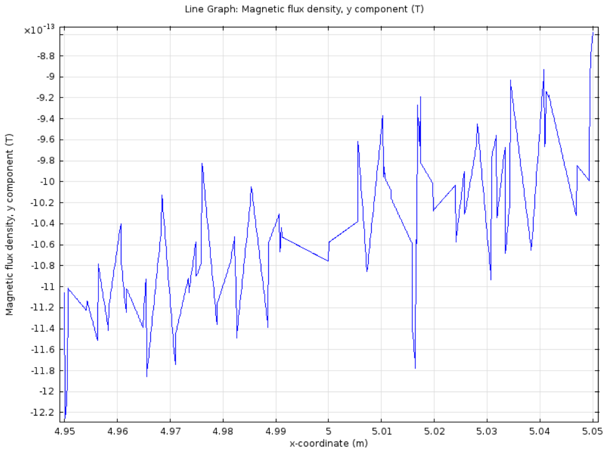

Figure 4.31: Y component on the observation line (x=[4.95:5.05],y=0,z=0).

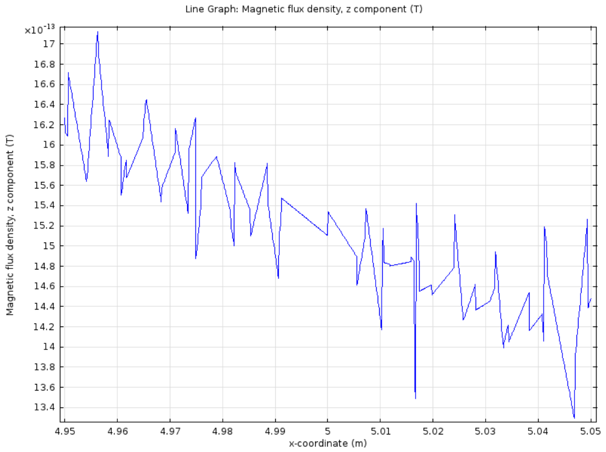

Figure 4.32: Z component on the observation line (x=[4.95:5.05],y=0,z=0).

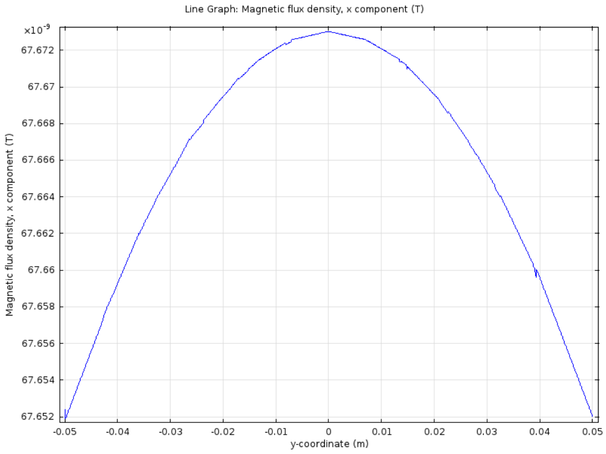

Figure 4.33: X component on the observation line (x=0,y=[-0.05:0.05],z=0).

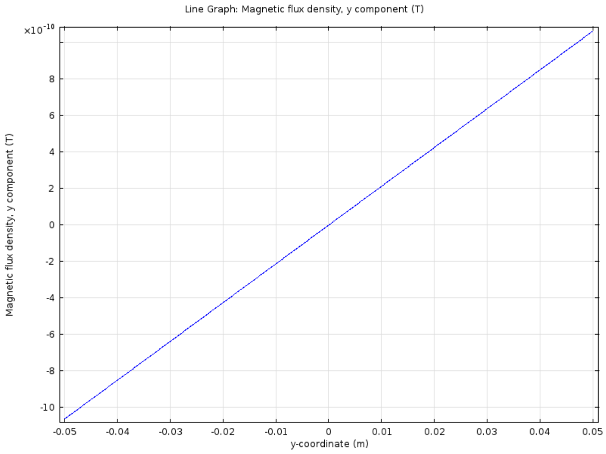

Figure 4.34: Y component on the observation line (x=0,y=[-0.05:0.05],z=0).

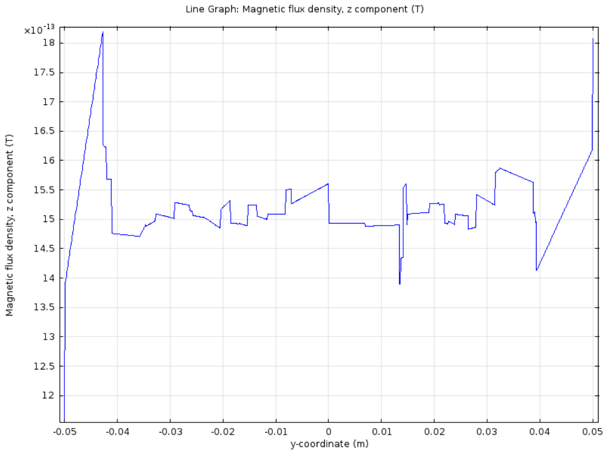

Figure 4.35: Z component on the observation line (x=0,y=[-0.05:0.05],z=0).

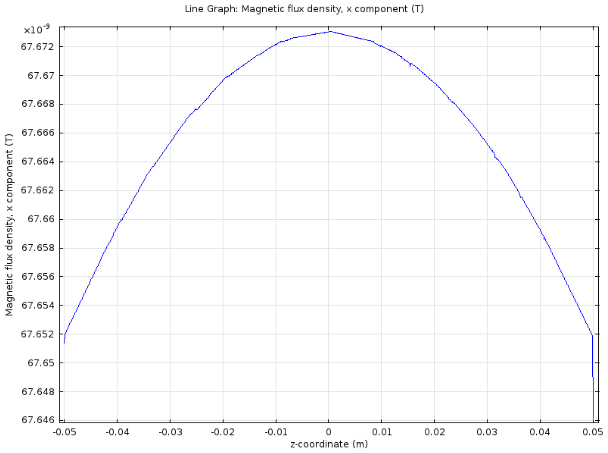

Figure 4.36: X component on the observation line (x=0,y=0,z=[-0.05:0.05]).

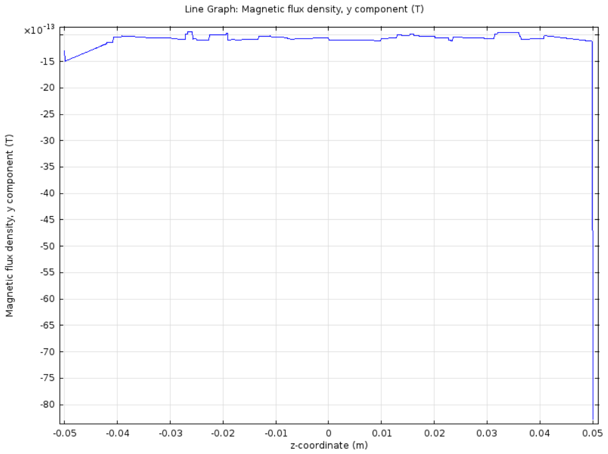

Figure 4.37: Y component on the observation line (x=0,y=0,z=[-0.05:0.05]).

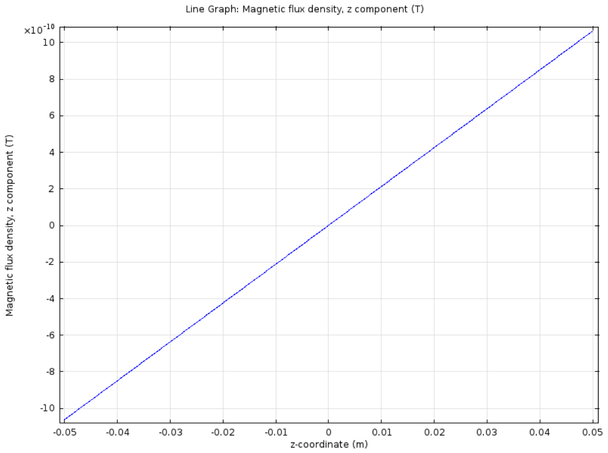

Figure 4.38: Z component on the observation line (x=0,y=0,z=[-0.05:0.05]).

Magnetic flux density of the coil at the observation point when the coil is anywhere in the solution domain and the plate domain has electrical properties of seawater is illustrated on the Table 4.6. We study the perturbation of these magnetic flux density values due to eddy currents created on the metal plate.

Magnetic Flux Density (T)		
x	**y**	**z**
6.76748e-8 -1.16503e-8i	-7.91263e-13 +4.28861e-14i	1.19563e-12 -8.4814e-14i

Table 4.6: Magnetic Flux Density of the coil on the observation point in seawater.

The real part of the x component of the magnetic flux density of the coil is 67nT, and imaginary part is -11.6nT. We expect the y and z components of it to be zero but there are numerical errors in the solution so they are not.

Now we start designating a detection region for the plate. Then, we study how much the magnetic field of the coil is perturbed due to the metal plate in this region. For a good detection performance we can restrict the amount of the attenuation loss of the secondary fields due to eddy currents as 8.7 dB (penetration depth) which is e^{-1} of magnetic flux density. Therefore, the target has to be at most $\frac{\lambda}{2}\times\frac{1}{e}=0.18\lambda$ away from the receiving sensors according to this restriction. Wavelength (λ) of the electromagnetic wave in seawater at 600 Hz is 64m so we have to set maximum detection distance as $0.18\lambda=0.18\times 64=11.5m$. With this assumption we take a detection region for the plate. This region is illustrated on the Figure 4.39. According to this region; we observe that if the transmitting coil is close to the plate with respect to z axis, measurable perturbation of the magnetic flux density of the coil starts when the observation point is near to the edges of the plate. However, if the coil is away from the plate with respect to z axis, measurable perturbation of the magnetic flux density of the coil starts when the coil comes to middle of the plate.

Described region is a rectangular pyramid. We designate that transmitting coil travels from minus x to plus x. We study 22m range of the coil from x=-15m to x=7m. We choose two paths for the coil to move; (x, y=0, z=0) and (x, y=0, z= -3.5). We solve the perturbation as the coil moves on these paths. These paths are 3.5m and 7m away from the plate respectively with respect to z axis. As the coil travels from x=-15m to x=7m, observation point travels from x=-10m to x=12m. After determining the detection region, we solve the problem for the iron and copper plate.

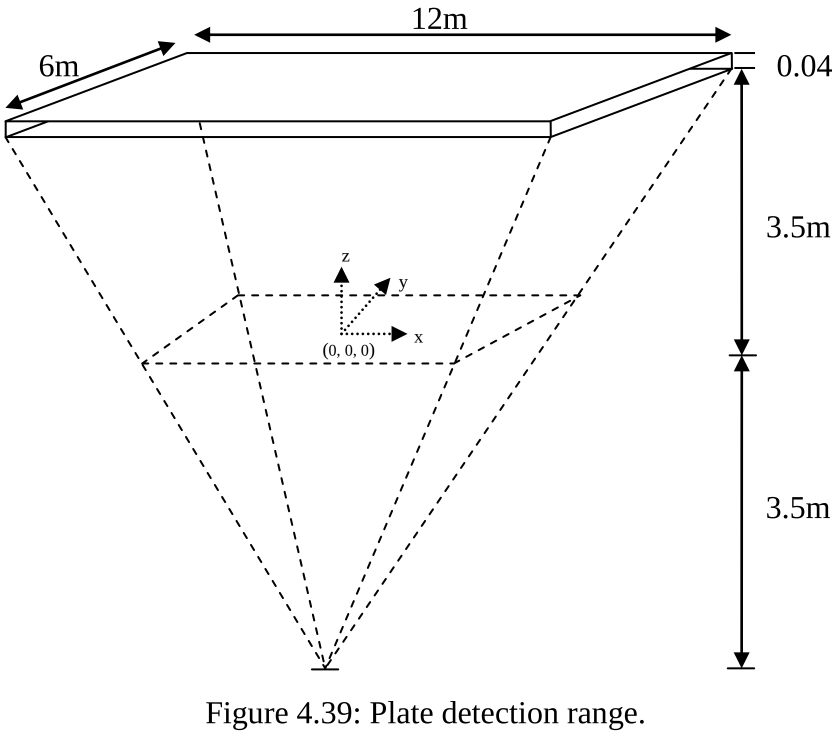

Figure 4.39: Plate detection range.

4.3.1 Iron Plate

Eddy currents are electric currents induced within conductors by a changing field in the conductor, [40]. If either the conductor moves through a steady field, or the magnetic field changes around a stationary conductor, eddy currents occur in the conductor. The circulating eddy currents have inductance and thus induce magnetic fields. Lenz's law governs this phenomenon. This law states that an induced electromotive force (emf) always gives rise to a current whose magnetic field opposes the original change in magnetic flux, [40]. Lenz's law is illustrated with the negative sign in Faraday's law of induction. Induced emf (ε) and the change in magnetic flux ($\partial\Phi_B$) have opposite signs, [41].

$$\varepsilon = -\frac{\partial\Phi_B}{\partial t} \tag{4.1}$$

In our analysis, the transmitting coil which is driven by alternating current (AC) passes under the metal plate. AC current of the coil creates changing magnetic field and this changing field creates eddy currents on the metal plate as governed by Lenz's law. These eddy currents oppose the original change in magnetic flux and perturb this field. Our aim is to detect this metal plate in a certain region by measuring the perturbation of the magnetic flux density of the coil.

We study perturbation of the magnetic flux density of the coil due to iron plate in this section. We put the coil to the origin (0, 0, 0). Electrical properties of iron are unit relative permittivity (ε_0), 4000 relative permeability (μ_r) and 1.12 x 10^7 (S/m) electrical conductivity (σ). Due to the fact that the relative permeability of the copper is 4000, magnetic field cannot completely penetrate into the interior of the plate. The formula of skin depth is $\delta = \frac{1}{\sqrt{\pi f \mu\sigma}}(m)$. Skin depth is about 0.1mm at 600 Hz for the iron plate. Therefore, we do not need to solve the interior domain of the iron plate in the physics. We can solve the fields only on the surfaces of the plate. Boundary condition of the six surfaces of the iron plate is impedance boundary condition. The equation solved on the surfaces of the plate is the following:

$$\sqrt{\frac{\mu_0 \mu_r}{\varepsilon_0 \varepsilon_r - j\dfrac{\sigma}{\omega}}}\, n \times H + E - (n.E)\,n = (n.E_s)\,n - E_s \,. \qquad (4.2)$$

After adding physics and boundary conditions, we generate a mesh for the model in order to discretize the geometry of the coil, plate and the solution medium into triangular and tetrahedral elements. In order to see the accuracy of the mesh of the iron plate firstly we set maximum element size of it as 32cm and solve the problem. Then we set maximum element size of it as 16cm and solve the problem. We take an observation line as (x=[-6:6], y=0, z=3.5) which is on the bottom surface of the plate and plot current density norm on this line for two mesh sizes. Thus we can compare the effect of the mesh size. As seen on the Figure 4.40, we get more accurate solution when the maximum element size is 16cm for the iron plate.

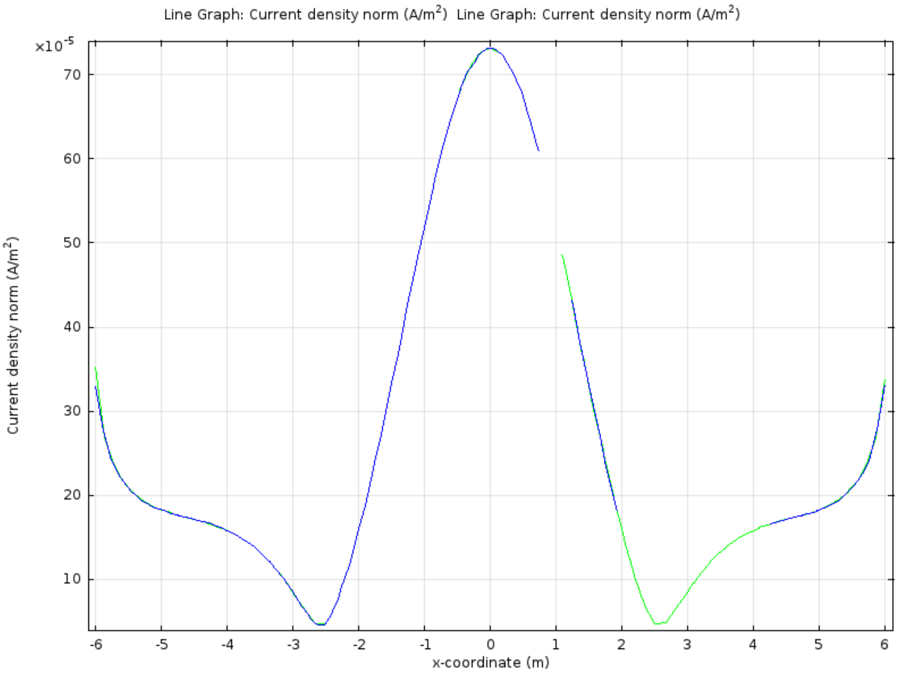

Figure 4.40: Element size 32cm (green) and 16cm (blue).

Now we plot the currents on the iron plate. We vary the phase angle of the eddy currents on the bottom surface of the iron plate from 0^0 to 360^0 to see how their magnitudes change while circulating on the surface of the plate. Figure 4.41 and Figure 4.42 are two plots of the eddy currents on the bottom surface of the plate for 0^0 and 75^0 phase angles respectively. The problem on these plots is that it is not possible to compare the magnitude of arrows of the surface current densities for varying phase angle. Plots compare the arrows with respect to the biggest magnitude arrow on its own angle instead of a globally referenced magnitude arrow for all varying angles.

We want to know how much real and imaginary part of the components of the magnetic flux density on the observation point changes as the coil moves under the iron plate. We solve the magnetic flux density of the coil when the observation point is at 23 locations; from x =-10m to x=12m when z=0 and z=-3.5m. The solutions of the fields are listed on the Table 4.7. When the maximum element size of the plate is 16cm, at each location of the coil, solution takes 6 minutes 49 seconds. There are 46 locations through the x axis on the two planes, so total solution time for the iron plate is about 5.2 hours.

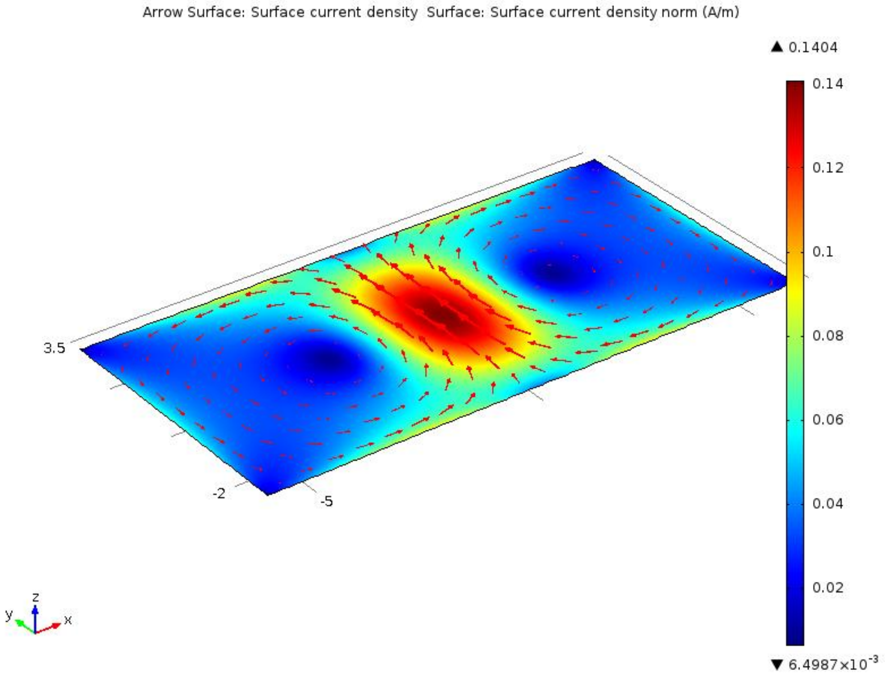

Figure 4.41: Eddy currents and surface current density on the bottom surface of the iron plate when phase angle: 0^0.

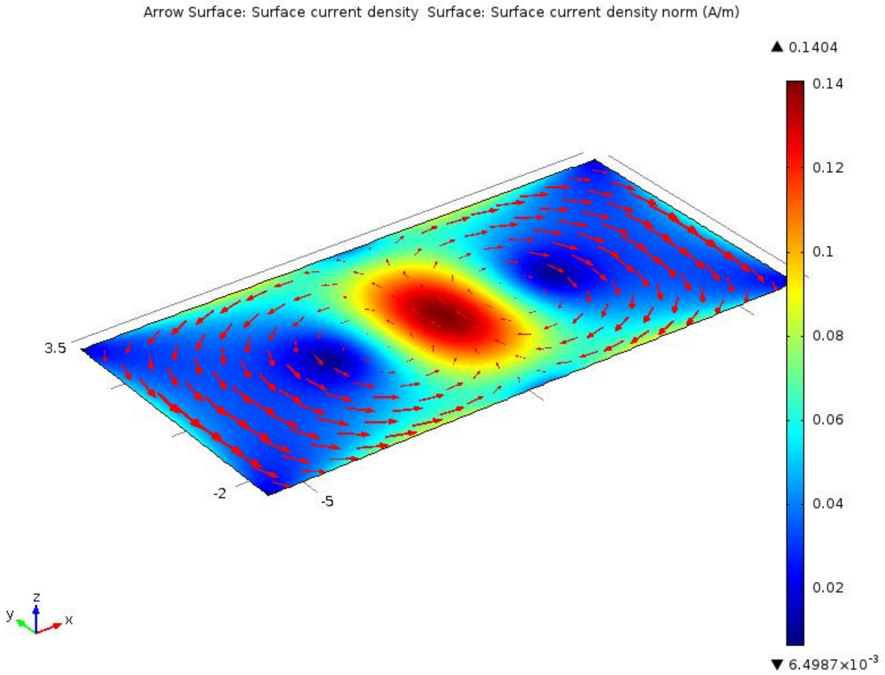

Figure 4.42: Eddy currents and surface current density on the bottom surface of the iron plate when phase angle: 75^0.

Iron plate	Magnetic Flux Density (T)					
Position of observation point (x)	**Path (x, y=0, z=0) (3.5m away from the plate)**			**Path (x, y=0, z=-3.5) (7m away from the plate)**		
	x	**y**	**z**	**x**	**y**	**z**
-10	6.76128e-8 -1.16581e-8i	1.62802e-12 -8.73932e-14i	4.50543e-11 +1.16284e-12i	6.76349e-8-1.16398e-8i	1.16938e-12-6.80395e-14i	1.88278e-11+4.79746e-12i
-9	6.75511e-8 -1.167e-8i	9.3294e-13 -9.481e-14i	6.34747e-11 +8.69048e-12i	6.76105e-8-1.16397e-8i	1.15034e-12-7.97215e-14i	1.53766e-11+1.30804e-11i
-8	6.7423e-8 -1.16944e-8i	-1.58989e-13 +5.18215e-14i	5.9582e-11 +2.16427e-11i	6.75831e-8-1.16427e-8i	-1.19956e-12+6.62933e-14i	6.36096e-12+2.56483e-11i
-7	6.71864e-8 -1.17397e-8i	-6.69395e-13 -2.74946e-14i	-5.04964e-11 +4.21391e-11i	6.75489e-8 -1.16507e-8i	-2.40652e-13 +2.26679e-15i	-1.36744e-11 +4.31244e-11i
-6	6.68572e-8 -1.18151e-8i	-7.96855e-13 -1.9348e-15i	-4.29991e-10 +7.29598e-11i	6.75111e-8 -1.16661e-8i	9.65619e-14 -1.8796e-14i	-5.2335e-11 +6.47391e-11i
-5	6.66239e-8 -1.19346e-8i	-6.63058e-13 -1.71031e-14i	-1.25863e-9 +1.19106e-10i	6.7483e-8 -1.16907e-8i	1.92036e-13 +4.25972e-14i	-1.05958e-10 +8.77571e-11i
-4	6.67662e-8 -1.21165e-8i	1.35265e-12 +9.22473e-15i	-2.47446e-9 +1.73462e-10	6.74602e-8 -1.17237e-8i	2.26564e-16 +3.09046e-15i	-1.70635e-10 +1.0815e-10i
-3	6.73703e-8 -1.23643e-8i	1.09569e-12 -9.23484e-14i	-3.76469e-9 +2.06179e-10i	6.74529e-8 -1.17618e-8i	-1.14932e-14 +2.12841e-14i	-2.32454e-10 +1.21529e-10i
-2	6.81947e-8 -1.26405e-8i	-1.08316e-12 +5.14974e-14i	-4.75523e-9 +1.80566e-10i	6.74561e-8 -1.18002e-8i	2.35016e-13 -1.9e-14i	-2.84517e-10 +1.24751e-10i
-1	6.88041e-8 -1.28685e-8i	-6.9344e-13 +8.77918e-14i	-5.25071e-9 +8.52892e-11i	6.74564e-8 -1.1833e-8i	-1.19429e-12 +6.43292e-15i	-3.1581e-10 +1.16982e-10i
0	6.89569e-8 -1.29842e-8i	4.85641e-13 -2.73673e-14i	-5.35762e-9 -4.80127e-11i	6.74556e-8 -1.18569e-8i	9.182e-13 +1.83699e-14i	-3.33433e-10 +1.00172e-10i
1	6.8823e-8 -1.30007e-8i	1.24376e-12 -3.90678e-15i	-5.3209e-9 -1.73983e-10i	6.74581e-8 -1.18717e-8i	1.06235e-13 +2.31642e-14i	-3.36755e-10 +7.67143e-11i
2	6.8687e-8 -1.29849e-8i	-7.18857e-13 -9.53529e-14i	-5.24905e-9 -2.81972e-10i	6.74519e-8 -1.18782e-8i	-1.10275e-12 +3.60455e-14i	-3.29146e-10 +4.88827e-11i
3	6.86875e-8 -1.29848e-8i	-8.61177e-14 -1.33719e-13i	-5.09603e-9 -4.00311e-10i	6.74527e-8 -1.18782e-8i	3.77186e-13 -5.46926e-14i	-3.14192e-10 +1.74793e-11i
4	6.88239e-8 -1.30006e-8i	4.51721e-13 -5.05925e-14i	-4.7236e-9 -5.7282e-10i	6.74554e-8 -1.18716e-8i	5.68954e-13 -7.52903e-14i	-2.87537e-10 -1.70575e-11i
5	6.89573e-8 -1.29838e-8i	1.15401e-13 +1.54007e-14i	-3.9822e-9 -8.23627e-10i	6.7459e-8 -1.1857e-8i	-3.0367e-13 -2.99855e-14i	-2.50521e-10 -5.28344e-11i
6	6.88012e-8 -1.28683e-8i	-7.78538e-13 +6.62836e-14i	-2.87833e-9 -1.11175e-9i	6.74575e-8 -1.18331e-8i	3.38665e-13 +3.91175e-14i	-2.08279e-10 -8.57351e-11i
7	6.81959e-8 -1.26407e-8i	-2.26217e-13 -3.90064e-14i	-1.76547e-9 -1.33236e-9i	6.74543e-8 -1.18002e-8i	-1.38764e-12 -3.4301e-14i	-1.68226e-10 -1.10093e-10i
8	6.73698e-8 -1.23647e-8i	1.91772e-13 +6.45656e-14i	-1.04197e-9 -1.39636e-9i	6.74547e-8 -1.1762e-8i	-4.46014e-13 +3.37821e-14i	-1.38012e-10 -1.20801e-10i
9	6.67626e-8 -1.2117e-8i	-4.17305e-13 +4.51303e-14i	-7.77081e-10 -1.27732e-9i	6.74604e-8 -1.17237e-8i	5.14914e-14 -2.72915e-14i	-1.2078e-10 -1.16173e-10i
10	6.66201e-8	-3.12154e-13	-7.40084e-10	6.74814e-8	-6.21796e-14	-1.08904e-10

	-1.1935e-8i	-7.50175e-14i	-1.00155e-9i	-1.16908e-8i	-5.31157e-14i	-9.8736e-11i
11	6.68581e-8 -1.18157e-8i	1.42032e-15 +9.88739e-15i	-6.74526e-10 -6.54064e-10i	6.75142e-8 -1.16663e-8i	8.34759e-13 -7.32367e-14i	-9.90892e-11 -7.41598e-11i
12	6.71872e-8 -1.17399e-8i	-7.22042e-13 +4.8835e-14i	-5.13444e-10 -3.53526e-10i	6.75483e-8 -1.16506e-8i	1.09916e-12 -1.059e-13i	-8.97047e-11 -4.87285e-11i

Table 4.7: Perturbation of the field on the observation point due to iron plate.

We plot these perturbed components of the magnetic flux density on the observation point due to the iron plate to be able to observe the change in norm, phase angle, real and imaginary parts of them.

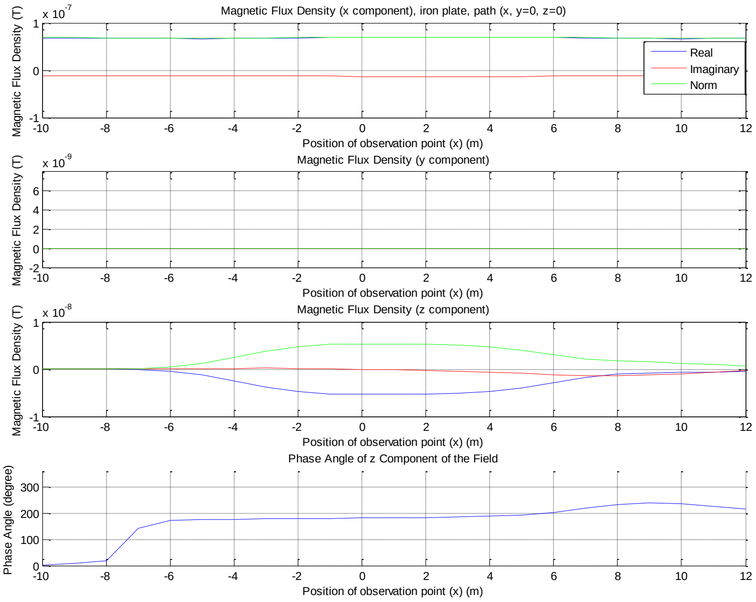

Figure 4.43: Perturbation of the field on the observation point due to iron plate through the path (x, y=0, z=0).

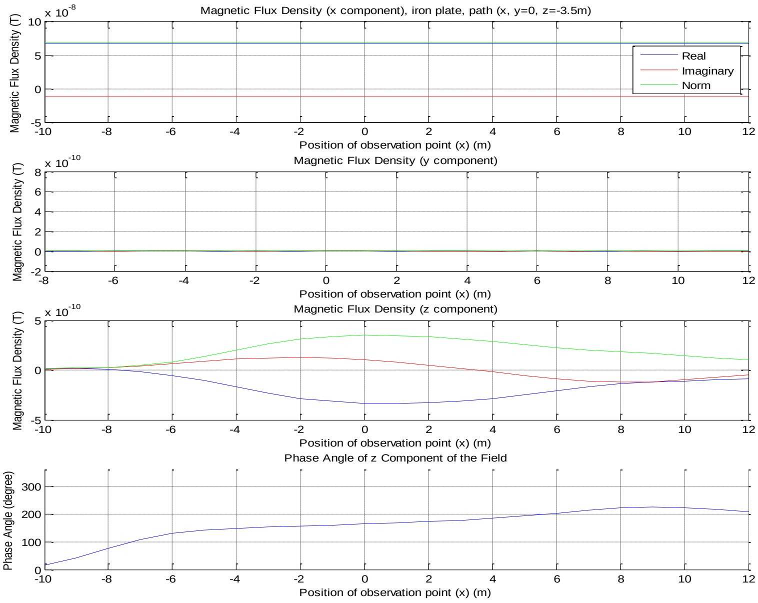

Figure 4.44: Perturbation of the field on the observation point due to iron plate through the path(x, y=0, z=-3.5).

Our first observation about the preceding two plots is that change in the z component of the magnetic flux density on the observation point is measurable via a fluxgate magnetometer. The strength of the field is levels of nanotesla. As the coil goes away from the iron plate with respect to z axis (from z=0 to z=-3.5m), norm of the z component of the field decreases due to the conductivity (4 S/m) of seawater. When the observation point travels on the z=0 plane which is 3.5m away from the plate with respect to z axis, real part of the z component on the observation point changes greater than the imaginary part of the z component of the field. However, when the observation point travels on the z=-3.5m plane which is 7m away from the plate with respect to z axis, imaginary part of the z component on the observation point changes comparable amount with respect to real part of the z component of the field. The edges of the plate are from x=-6m to x=6m. We can observe the perturbation of the field under the plate between these edges when we have a look at the norm of the z component of the field. As the coil starts leaving the plate, phase angle of the z component of the field increases. This effect can be seen around x=9m. There is symmetry around y=0 plane on the geometry so y component of the magnetic flux density on the observation point is zero.

4.3.2 Copper Plate

We solve the fields when the material of the metal plate is copper in this section. We put the coil to the origin (0, 0, 0) again. Electrical properties of copper are unit relative permittivity (ε_0), unit relative permeability (μ_0) and 5.998 x 10^7 (S/m) electrical conductivity (σ). Due to the fact that the relative permeability of the copper is one, magnetic field can penetrate into the interior of the plate. Skin depth is 2.663mm at 600 Hz for copper plate. Therefore, we also need to solve the interior domain of the copper plate. Ampere's Law is assigned to the domain of the copper plate and material properties of the copper are assigned to this domain.

After adding physics and boundary conditions for the copper plate like iron plate case, we generate a mesh for the model in order to discretize the geometry of the coil, plate and the solution medium into triangular and tetrahedral elements. We re-generate the mesh of the plate.

In order to see the accuracy of the mesh of the copper plate firstly we set maximum element size of it as 10cm and solve the problem. Then we set maximum element size of it as 8cm and solve the problem. We take an observation line as (x=[-6:6], y=0, z=3.5) which is on the bottom surface of the plate and plot current density norm on this line for two mesh sizes. Thus we can compare the effect of the mesh size. Comparison can be seen on the Figure 4.45. For these two mesh sizes, solution does not change distinguishably. Increasing mesh size gets calculations to last much longer time and causes to get warning of "out of memory".

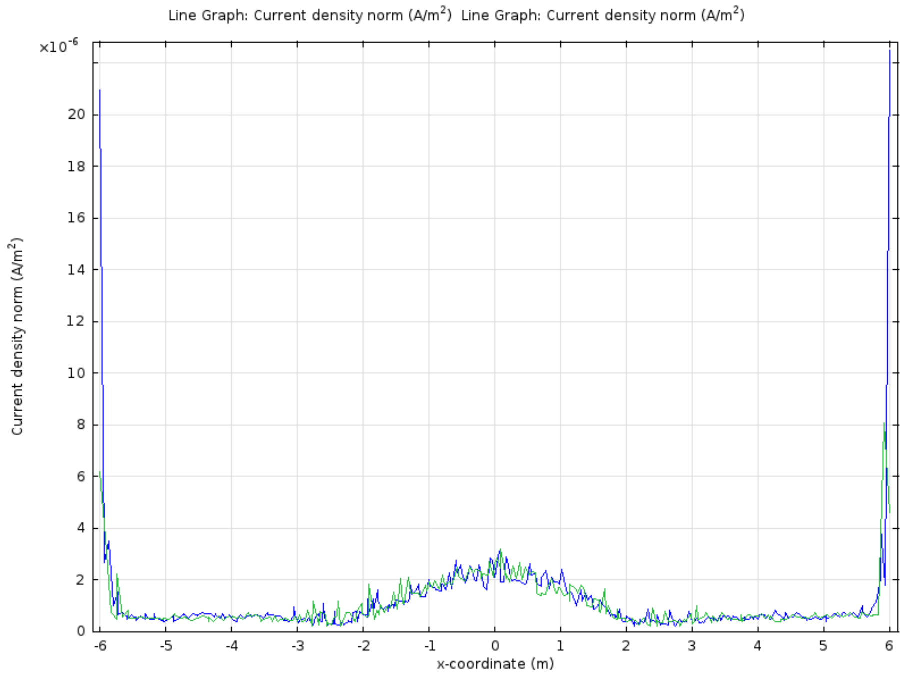

Figure 4.45: Element size 10cm (green) and 8cm (blue).

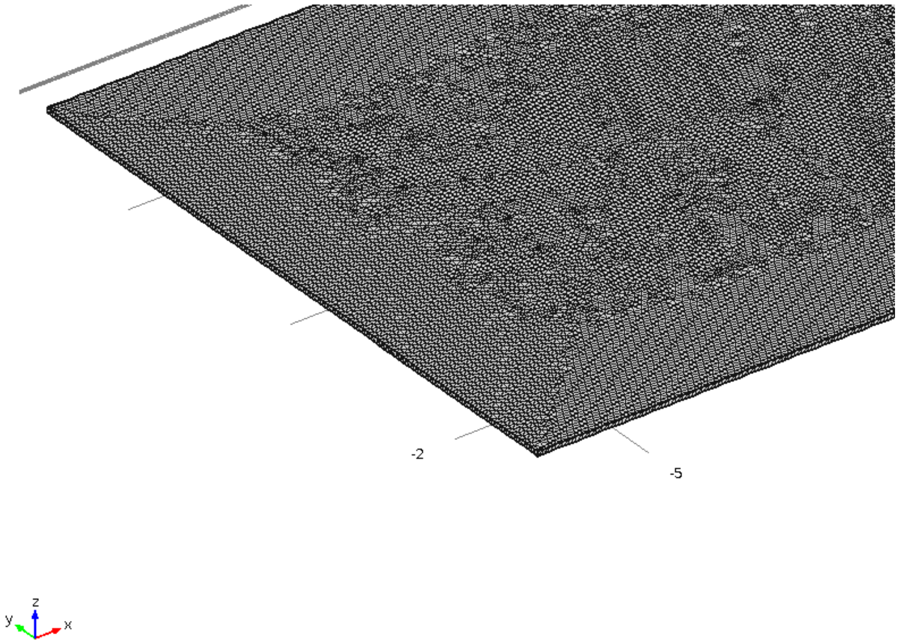

Figure 4.46: Generated mesh of the copper plate.

As done for the iron plate, we plot the currents on the copper plate. We vary the phase angle of the eddy currents on the bottom surface of the copper plate from 0^0 to 360^0 to see how their strength changes. Figure 4.47 and Figure 4.48 are two plots of the eddy currents on the bottom surface of the plate for 0^0 and 75^0 respectively. The same problem is valid also in this situation; we cannot compare the magnitude of arrows of the surface current densities.

We want to know how much real and imaginary part of the components of the magnetic flux density on the observation point changes as the coil moves under the copper plate. We solve the magnetic flux density of the coil when the observation point is at 23 locations; from x =-10m to x=12m when z=0 and z=-3.5m. The solutions of the fields are listed on the Table 4.8. When the maximum element size of the plate is 10cm, at each location of the coil, solution takes 10 minutes 45 seconds. There are 46 locations through the x axis on the two planes, so total solution time for the copper plate is about 8.2 hours.

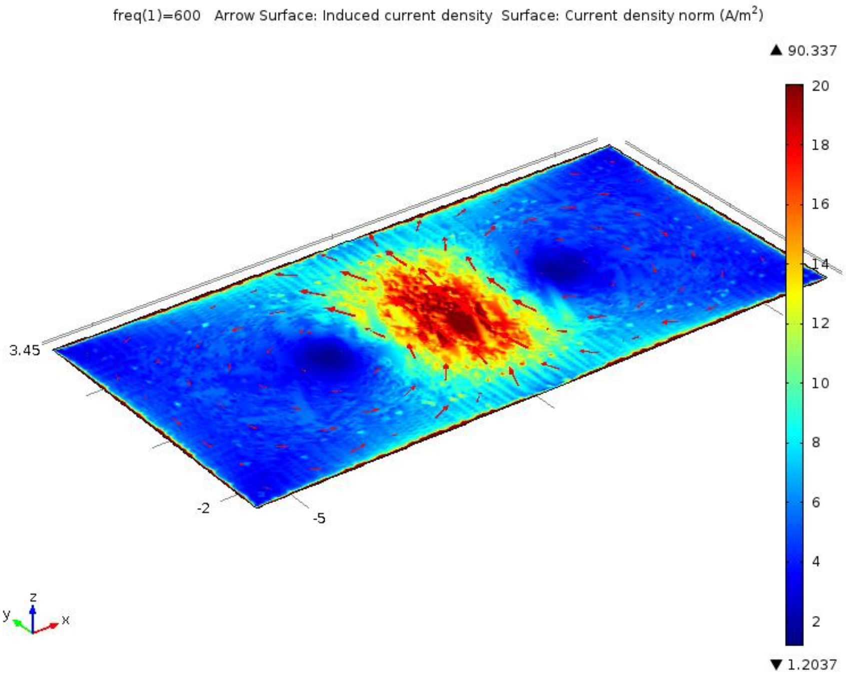

Figure 4.47: Eddy currents and surface current density on the bottom surface of the copper plate when phase angle of the current: 0^0.

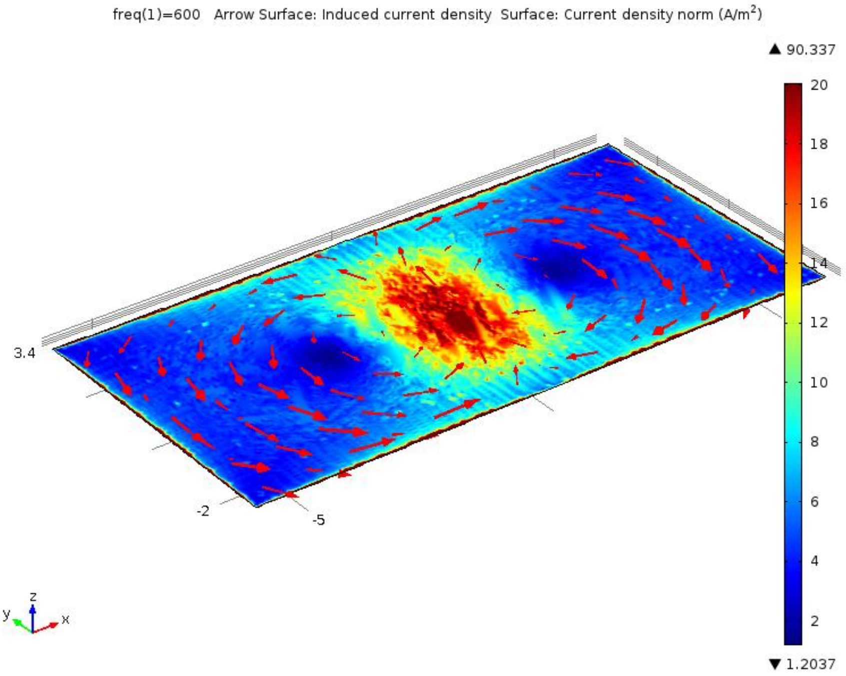

Figure 4.48: Eddy currents and surface current density on the bottom surface of the copper plate when phase angle of the current: 75^0.

Copper plate	Magnetic Flux Density (T)					
Position of observation point (x)	Plane (x, y=0, z=0) (3.5m away from the plate)			Plane (x, y=0, z=-3.5) (7m away from the plate)		
	x	y	z	x	y	z
-10	6.76021e-8-1.16322e-8i	1.30773e-12-1.54356e-13i	5.05768e-11+1.67586e-11i	6.7632e-8-1.16325e-8i	1.16976e-12-6.84117e-14i	2.15357e-11+1.03137e-11i
-9	6.75241e-8-1.16254e-8i	-1.74032e-12+3.17197e-14i	6.06198e-11+2.5876e-11i	6.7605e-8-1.16296e-8i	1.15108e-12-8.03045e-14i	1.73838e-11+2.33168e-11i
-8	6.73668e-8-1.16232e-8i	7.06063e-13-6.13521e-15i	3.09168e-11+1.0678e-10i	6.75741e-8-1.16298e-8i	-1.1988e-12+6.64149e-14i	2.96942e-12+4.32058e-11i
-7	6.7089e-8-1.16445e-8i	-6.97547e-13-2.28288e-14i	-1.56106e-10+2.23712e-10i	6.7536e-8-1.16355e-8i	-2.37657e-13-2.99699e-16i	-1.90357e-11+7.10966e-11i
-6	6.67413e-8-1.17299e-8i	-8.0106e-13+3.19199e-16i	-7.03368e-10+4.14804e-10i	6.74946e-8-1.16499e-8i	9.56329e-14-1.69802e-14i	-6.571e-11+1.06189e-10i
-5	6.65784e-8-1.19292e-8i	-5.41132e-13-3.05555e-14i	-1.78131e-9+6.67404e-10i	6.74646e-8-1.16756e-8i	1.91119e-13+4.12696e-14i	-1.29818e-10+1.44838e-10i
-4	6.69003e-8-1.22617e-8i	1.3657e-12-4.58275e-15i	-3.26005e-9+9.35476e-10i	6.74418e-8-1.17116e-8i	-3.3988e-15+1.70945e-15i	-2.05782e-10+1.81334e-10i
-3	6.77381e-8-1.26966e-8i	1.04811e-12-1.15489e-13i	-4.76727e-9+1.16591e-9i	6.7436e-8-1.17539e-8i	-1.19112e-14+1.53791e-14i	-2.77599e-10+2.09276e-10i
-2	6.8758e-8-1.31458e-8i	-1.00877e-12+2.0502e-14i	-5.89834e-9+1.30721e-9i	6.74407e-8-1.17964e-8i	2.34914e-13-1.36654e-14i	-3.36913e-10+2.23831e-10i
-1	6.94473e-8-1.34761e-8i	-6.85724e-13+1.05407e-13i	-6.45406e-9+1.32504e-9i	6.74415e-8-1.18321e-8i	-1.19155e-12+8.91322e-15i	-3.72461e-10+2.23245e-10i
0	6.95763e-8-1.36076e-8i	6.15971e-13-1.225e-13i	-6.57161e-9+1.24183e-9i	6.74399e-8-1.18573e-8i	9.19415e-13+1.10932e-14i	-3.92126e-10+2.095e-10i
1	6.93941e-8-1.35995e-8i	1.17615e-12+2.78003e-14i	-6.53129e-9+1.12223e-9i	6.7441e-8-1.18722e-8i	1.08426e-13+1.57367e-14i	-3.96221e-10+1.85564e-10i
2	6.92309e-8-1.35639e-8i	-5.54567e-13-2.07555e-13i	-6.45461e-9+9.98635e-10i	6.74339e-8-1.18785e-8i	-1.10094e-12+3.13612e-14i	-3.88643e-10+1.54295e-10i
3	6.92314e-8-1.35638e-8i	-2.61935e-14-1.6946e-13i	-6.29269e-9+8.48589e-10i	6.74347e-8-1.18785e-8i	3.77231e-13-5.05491e-14i	-3.72763e-10+1.16697e-10i
4	6.93949e-8-1.35992e-8i	4.8391e-13-5.69511e-14i	-5.89426e-9+6.16906e-10i	6.74384e-8-1.18722e-8i	5.68152e-13-7.22284e-14i	-3.43748e-10+7.31648e-11i
5	6.95764e-8-1.36068e-8i	9.00792e-14+2.53748e-14i	-5.07758e-9+2.522e-10i	6.74433e-8-1.18574e-8i	-3.03961e-13-3.19678e-14i	-3.02384e-10+2.558e-11i
6	6.94438e-8-1.34754e-8i	-8.52326e-13+1.016e-13i	-3.80906e-9-2.23197e-10i	6.74425e-8-1.18322e-8i	3.37114e-13+4.00411e-14i	-2.5377e-10-2.14335e-11i
7	6.87591e-8-1.31459e-8i	-2.63213e-13-2.82149e-14i	-2.46356e-9-6.69722e-10i	6.74389e-8-1.17964e-8i	-1.38607e-12-3.79011e-14i	-2.06139e-10-6.09273e-11i
8	6.77378e-8-1.26972e-8i	1.77639e-13+6.08121e-14i	-1.52818e-9-9.39817e-10i	6.74377e-8-1.17541e-8i	-4.47295e-13+3.24354e-14i	-1.68547e-10-8.60077e-11i
9	6.68968e-8-1.22624e-8i	-4.50082e-13+4.8409e-14i	-1.1241e-9-9.87624e-10i	6.7442e-8-1.17116e-8i	5.14774e-14-2.54015e-14i	-1.45302e-10-9.33937e-11i

10	6.65744e-8 -1.19295e-8i	-3.13809e-13 -7.05752e-14i	-1.00269e-9 -8.43701e-10i	6.7463e-8 -1.16756e-8i	-6.28841e-14 -5.51783e-14i	-1.29057e-10 -8.47356e-11i
11	6.67417e-8 -1.17302e-8i	3.86733e-15 +7.44658e-15i	-8.6951e-10 -5.86377e-10i	6.74978e-8 -1.16501e-8i	8.34726e-13 -7.55301e-14i	-1.15998e-10 -6.57153e-11i
12	6.70895e-8 -1.16444e-8i	-7.24434e-13 +4.7568e-14i	-6.42716e-10 -3.30076e-10i	6.75353e-8 -1.16354e-8i	1.10011e-12 -1.04887e-13i	-1.03789e-10 -4.3319e-11i

Table 4.8: Perturbation of the field on the observation point due to copper plate.

We plot these perturbed components of the magnetic flux density on the observation point due to the copper plate to be able to observe the change in norm, phase angle, real and imaginary parts of them.

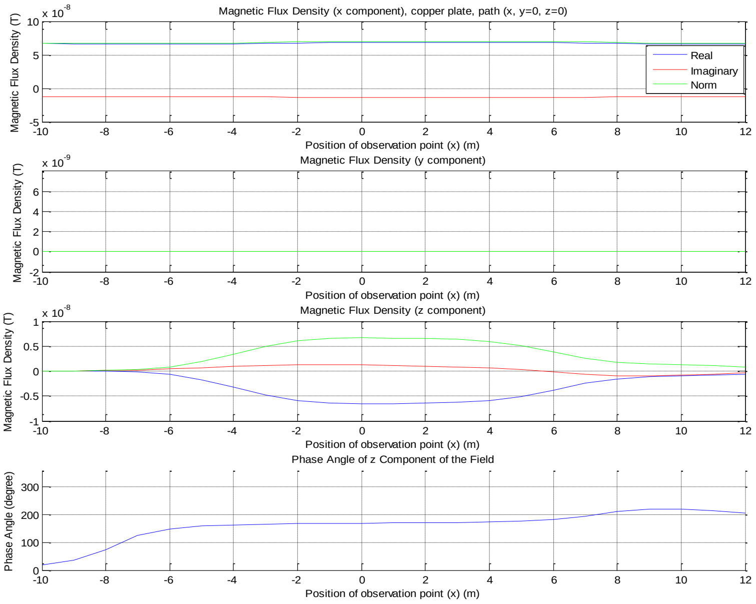

Figure 4.49: Perturbation of the field on the observation point due to copper plate, path(x, y=0, z=0).

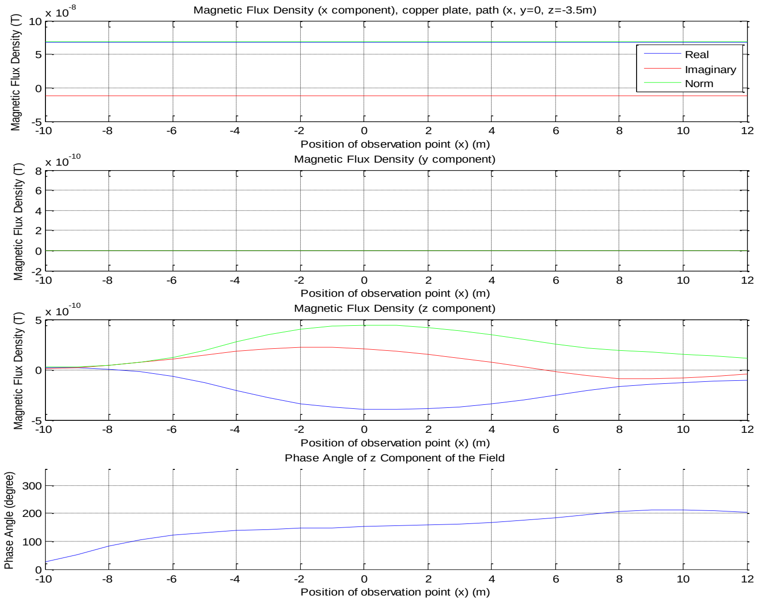

Figure 4.50: Perturbation of the field on the observation point due to copper plate, path(x, y=0, z=-3.5).

Our observation about the preceding two plots is that change in the z component of the magnetic flux density on the observation point is measurable via a fluxgate magnetometer. The strength of the field is levels of nanotesla. As the coil goes away from the copper plate with respect to z axis (from z=0 to z=-3.5m), norm of the z component of the field decreases due to the conductivity (4 S/m) of seawater as in the iron case. When the observation point travels on the z=0 plane which is 3.5m away from the plate with respect to z axis, real part of the z component of the magnetic flux density on the observation point changes greater than the imaginary part of the z component of the field. However, when the observation point travels on the z=-3.5m plane which is 7m away from the plate with respect to z axis, imaginary part of the z component of the magnetic flux density changes comparable amount with respect to real part of the z component of the field. The edges of the plate are from x=-6m to x=6m. We can observe the perturbation of the field under the plate between these edges when we have a look at the norm of the z component of the field. As the coil starts leaving the plate, phase angle of the z component of the field increases. This effect can be seen around x=9m. There is symmetry around y=0 plane on the geometry so y component of the magnetic flux density on the observation point is zero again.

We observe the perturbation of the magnetic flux density on the observation point due to iron and copper plates on the preceding plots. In the followings we compare and contrast the perturbation of the magnetic flux density due to iron and copper plates on the observation points on the same plots. Electrical properties of iron are unit relative permittivity (ε_0), 4000 relative permeability (μ_r) and 1.12 x 10^7 (S/m) electrical conductivity (σ). Electrical properties of copper are unit relative permittivity (ε_0), unit relative permeability (μ_0) and 5.998 x 10^7 (S/m) electrical conductivity (σ). We try to investigate the effect of electrical conductivity and relative permeability of the plate on the perturbation of the field on the observation point.

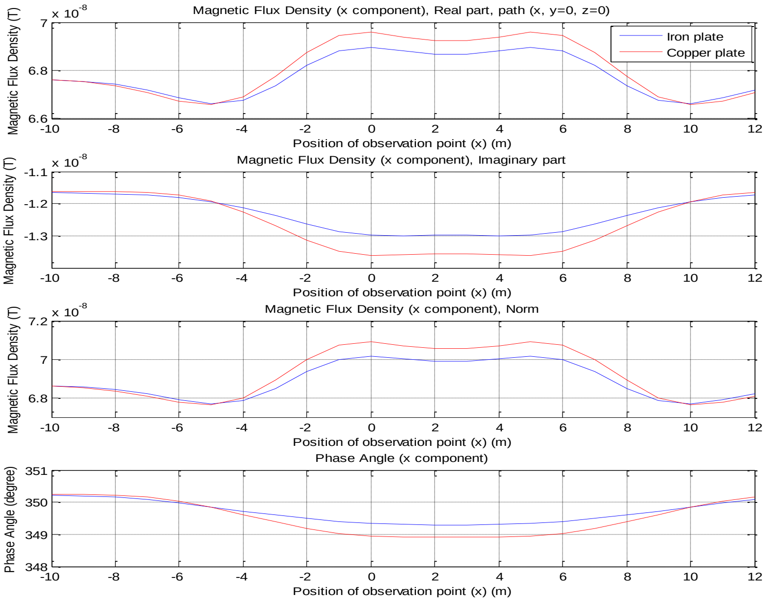

Figure 4.51: Perturbation of the field on the observation point (x component), iron vs. copper through the path(x, y=0, z=0).

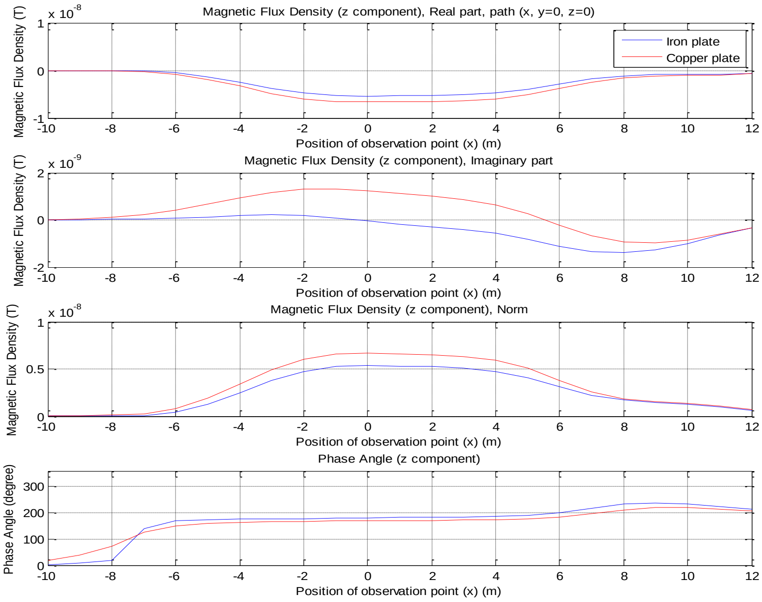

Figure 4.52: Perturbation of the field on the observation point (z component), iron vs. copper through the path(x, y=0, z=0).

We observe on the preceding two plots that as the observation point moves from the x=-10m to x=12m on z=0 plane, norm of x component of the field on the observation point increases due to the fact that x components of the secondary fields created by the eddy currents on the metal plate superpose onto the x component of the magnetic flux density of the coil. Norm of z component of the field increases more when plate is copper than when the plate is iron due to the fact that electrical conductivity of copper (5.998 x 10^7 (S/m)) is higher than electrical conductivity of iron (5.998 x 10^7 (S/m)). Difference on the phase angles of the z components of the iron and copper plates is 14.5^0 when the observation point is at x=5m and the coil is at the origin, at the middle of the plate.

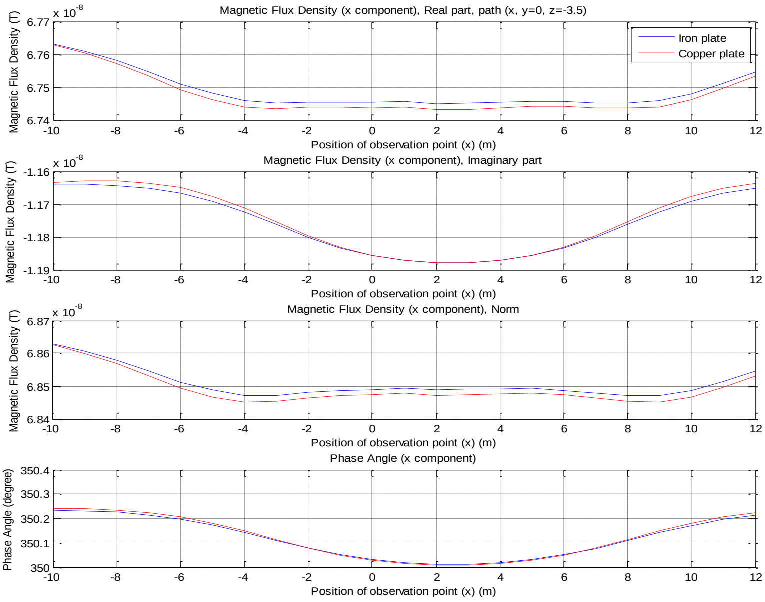

Figure 4.53: Perturbation of the field on the observation point (x component), iron vs. copper through the path(x, y=0, z=-3.5).

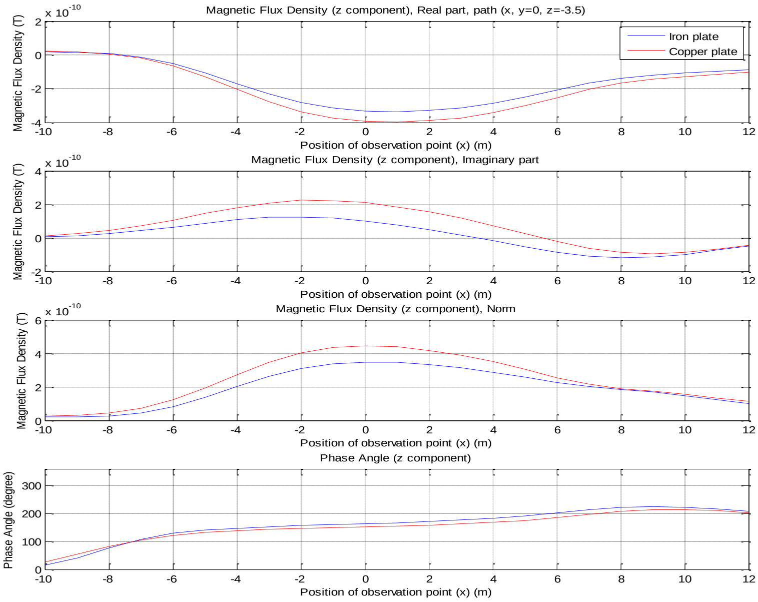

Figure 4.54: Perturbation of the field on the observation point (z component), iron vs. copper through the path(x, y=0, z=-3.5).

We observe on the preceding two plots that as the observation point moves from the x=-10m to x=12m on z=-3.5m plane, norm of x component of the field on the observation point decreases due to the fact that x components of the secondary fields created by the eddy currents on the metal plate superpose onto the x component of the magnetic flux density of the coil. Norm of z component of the field increases more when plate is copper than when the plate is iron due to the fact that electrical conductivity of copper (5.998 x 10^7 (S/m)) is higher than electrical conductivity of iron (5.998 x 10^7 (S/m)). Difference on the phase angles of the z components of the iron and copper plates is 16.7^0 when the observation point is at x=5m and the coil is at the origin, at the middle of the plate.

We cannot barely observe the effect of relative permeability on the perturbation of the magnetic flux density of the coil on the preceding solutions. Now we solve the fields on the observation point (5, 0, 0) for two electrical conductivity and relative permeability when the coil is at the origin. We solve this case like in the copper plate; we assign ampere's law to the plate, set relative permittivity (ε_r) as 1 and solve inside of it as well. The solutions are illustrated on the Table 4.9. We cannot observe the effect of relative permeability on the phase angle of the z component of the field. However, as the electrical conductivity changes, phase angle of the z component of the field changes as well.

	Magnetic Flux Density (T)			Phase angle of z (degree)
	x	y	z	
σ = 5.998e7 μ_r = 1	6.95745e-8-1.36122e-8i	1.09891e-12-1.08741e-14i	-5.09055e-9+2.55984e-10i	177.12124
σ = 5.998e7 μ_r = 4000	6.95746e-8-1.36122e-8i	1.09959e-12-1.19506e-14i	-5.09062e-9+2.55991e-10i	177.12121
σ = 1.12e7 μ_r = 4000	6.95752e-8-1.36047e-8i	1.14818e-12+3.37358e-14i	-5.09342e-9+2.41446e-10i	177.28601
σ = 1.12e7 μ_r = 1	6.9574e-8-1.36049e-8i	1.11725e-12+5.56952e-14i	-5.09154e-9+2.41747e-10i	177.28163

Table 4.9: Effect of relative permeability and electrical conductivity on the phase angle.

4.4 Magnetic Field Due to Current in Straight Wire

Submarines create perturbation on the ambient Earth magnetic field due to their ferromagnetic bodies. Magnetic anomaly detector equipped aircrafts fly over the oceans and seas so as to detect submerged submarines. Detection performances of MAD equipped aircrafts are tested in the development processes of these systems. However, it is not possible to have a submerged submarine any time tests are wanted to be done. So in order to test the performance of the MAD equipped aircrafts, DC current carrying wire systems which create same amount of perturbation on the ambient Earth magnetic field are developed.

In this section we designate a submarine model in a magnetic field and try to observe how much perturbation on the field created by the submarine. Then we designate a current carrying wire and try to observe how much magnetic field this wire can create. We compare the perturbation on ambient Earth magnetic field due to the submarine and magnetic field of the current carrying wire on observation lines.

Firstly we study the perturbation of ambient Earth magnetic field due to a submarine in COMSOL Multiphysics. As illustrated on the Figure 4.55, we take a submarine model. Dimensions of the submarine are 60m length, 6m diameter and 2.54cm thickness. We put this submarine into the solution medium. Solution medium is an x-directed square prism. Dimensions of the square prism are 80m by 80m by 200m. Solution medium and the submarine are on the Figure 4.56.

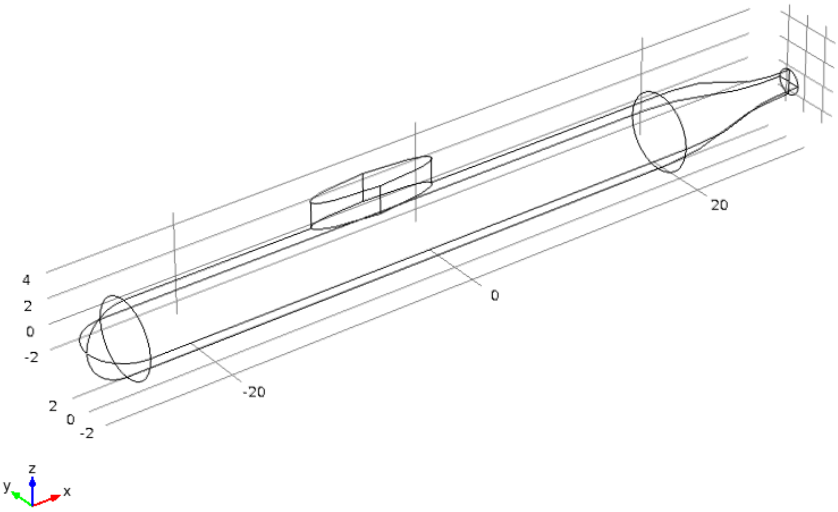

Figure 4.55: Model of submarine.

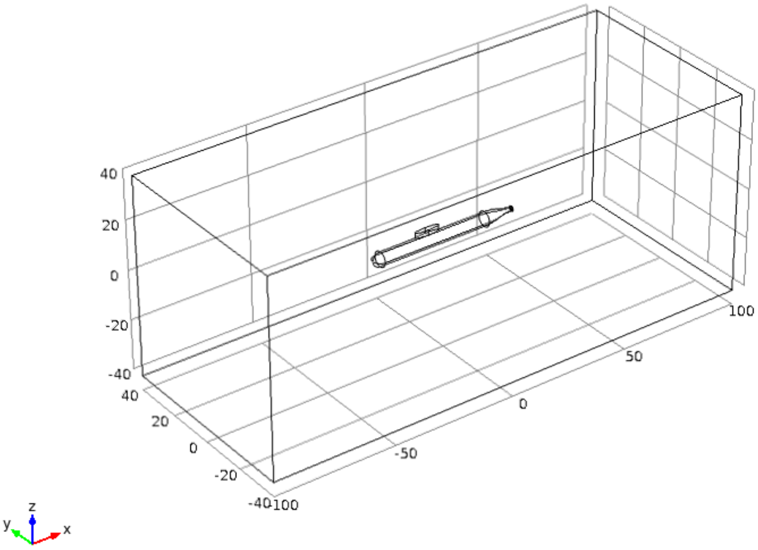

Figure 4.56: Submarine in the solution medium.

After modeling the geometry of the submarine, *Magnetic Fields, No Currents* interface is added under the *AC/DC* branch for the physics selection of the model. This interface solves the following equations:

$$\nabla.B = 0, \tag{4.3}$$

$$H = -\nabla v_m, \tag{4.4}$$

where B is the magnetic flux density vector, H is the magnetic field strength, v_m is the magnetic scalar potential.

After adding physics for the model, we assign boundary conditions to the submarine and outer boundary of the solution domain enclosing the submarine geometry. Boundary condition on the surfaces of the medium is magnetic insulation. The equation solved on these surfaces is $n.B = 0$. Boundary condition on the surfaces of the submarine is magnetic shielding. The equation solved on these surfaces is $n.\left(B_1 - B_2\right) = -\nabla_t.\left(\mu_0 \mu_r d_s \nabla_t V_m\right)$. Relative permeability of the material of the submarine is 700. Magnetic flux density applied onto the submarine is 50 x 10^{-6} (T).

After adding physics and boundary condition, we generate a mesh for the model in order to discretize the complex geometry of the coil into triangular elements. Generated meshes of the submarine and the solution domain can be seen on the Figure 4.57 and Figure 4.58.

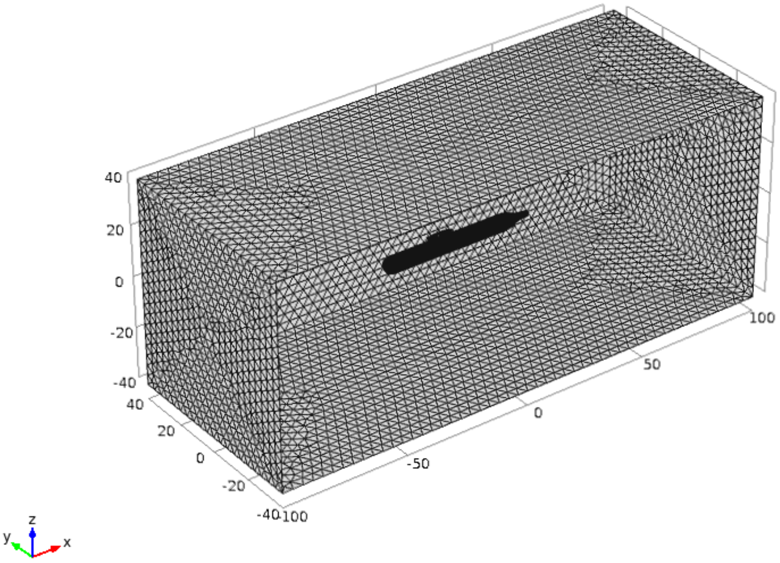

Figure 4.57: Generated meshes of the submarine and the solution medium.

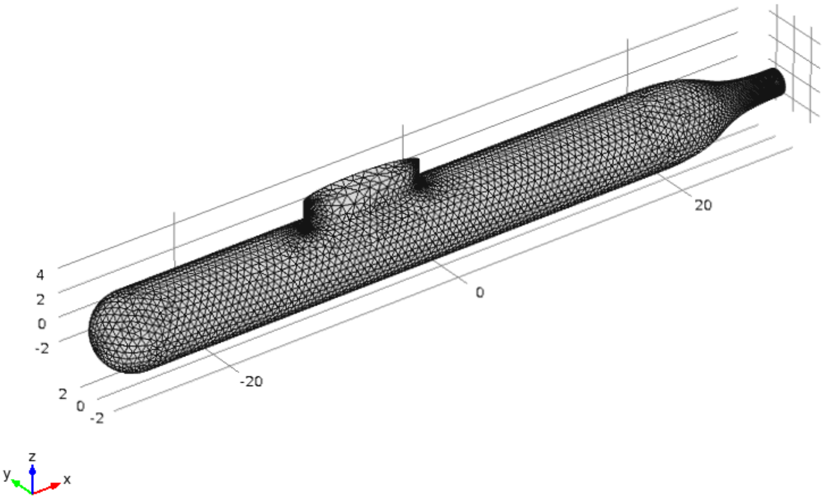

Figure 4.58: Generated mesh of the submarine.

As the last step, we add stationary domain as study step and solver sequence for the model so as to compute the solution.

We begin post-processing of the solution. We take observation lines on the medium and observe how the magnetic field around the submarine is perturbed. First observation line is (x=0, y=0, z=-40 to z=40). The observation line is illustrated on the Figure 4.59. Perturbation of the magnetic field through the line due to existence of the submarine can be seen on the Figure 4.60. Second observation line is (x=0, y=-25 to y=25, 13). The observation line is illustrated on the Figure 4.61. This line is 10m away from the surface of the submarine. Perturbation of the magnetic field through the line due to existence of the submarine can be seen on the Figure 4.62. Third observation line is (x=0, y=-25 to y=25, 18). This line is 15m away from the surface of the submarine. Perturbation of the magnetic field through the line due to existence of the submarine can be seen on the Figure 4.63. Forth observation line is (x=0, y=-25 to y=25, 28). This line is 25m away from the surface of the submarine. Perturbation of the magnetic field through the line due to existence of the submarine can be seen on the Figure 4.64.

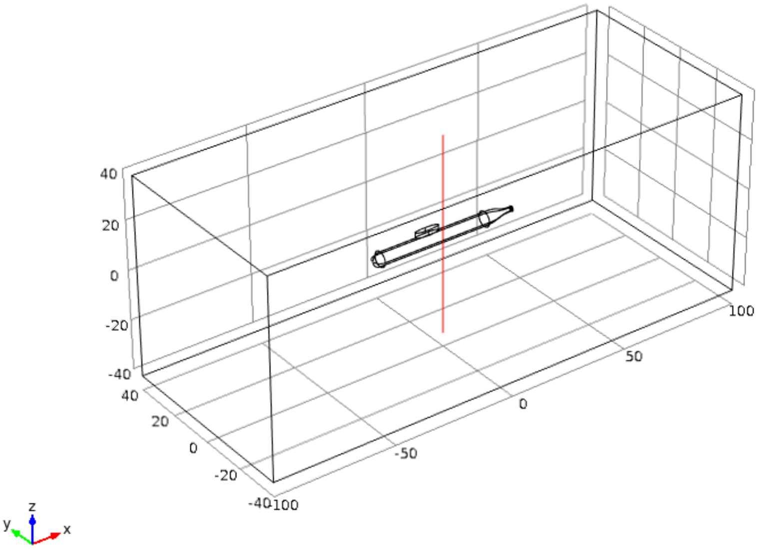

Figure 4.59: Observation line (x=0, y=0, z=-40 to z=40).

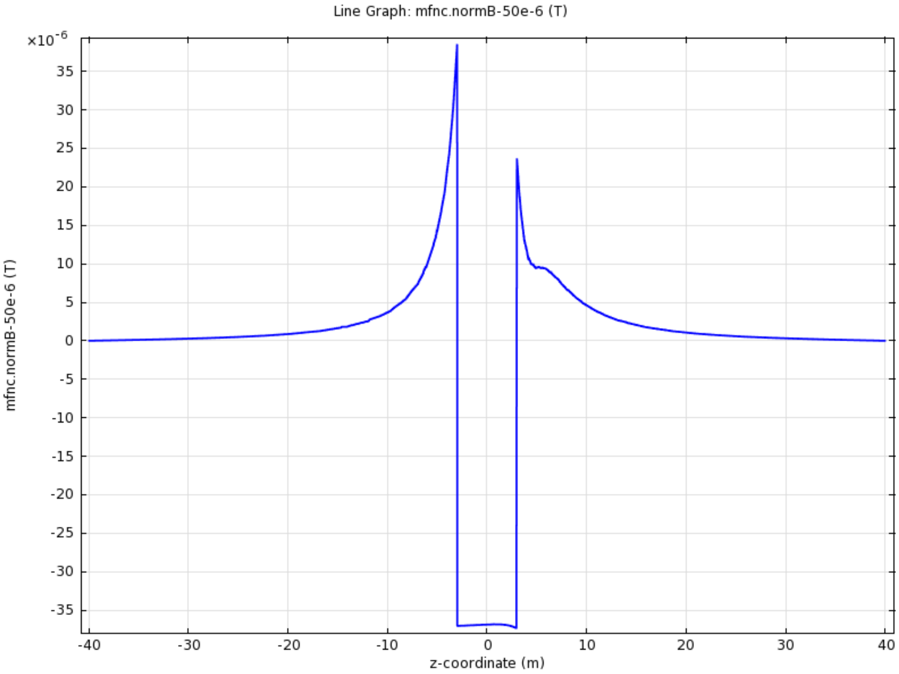

Figure 4.60: Perturbation on the line of (x=0, y=0, z=-40 to z=40).

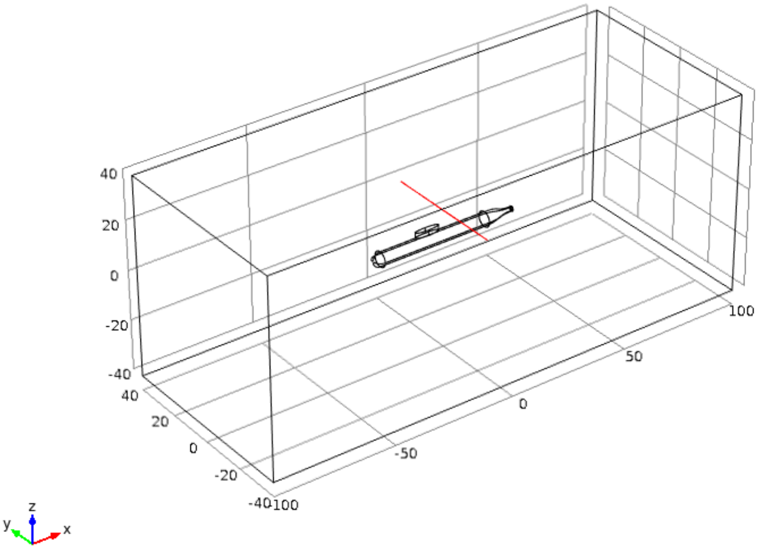

Figure 4.61: Observation line (x=0, y=-25 to y=25, z=13).

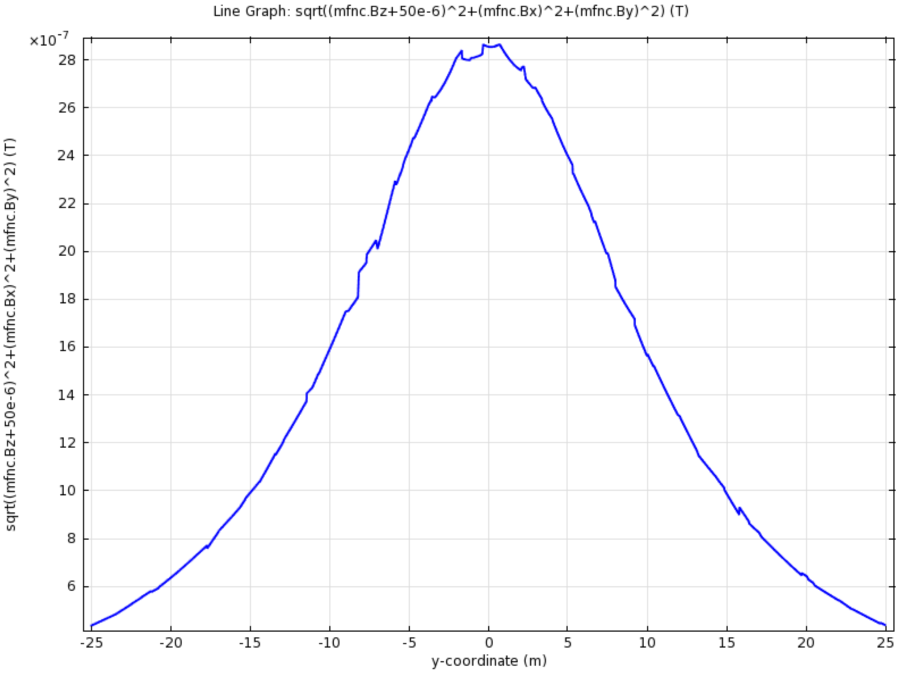

Figure 4.62: Perturbation on the line of (x=0, y=-25 to y=25, z=13). 10m above the submarine.

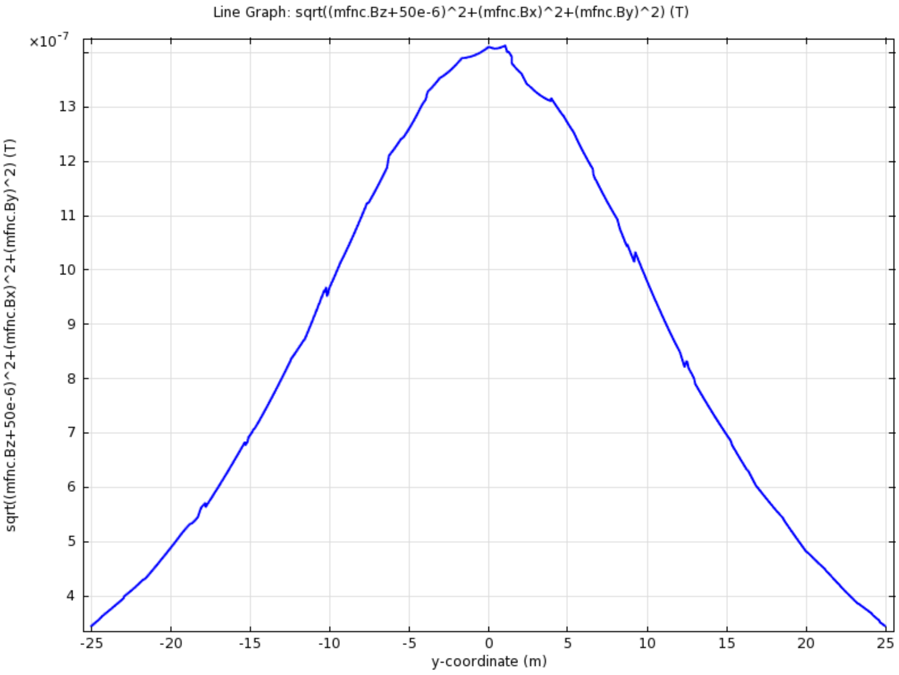

Figure 4.63: Perturbation on the line of (x=0, y=-25 to y=25, z=18). 15m above the submarine.

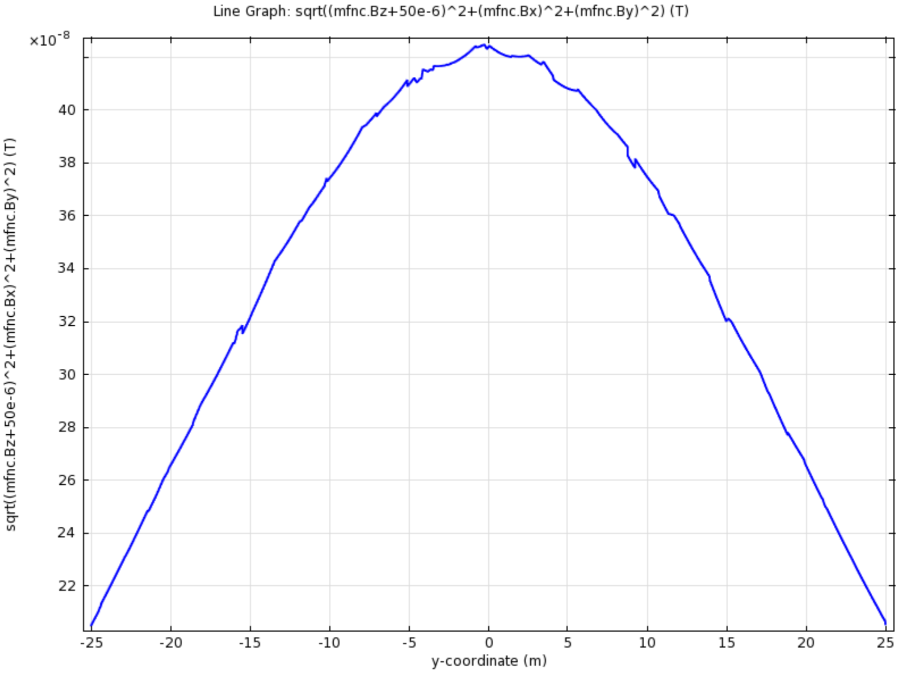

Figure 4.64: Perturbation on the line of (x=0, y=-25 to y=25, z=28). 25m above the submarine.

Observation line	**(x=0, y=0, z=-40m to 40m)**	**(x=0, y=-25m to 25m, z=13), 10 above surface of submarine**	**(x=0, y=-25m to 25m, z=18), 15 above surface of submarine**	**(x=0, y=-25m to 25m, z=28), 25 above surface of submarine**
Maximum perturbation (nT)	35000	2800	1400	420

Table 4.10: Perturbation of ambient Earth magnetic field due to submarine.

Secondly we study field of a current carrying wire towing system. Such current carrying wire systems are thrown by ships or submersed submarines. They are stand alone systems that tow the wire. The aim of these systems is to perturb ambient Earth magnetic field like a submarine in order to test the performance of magnetic anomaly detector equipped aircrafts.

We designate a system which tows 30m wire. The system can be seen on the Figure 4.65. Length of 29m portion of it is insulated from the seawater and last 1 meter portion is contacting with seawater. Thus, the applied current turns back to the tube (wire towing vehicle) 29m away from it on conducting seawater instead of just after leaving the tube.

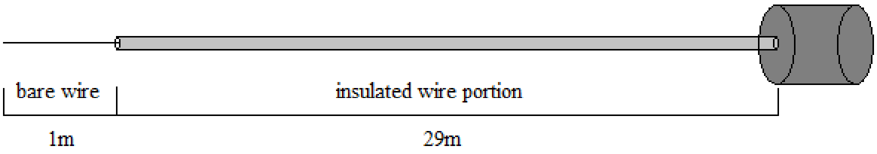

Figure 4.65: Current carrying wire system.

We take an x-directed cylinder as the simulation medium. The dimensions of the cylinder are 50m radius and 100 length. We take a 30m wire. The wire and the solution medium is shown on the Figure 4.66.

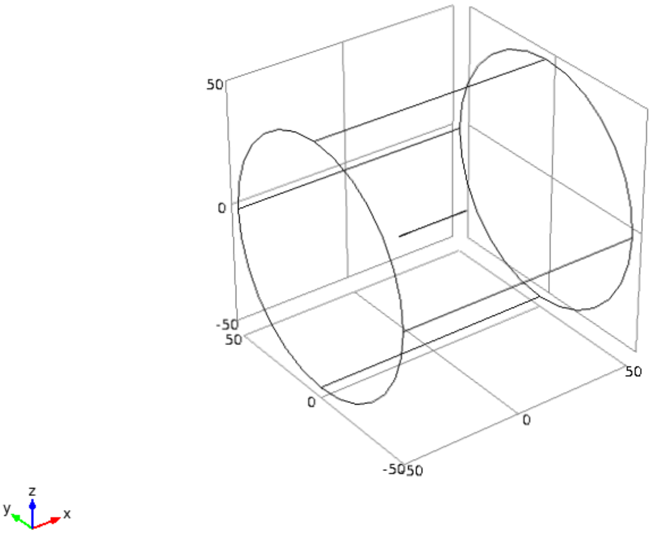

Figure 4.66: Wire and solution domain.

After modeling the geometry of the wire, *Magnetic Fields* interface is added under the *AC/DC* branch for the physics selection of the model. The equation solved in this interface is the equation (2.12).

After adding physics for the model, we need to assign boundary conditions to the outer boundary of the solution domain enclosing the wire geometry. Boundary conditon on the surfaces of the solution domain is magnetic insulation. The equation solved on these surfaces is $n \times A = 0$. Edge current of 8.25 Ampere is applied to the wire.

After adding physics and boundary conditions, we generate a mesh for the model in order to discretize the complex geometry into triangular and tetrahedral elements. In order to be able to mesh the wire well, we take a cylinder whose radius is 0.02m. The meshing of the solution domain and the wire are shown on the Figure 4.67.

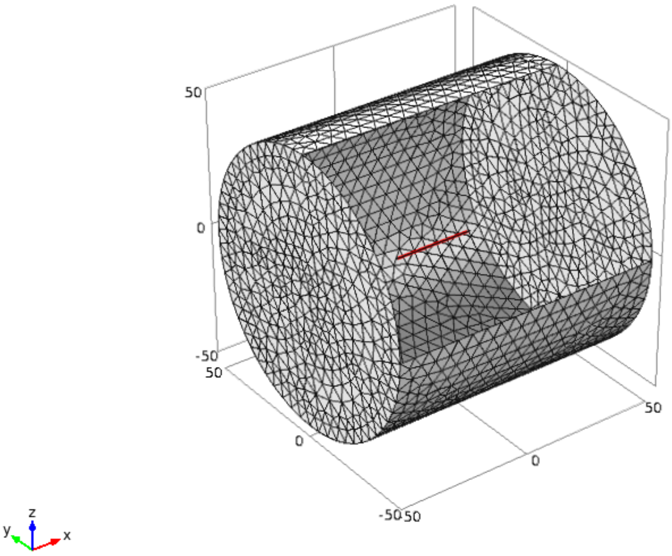

Figure 4.67: Generated meshes of the wire and the solution domain.

For the final step, we have to add study and solver sequence for the model in order to compute the solution. We add stationary domain as study step and solver sequence for the model so as to compute the solution.

We begin post-processing of the solution. We observe fields of the wire on different observation lines as in the submarine case. First observation line of the magnetic flux density norm is (x=0, y=0, z=-40 to z=40). This line can be seen on the Figure 4.68. Magnetic flux density norm along this observation line can be seen on the Figure 4.69. Second observation line of the magnetic flux density norm is (x=0, y=-25 to y=25, z=10). This line is illustrated on the Figure 4.70. Magnetic flux density norm along this observation line can be seen on the Figure 4.71. Third observation line of the magnetic flux density norm is (x=0, y=-25 to y=25, z=15). Magnetic flux density norm along this observation line can be seen on the Figure 4.72. Forth observation line of the magnetic flux density norm is (x=0, y=-25 to y=25, z=25). Magnetic flux density norm along this observation line can be seen on the Figure 4.73.

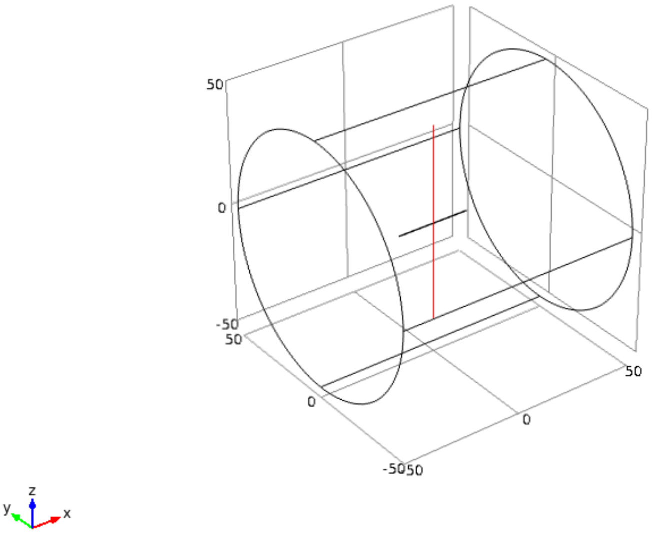

Figure 4.68: Observation line (x=0, y=0, z=-40 to z=40).

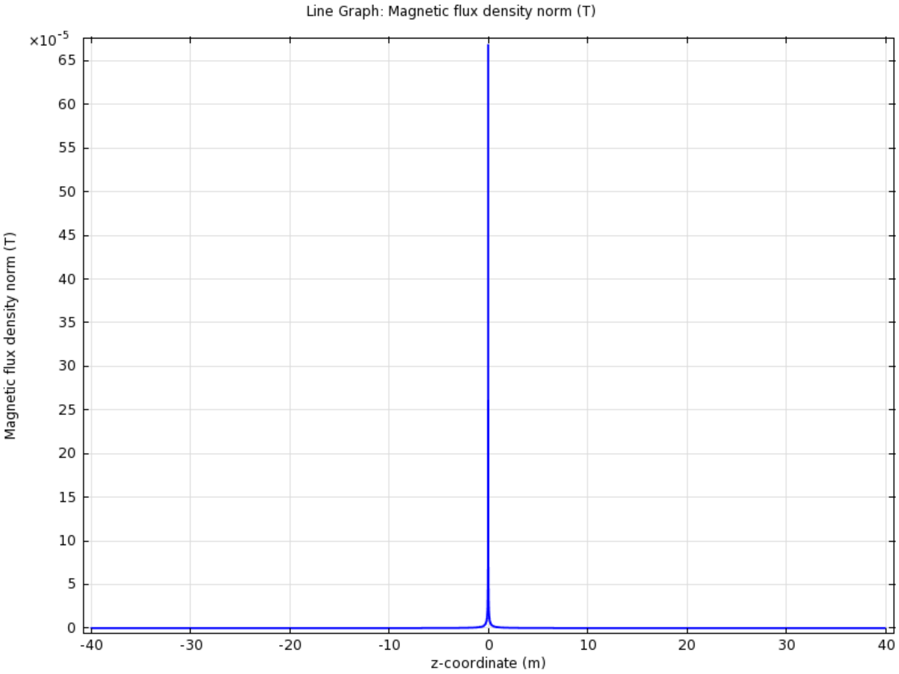

Figure 4.69: Magnetic Flux Density norm on the line of (x=0, y=0, z=-40 to z=40).

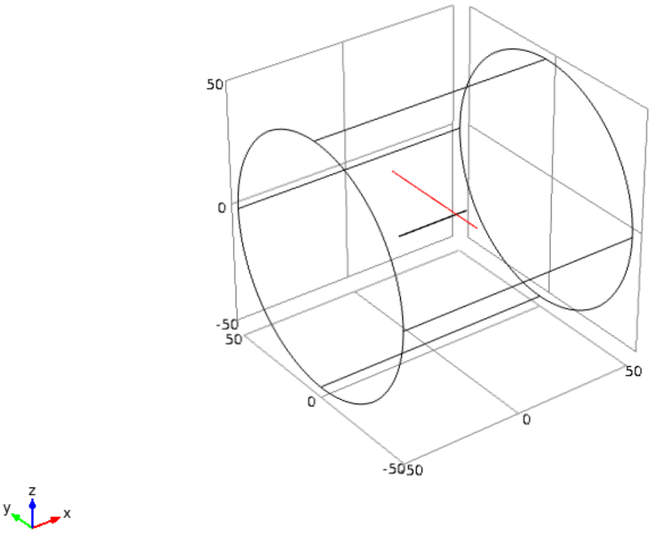

Figure 4.70: Observation line (x=0, y=-25 to y=25, z=10).

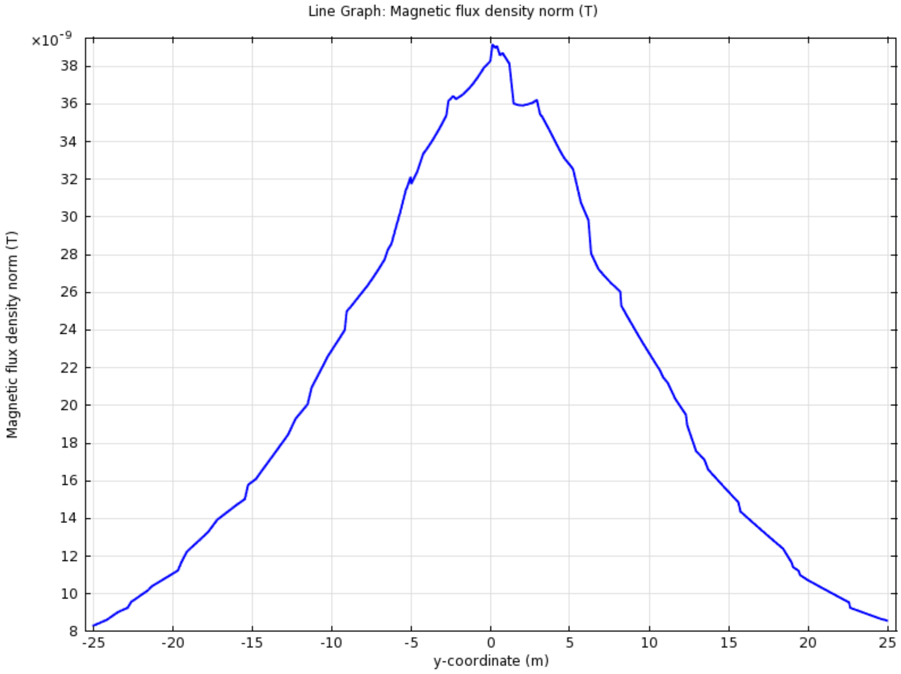

Figure 4.71: Magnetic Flux Density norm on the line of (x=0, y=-25 to y=25, z=10).

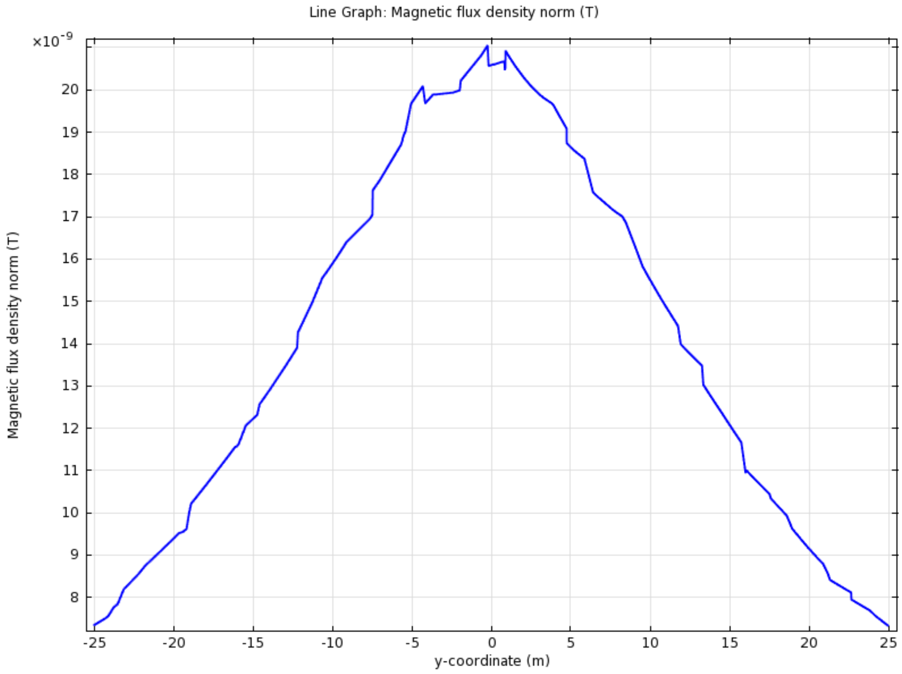

Figure 4.72: Magnetic Flux Density norm on the line of (x=0, y=-25 to y=25, z=15).

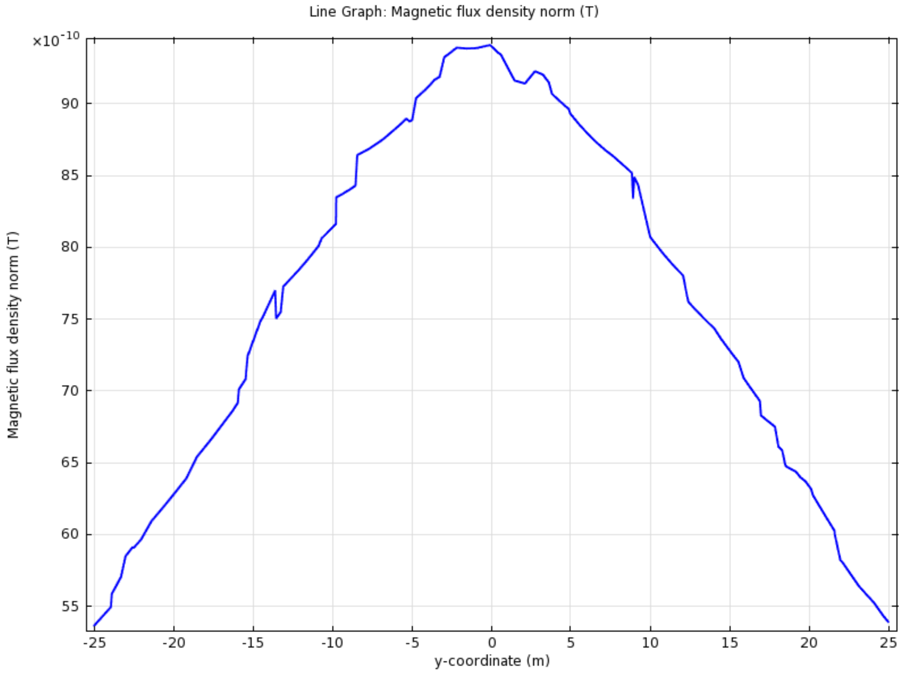

Figure 4.73: Magnetic Flux Density norm on the line of (x=0, y=-25 to y=25, z=25).

Observation line	**(x=0, y=0, z=-40m to 40m)**	**(x=0, y=-25m to 25m, z=10)**	**(x=0, y=-25m to 25m, z=15)**	**(x=0, y=-25m to 25m, z=25)**
Maximum magnetic field (nT)	650000	38	21	10

Table 4.11: Magnetic field of current carrying wire.

When we compare the perturbation of ambient Earth magnetic field due to the submarine as well as magnetic field of the current carrying wire, we see that the wire cannot create as much magnetic field values as on the equal distances away from them. For instance, submarine perturbs 420nT on the observation point (x=0, y=0, z=28m) which is 25m away from on the z-direction, but the current of the wire creates 10nT field on the observaion point (x=0, y=0, z=25m). After this observation, we can say that for this geometry of the wire (30m) and the current value (8.25A), this wire cannot create as much field as the submarine perturbs on the ambient Earth magnetic field on the same observation points. One possible solution to this problem is that the wire can be driven by higher current values and the observation lines of it can be closer compared to the observation lines of the submarine. As an example, if the current on the wire is 82.5A which is ten times designated and the observation point is (x=0, y=0, z=10m), magnetic flux density on this point is 380nT. This much perturbation values for the submarine (420nT) can be observed when the observation point of the submarine is (x=0, y=0, z=25) which is 25m away from it. This means that detection performance of the magnetic anomaly detector equipped aircrafts can be evaluated via current carrying wire systems.

Chapter 5

DISCUSSION & CONCLUSION

In this thesis, we focused on low frequency magnetic field in seawater. We stated the governing equations of electromagnetic waves. We compared electrical properties (electrical conductivity, relative permeability and relative permittivity) of air (vacuum) and seawater. Then we compared the speed and wavelength of electromagnetic wave in air and seawater. In order to solve magnetic field of a coil in seawater with the help of COMSOL Multiphysics packet software, we designed an air-cored multilayer coil which can be realized and driven by plausible power values. After the design of the coil, we studied low frequency magnetic field of this coil in seawater in different cases. In each simulation, geometry of the model is taken, appropriate physics for the analysis is chosen, boundary conditions for the geometry and enclosing solution domain are assigned and mesh of the geometries and the medium are generated. In the first study we solved magnetic field of the coil for three frequencies in air and in seawater on different observation arcs, lines and points. We observed the attenuation of magnetic field due to the electrical conductivity (4 S/m) of seawater and due to the increase of the frequency. In the second study, we observed the shielding effect of the electrical conductivity of the material and thickness of the case which holds the coil. We observed that as the electrical conductivity of the material and the thickness of the case increases, shielding of the case on the magnetic field of the coil increases, magnetic field of the coil attenuates more. We suggested GRP or CRP whose electrical conductivities are under 10^6(S/m) for the material of the case. However, if the case has to be metal, we suggested stainless steel whose electrical conductivity is $1.45\text{x}10^6$ (S/m). The case has to be as thin as possible to avoid the attenuation of the field. In the third study, we solved the magnetic flux density of the coil on observation points when there is a metal plate in the medium. We designated a detection region for the metal plate. We moved the coil and the observation point according to this region to observe the fields on the observation point. We took the material of the plate as iron and copper. Both of these materials have high electrical conductivity but copper has higher electrical conductivity (5.998 x 10^7 (S/m)) than iron (1.12 x 10^7 (S/m)). Iron has 4000 relative permeability and copper has unit relative permeability. Skin depth on the iron plate is 0.1mm so it was not necessary to solve inside of it. On the other hand, skin depth on the copper plate is 2.665mm, so it was necessary to solve inside of it. However, thickness of the plate is so small (0.04m) compared to other edges of it (6m x 12m) and this makes harder to generate mesh inside of the copper plate. When we wanted to have finer meshes inside of the copper plate, we get the warning of "out of memory". Real and imaginary parts of x and z components of the field change due to eddy currents on the metal plate. Norm of x and z components of the fields increases more when the plate is copper than the plate is iron. As the electrical conductivity of the material of the plate increases, more eddy currents are created on the metal plate, perturbation of the magnetic field on the observation point increases as well. Change in the real part of x component of the field occurs on 67nT, so the sensing circuit can be saturated. Change in the imaginary part of x component of the field occurs on 1nT, so this value must be subtracted from the measured field on the observation point to find the change in the field. Change in the real and imaginary part of z component of the field occurs on zero nT, so the sensing circuit cannot be saturated easily. Levels of the perturbation of the magnetic field on the observation point due to metal plate are between 0.3 to 10nT. Fluxgate magnetometers can measure fields of approximately 0.1nT. This means that we can place a fluxgate magnetometer onto the observation point to measure perturbation of the field and detect the metal plate in the defined detection region in 7m. Difference of the phase angle of z component of field due to iron and copper plate is around 15^0. This angle can be valuable to discriminate the sort of the metal to be detected. Therefore, quadrature sensing can still be useful. In the forth study, we solved the perturbation of ambient Earth magnetic field due to a submarine as well as solved the magnetic field of a DC current carrying wire. We investigated how the perturbation on ambient Earth magnetic field due to the submarine can be imitated by an underwater system which tows a DC current carrying wire. We concluded that by applying higher DC current than 8.25A to the straight wire and flying the magnetic anomaly detector (MAD) equipped aircraft closer to the wire system, same levels of perturbation can be measured as levels of perturbation due to the submerged submarine.

As a future work, a theoretical way to solve fields and currents inside of the copper plate without meshing and solving inside of it can be studied. This can be a boundary condition like impedance boundary condition. By just assigning this boundary condition onto the surfaces of the copper plate and setting the thickness of it, fields and currents can be solved inside of it with less generation of mesh; which means that less computation power and physical memory of the computer are required.

Bibliography

[1] A. Palmeiro, M. Martin, I. Crowther, and M. Rhodes, "Underwater radio frequency communications," in *OCEANS, 2011 IEEE-Spain*, pp. 1-8, IEEE, 2011.

[2] M. Stojanovic, "Recent advances in high-speed underwater acoustic communications," *IEEE Journal of Oceanic Engineering*, vol. 21, no. 2, pp. 125-136, 1996.

[3] R. Coates and P. Willison, "Underwater Acoustic Communications: A Review and Bibliography," *The Institute of Acoustics*, 1987.

[4] R. Coates, R. Owen, and M. Zheng, "Underwater Acoustic Communica-tions: A Review and Bibliography (ii)," *PROCEEDINGS-INSTITUTE OF ACOUSTICS*, vol. 15, pp. 1-1, 1993.

[5] J. A. Catipovic, "Performance limitations in underwater acoustic telemetry," *IEEE Journal of Oceanic Engineering*, vol. 15, no. 3, pp. 205-216, 1990.

[6] J. Smart, "Underwater optical communications systems Part 1: variability of water optical parameters," in *Military Communications Conference, 2005. MILCOM 2005. IEEE*, pp. 1140-1146, 2005.

[7] J. W. Giles and I. N. Bankman, "Underwater optical communications systems. Part 2: basic design considerations," in *Military Communications Conference, 2005. MILCOM 2005. IEEE*, pp. 1700-1705, 2005.

[8] F. Hanson and S. Radic, "High bandwidth underwater optical communication," *Applied optics*, vol. 47, no. 2, pp. 277-283, 2008.

[9] N.Farr, A. Bowen, J. Ware, C. Pontbriand, and M. Tivey, "An integrated, underwater optical/acoustic communications system," in *OCEANS 2010 IEEE-Sydney*, pp. 1-6, 2010.

[10] M. R. Frater, M. J. Ryan, and R. M. Dunbar, "Electromagnetic communications within swarms of autonomous underwater vehicles," in *Proceedings of the 1st ACM international workshop on Underwater networks*, pp. 64-70, ACM, 2006.

[11] X.Che, I. Wells, G. Dickers, P. Kear, and X. Gong, "Re-evaluation of RF electromagnetic communication in underwater sensor networks," *Communications Magazine, IEEE*, vol. 48, no. 12, pp. 143-151, 2010.

[12] X.Che, I. Wells, P. Kear, G. Dickers, X. Gong, and M. Rhodes, "A static multi-hop underwater wireless sensor network using RF electromagnetic communications," in *29th IEEE International Conference on Distributed Computing Systems Workshops, 2009. ICDCS Workshops' 09.*, pp. 460-463, 2009.

[13] M. Rhodes, "Underwater electromagnetic propagation: re-evaluating wireless capabilities," Hydro International, vol. 10, no. 10, pp. 28-31, 2006

[14] E. Foster, "A Diver-Operated Underwater Metal Detector," *Archaeometry*, vol. 12, no. 2, pp. 161-166, 1970.

[15] J. N. Green, E. Hall, and M. Katzev, "Survey of a Greek shipwreck o Kyrenia, Cyprus," *Archaeometry*, vol. 10, no. 1, pp. 47-56, 1967.

[16] P. Czipott and W. Podney, "Use of a superconductive gradiometer in an ultrasensitive electromagnetic metal detector," *IEEE Transactions on Magnetics*, vol. 25, no. 2, pp. 1204-1207, 1989.

[17] C. J. Clausen and J. B. Arnold, "The magnetometer and underwater archaeology," *International Journal of Nautical Archaeology*, vol. 5, no. 2, pp. 159- 169, 1976.

[18] J. N. Heine, "Scientific diving techniques," *Marine Technology Society Journal*, vol. 34, no. 4, pp. 23-37, 2001.

[19] K. Asakawa, Y. Shirasaki, and Y. Iwamoto, "Metal detector for tracing submarine telecommunication cables," *IEEE Transactions on Instrumentation and Measurement*, vol. 32, no. 4, pp. 477-483, 1983.

[20] J.-G. Webster, *The Measurement, Instrumentation, and Sensors: Handbook*. Springer, 1999.

[21] D. Guelle, *Metal Detector Handbook for Humanitarian Demining: A Book about Metal Detectors, Covering Detection Procedures in the Field, and the Testing and Evaluation of Metal Detectors for Humanitarian Demining*. Office for Offcial Publications of the European Communities, 2003.

[22] J. Tyson, "How metal detectors work," *How Stuff Works*, 2003.

[23] M. Rowan and W. Lahr, "How Metal Detectors Work," 2002.

[24] V. Aravinthan and T. Nanyakkara, "Intellligent signal classification in VLF metal detectors to distinguish landmines from harmless metal debris," *proceedings of the annual sessions of the IEE Sri Lunka section*, 2004.

[25] M. S. Sharawi and M. Sharawi, "Design and implementation of a low cost VLF metal detector with metal-type discrimination capabilities," in *IEEE International Conference on Signal Processing and Communications*, 2007. ICSPC 2007., pp. 480-483, 2007.

[26] J. Corbyn, "Pulse induction metal detector," *Wireless World*, vol. 86, no. 1531, pp. 40-44, 1980.

[27] W. E. Lahr, "Pulse induction metal detector," May 9 1995. US Patent 5,414,411.

[28] W.-S. Hua, J. R. Hooks, W.-J. Wu, and W.-C. Wang, "Development of a novel polymeric fiber-optic magnetostrictive metal detector," in *SPIE Smart Structures and Materials+ Nondestructive Evaluation and Health Monitoring,* pp. 76501P-76501P, International Society for Optics and Photonics, 2010.

[29] H. Huang and I. Won, "Characterization of UXO-like targets using broadband electromagnetic induction sensors," *IEEE Transactions on Geoscience and Remote Sensing*, vol. 41, no. 3, pp. 652-663, 2003.

[30] I. Won, S. Norton, B. SanFilipo, and F. Kunak, "Active broadband electromagnetic detection and classification of buried naval mines," in *OCEANS'02 MTS/IEEE*, vol. 2, pp. 966-973, 2002.

[31] Y. Iwamoto, Y. Shirasaki, and K. Asakawa, "Fiber-optic-tethered unmanned submersible for searching submarine cables," in *OCEANS 82*, pp. 65-72, 1982.

[32] F. Primdahl, "The fluxgate magnetometer," *Journal of Physics E: Scientific Instruments*, vol. 12, no. 4, p. 241, 1979.

[33] H. C. Hayes, "Detection of submarines," *Proceedings of the American Philosophical Society*, vol. 59, no. 1, pp. 1-47, 1920.

[34] A. Sheinker, B. Ginzburg, N. Salomonski, P. A. Dickstein, L. Frumkis, and B. Kaplan, "Magnetic Anomaly Detection Using High-Order Crossing Method," *IEEE Transactions on Geoscience and Remote Sensing*, vol. 50, no. 4, pp. 1095-1103, 2012.

[35] T. A. Gardner, "Magnetic Anomaly Detection." http://www.uboat.net., Accessed: 2013-09-02.

[36] C. Multiphysics, "4.2 User’s Guide," 2011.

[37] A. I. Al-Shamma'a, A. Shaw, and S. Saman, "Propagation of electromagnetic waves at MHZ frequencies through seawater," IEEE Transactions on Antennas and Propagation, vol. 52, no. 11, pp. 2843-2849, 2004.

[38] H. A. Wheeler, "Simple inductance formulas for radio coils," *Proceedings of the Institute of Radio Engineers*, vol. 16, no. 10, pp. 1398-1400, 1928.

[39] C. Multiphysics, "Rf module user's guide," 2008.

[40] R. L. Stoll, *The analysis of eddy currents*. Clarendon Press Oxford, 1974.

[41] D. C. Giancoli and J. J. Boyle, *Physics: principles with applications*. Pearson Education, 2005.

Appendix A

Detailed Description of Simulation: Iron Plate

We presented solutions of perturbation of magnetic flux density of the coil due to iron plate in the section 4.3.1. Now we present how we setup models, boundary conditions and meshes in Comsol Multiphysics. We used Comsol 4.3a for the simulations. We solve the problem when the coil is at the origin (0, 0, 0) and the observation point is at the point (5, 0, 0). We present this solution as an .mph file. The name of the file is *iron_35m.mph*.

Firstly we selected *3D* space dimension. We added physics, interface of *Magnetic Fields (mf)* under *AC/DC* branch. We selected *Frequency Domain* as the study type and started creating the models.

Under the *Global Definitions* branch we defined four parameters: *shift_x*, *shift_y*, *shift_z* and *ang* to be able to parametrize the solutions. First three parameters let us change the position of the coil and *ang* lets us change the phase angle of the solution.

Under the *Geometry1* branch we created solution domain which is Cylinder1 *(cyl1)*, coil which is under the branch of *Work Plane1 (wp1)*, plate which is *Block1 (blk1)*. In order to be able to solve the field more accurately on the observation point which is 5m away from the center of the coil we created a cylinder which *Cylinder2 (cyl2)* and a point which is *Point1 (pt1)*. This cylinder lets finer meshes be generated around the observation point. The point lets a node of the mesh be on the observation point. Domain 1 refers to solution domain, Domain 2 refers to plate domain, Domain 3 refers to coil domain and Domain 4 refers to the cylinder which includes the observation point.

Under the *Magnetic Fields (mf)* branch we assigned Ampere's Law and boundary conditions to the model. We excluded Domain 2 from *Magnetic Fields (mf)*, thus we do not solve inside of it. We assigned *Ampere's Law 1* to Domain 1 and Domain 4. Domain 2 is not applicable to this solution. We set electrical conductivity (σ) to 4, relative permittivity (ε_r) to 80 and relative permeability (μ_r) to 1. We created *Ampere's Law 2* and assigned Domain 3 in it. We set electrical conductivity (σ) to 0.001 (Comsol does not let it be zero), relative permittivity (ε_r) to 1 and relative permeability (μ_r) to 1. Finally we assigned *Impedance Boundary Condition 1* to six surfaces of the plate. We set electrical conductivity (σ) to 1.12e7, relative permittivity (ε_r) to 1 and relative permeability (μ_r) to 4000. These electrical properties belong to iron (Fe). We assigned *External Current Density 1* to Domain 3.

Under the *Mesh1* branch we set mesh parameters of the domains. We created four Free Tetrahedral. *Free Tetrahedral 2* is assigned to Domain 3 and maximum element size is set to 4cm. *Free Tetrahedral 3* is assigned to Domain 4 and maximum element size is set to 1cm. *Free Tetrahedral 4* is assigned to Domain 2 and maximum element size is set to 16cm. *Free Tetrahedral 4* is assigned to entire geometry and predefined configuration of *Extra Fine* is set.

Finally, under the *Study1* branch we set the frequency and solvers. We set 600 Hz in *Step1: Frequency Domain* and compute.

We solved magnetic flux density on the observation point for 46 different positions of the coil. We sweep the coil from x=-15m to x=7m on two planes; z=0 and z=-3.5m. We added *Parametric Sweep* under *Study 1* and made *shift_x* increase from -15 to 7 when *shift_z* is 0 to have 23 solutions. We repeat this process when shift_z is -3.5m and thus we have 46 solutions for different positions of the coil under the iron plate.

Appendix B

Detailed Description of Simulation: Copper Plate

We presented solutions of perturbation of magnetic flux density of the coil due to copper plate in the section 4.3.2. Now we present how we setup models, boundary conditions and meshes in Comsol Multiphysics. We used Comsol 4.3a for the simulations. We solve the problem when the coil is at the origin (0, 0, 0) and the observation point is at the point (5, 0, 0). We present this solution as an .mph file. The name of the file is copper*_35m.mph*.

Firstly we selected *3D* space dimension. We added physics, interface of *Magnetic Fields (mf)* under *AC/DC* branch. We selected *Frequency Domain* as the study type and started creating the models.

Under the *Global Definitions* branch we defined four parameters: *shift_x*, *shift_y*, *shift_z* and *ang* to be able to parametrize the solutions. First three parameters let us change the position of the coil and *ang* lets us change the phase angle of the solution.

Under the *Geometry1* branch we created solution domain which is Cylinder1 *(cyl1)*, coil which is under the branch of *Work Plane1 (wp1)*, plate which is *Block1 (blk1)*. In order to be able to solve the field more accurately on the observation point which is 5m away from the center of the coil we created a cylinder which *Cylinder2 (cyl2)* and a point which is *Point1 (pt1)*. This cylinder lets finer meshes be generated around the observation point. The point lets a node of the mesh be on the observation point. Domain 1 refers to solution domain, Domain 2 refers to plate domain, Domain 3 refers to coil domain and Domain 4 refers to the cylinder which includes the observation point.

Under the *Materials* branch, we added *Copper (mat1)* and assigned Domain 2 in it. Thus we set the properties of the plate as Copper (Cu).

Under the *Magnetic Fields (mf)* branch we assigned Ampere's Law and boundary conditions to the model. We assigned *Ampere's Law 1* to Domain 1 and Domain 4. We set electrical conductivity (σ) to 4, relative permittivity (ε_r) to 80 and relative permeability (μ_r) to 1. We created *Ampere's Law 2* and assigned Domain 3 in it. We set electrical conductivity (σ) to 0.001 (Comsol does not let it be zero), relative permittivity (ε_r) to 1 and relative permeability (μ_r) to 1. We created *Ampere's Law3* and assigned Domain 2 in it. This plate domain gets electrical properties *From material*. We assigned *External Current Density 1* to Domain 3.

Under the *Mesh1* branch we set mesh parameters of the domains. We created four Free Tetrahedral. *Free Tetrahedral 2* is assigned to Domain 3 and maximum element size is set to 4cm. *Free Tetrahedral 3* is assigned to Domain 4 and maximum element size is set to 1cm. *Free Tetrahedral 4* is assigned to Domain 2 and maximum element size is set to 10cm. *Free Tetrahedral 4* is assigned to entire geometry and predefined configuration of *Extra Fine* is set.

Finally, under the *Study1* branch we set the frequency and solvers. We set 600 Hz in *Step1: Frequency Domain* and compute.

We solved magnetic flux density on the observation point for 46 different positions of the coil. We sweep the coil from x=-15m to x=7m on two planes; z=0 and z=-3.5m. We added *Parametric Sweep* under *Study 1* and made *shift_x* increase from -15 to 7 when *shift_z* is 0 to have 23 solutions. We repeat this process when shift_z is -3.5m and thus we have 46 solutions for different positions of the coil under the copper plate.